

Masterarbeit

# Wire Bonding on 2S Modules of the Phase-2 CMS Detector

von

Tim Ziemons

vorgelegt der

**Fakultät für Mathematik, Informatik und  
Naturwissenschaften der RWTH-Aachen**

im September 2017

angefertigt im

**I. und III. Physikalischen Institut B**

bei

**Erstgutachter: PD Dr. Oliver Pooth**

**Zweitgutachter: Prof. Dr. Lutz Feld**





# List of abbreviations

**LHC** Large Hadron Collider

**CMS** Compact Muon Solenoid

**HEP** high energy physics

**CERN** European Council for Nuclear Research

**LS** Long Shutdown

**LEP** Large Electron-Positron Collider

**ATLAS** A Toroidal LHC Apparatus

**HL** High Luminosity

**ECAL** electromagnetic calorimeter

**HCAL** hadron calorimeter

**MET** missing transverse energy

**HO** outer calorimeter

**L1** Level-1

**HLT** High-Level-Trigger

**IT** Inner Tracker

**OT** Outer Tracker

**CBC** CMS Binary Chip

**CIC** Concentrator Integrated Circuit

**CFRP** carbon fibre reinforced polymer

**FE** front-end

**LpGBT** Low-power Gigabit Transceiver

**VTRx+** Versatile TRansceiver plus

**ESD** electrostatic discharge

**TDF** touchdown force

**BPC** Bond Process Control

**US** ultra-sonic

**BF** bond force

**BT** bond time

**WTS** wire tensile strength

**WD** wire diameter

**ENIG** electroless nickel immersion-gold

**RT** room temperature

**2K** two-component

**TOB** tracker outer barrel

**ARC** APV read-out controller

**ADC** Analog-to-Digital-Converter

# Contents

<b>1</b>	<b>Introduction</b>	<b>1</b>
<b>2</b>	<b>The CMS Experiment at the Large Hadron Collider</b>	<b>3</b>
2.1	The Large Hadron Collider . . . . .	3
2.2	Overview of the CMS Detector . . . . .	4
2.3	The Phase-2 Upgrade . . . . .	6
2.3.1	Overview . . . . .	6
2.3.2	Tracker upgrade . . . . .	7
<b>3</b>	<b>Wire Bonding</b>	<b>11</b>
3.1	Overview . . . . .	11
3.2	Quality Test Procedure . . . . .	15
3.2.1	Wire Pull Test . . . . .	15
3.2.2	Visual Inspection . . . . .	19
3.3	Setup . . . . .	20
3.3.1	Bonding machine and bonding equipment . . . . .	20
3.3.2	Quality Checks . . . . .	24
3.4	Optimization of bond parameters . . . . .	25
3.4.1	Boundary conditions . . . . .	25
3.4.2	Studies of the bond parameters with deactivated Bond Process Control	31
3.4.3	Studies of BPC related features . . . . .	43
3.5	Bond procedure in module series production . . . . .	51
3.5.1	Description of the dummy module and its preparation . . . . .	51
3.5.2	Determination of the correction factors and systematic uncertainties for parameter optimization . . . . .	53
3.5.3	Optimization of the bond parameters . . . . .	56
3.5.4	The bonding program . . . . .	60
3.5.5	Determination of the correction factor for the test wires . . . . .	64
3.5.6	Analysis of quality tests and issues . . . . .	65
<b>4</b>	<b>Encapsulation</b>	<b>69</b>
4.1	Overview . . . . .	69

4.2	Encapsulation setup . . . . .	71
4.3	Encapsulation tests . . . . .	72
4.3.1	The different degrees of freedom . . . . .	72
4.3.2	Viscosity of the different glues . . . . .	73
4.3.3	Tests on wire bonds . . . . .	75
<b>5</b>	<b>Summary and Outlook</b>	<b>79</b>
	<b>List of Figures</b>	<b>I</b>
	<b>List of Tables</b>	<b>VII</b>
	<b>Bibliography</b>	<b>IX</b>

# 1 Introduction

Particle physics has experienced an extremely high public interest in the last thirty years as incredible human effort has been spent to reveal the mysteries of the universe. Questions like “How has the universe been evolved?”, “How can electroweak symmetry breaking be explained?” or “What is dark matter?” are only a few of the questions which motivated the construction of the *Large Hadron Collider (LHC)* at CERN (European Council for Nuclear Research) which is the most powerful particle accelerator built by human beings. On 4th July 2012, the ATLAS and the CMS experiment both presented the observation of a new particle with a mass of about 125 GeV, the long-sought Higgs particle [1]. Only one year later Peter Higgs and François Englert have been awarded the Nobel Prize in Physics for a mechanism that theoretically predicts this recently discovered particle [2]. But there are still many unanswered questions.

The LHC is going to be upgraded to achieve much higher collision rates to collect more data than ever before. Radiation damage and new technological challenges corresponding to the LHC upgrade require the exchange of detector elements of the CMS detector, the so-called Phase-2 Upgrade [3]. Among other sub-detectors, the entire tracker has to be replaced. Therefore new tracker modules have to be designed, built and tested until they are finally installed during the Long Shutdown (LS) 3 from 2024 to 2026.

RWTH Aachen University is involved in the design, test and production of 2S tracker modules of the Phase-2 upgrade. One aspect of this is the electrical connection of the particle detecting sensors and the electronic hybrids which process the sensor signal. The electrical connection is achieved via thin aluminum wires that are welded onto the two components. The method used is called wire bonding. As thousand modules at least will be produced in Aachen, the series production has to be prepared and the quality of the bond connections has to be optimized. These goals form one part of the work of this master thesis. Because the wires are very fragile, the CMS collaboration plans to encapsulate them with a soft glue. Therefore appropriate glues have to be tested and a precise and repeatable dispensing system has to be prepared for the series production. First studies of three different glue candidates and the challenges in the dispensing process of a series production are also discussed in this theses.



# 2 The CMS Experiment at the Large Hadron Collider

This chapter introduces the CMS detector. The LHC and the LHC upgrade plans are shortly discussed in Chapter 2.1. A general overview of the Compact Muon Solenoid (CMS) detector and the detecting principle is presented in Chapter 2.2. As a last step the Phase-2 upgrade is discussed in Chapter 2.3.

## 2.1 The Large Hadron Collider

The LHC is nowadays the largest man-made particle collider and therefore one of the most important accelerator experiments in the field of high energy physics (HEP). It is located at CERN (European Council for Nuclear Research) at the border between Switzerland and France near Geneva [4]. It is operated in the approximately 27 km long ring shaped tunnel of the precursor synchrotron experiment LEP (Large Electron-Positron Collider) 50 to 175 m underground [5, 6].

The LHC is mainly a proton-proton collider designed to reach center-of-mass energies up to  $\sqrt{s} = 14 \text{ TeV}$  with an instantaneous luminosity<sup>1</sup> of about  $\mathcal{L} \approx 1.0 \times 10^{34} \text{ cm}^{-2}\text{s}^{-1}$  [8]. Additionally, heavy ions are accelerated and collide to investigate the so called “quark-gluon plasma”, a state of matter present in the early universe which can be artificially produced by the LHC. The particle collisions are observed at four different points of the circular collider with the experiments ATLAS, CMS, LHCb and ALICE.

The start of the project Large Hadron Collider may be dated to be a workshop in Lausanne, Switzerland, in March 1984 when the concept of the LHC has been discussed for the first time [1]. It took more than 24 years of developing the technology and actually building magnets and the detectors from that date to the first successfully steered proton beam on 10 September 2008. Nine days later there was an incident during power tests of the main dipole circuit which caused mechanical damage and release of helium into the tunnel. One

---

<sup>1</sup>The instantaneous luminosity is a measure for the rate of particle collisions in a collider experiment. It is proportional to the frequency of particles traversing in the collider, the number of particles in the particle bunches and the inverse of the bunch size. The so called “integrated luminosity” is the luminosity integrated over time. By multiplying this value with the cross section of a certain process the expected number of events can be calculated [7].

year later the repairs have been finished and on 20 November 2009 the first beams started to circulate in the LHC for the first time after the incident. Until the end of the year collisions with energies up to 2.36 TeV have been detected. First collisions with center of mass energies of 7 TeV have been detected at end of March 2010. In 2012 the energy was further increased to 8 TeV with a maximum instantaneous luminosity of  $0.76 \times 10^{34} \text{ cm}^{-2}\text{s}^{-1}$  at the CMS detector [9]. The LHC Run 2 started with a higher energy of 13 TeV in 2015 and until the end of 2016 peak luminosities up to  $1.53 \times 10^{34} \text{ cm}^{-2}\text{s}^{-1}$  have been measured at CMS. At the end of 2018 the LS2 will start, followed by Run 3 in 2021 [10]. Until the end of Run 3 the instantaneous luminosity is planned to be increased up to twice the nominal design luminosity [11]. The LS3 (starting at the end of 2024) will then be used to install the so-called High Luminosity LHC (HL-LHC) which will provide instantaneous peak luminosities of 5 or even  $7.5 \times 10^{34} \text{ cm}^{-2}\text{s}^{-1}$ .

## 2.2 Overview of the CMS Detector

The CMS detector is a general purpose detector which means that it is designed to measure all physical processes that might occur in the collisions of the LHC [12]. The name CMS is an acronym for Compact Muon Solenoid. With its mass of about 14,000 tons and the dimensions of 15 m in height and 21 m in length the CMS detector is compact compared to other experiments like ATLAS. The special mentioning of “Muons” in the name of the detector is because it is designed to measure especially the muons with very high accuracy. The last word “Solenoid” refers to the strong solenoidal magnet. The magnetic field bends the charged particle’s trajectories. Those are reconstructed to measure the electrical charge and the momentum of the particle.

The CMS detector is constructed of 15 separate slices which have been built on the surface and then lowered to the cavern [12]. This made the construction much more comfortable and allows to easily access the different parts of the detector for maintenance and upgrades. The detector is composed of multiple layers of different sub-detectors. Figure 2.1 shows a sketch of the detector structure.

The innermost part is the silicon tracker which consists of the pixel detector and the silicon strip tracker [14]. The pixel detector delivers high precision space points close to the interaction point. This is important to achieve secondary vertex reconstruction with high resolution. The pixel modules are arranged in so-called barrel layers and endcap disks. The barrel layer modules are installed around the beam axis. The endcap disk modules are arranged perpendicular to the beam axis at each side of the detector. In this way the CMS

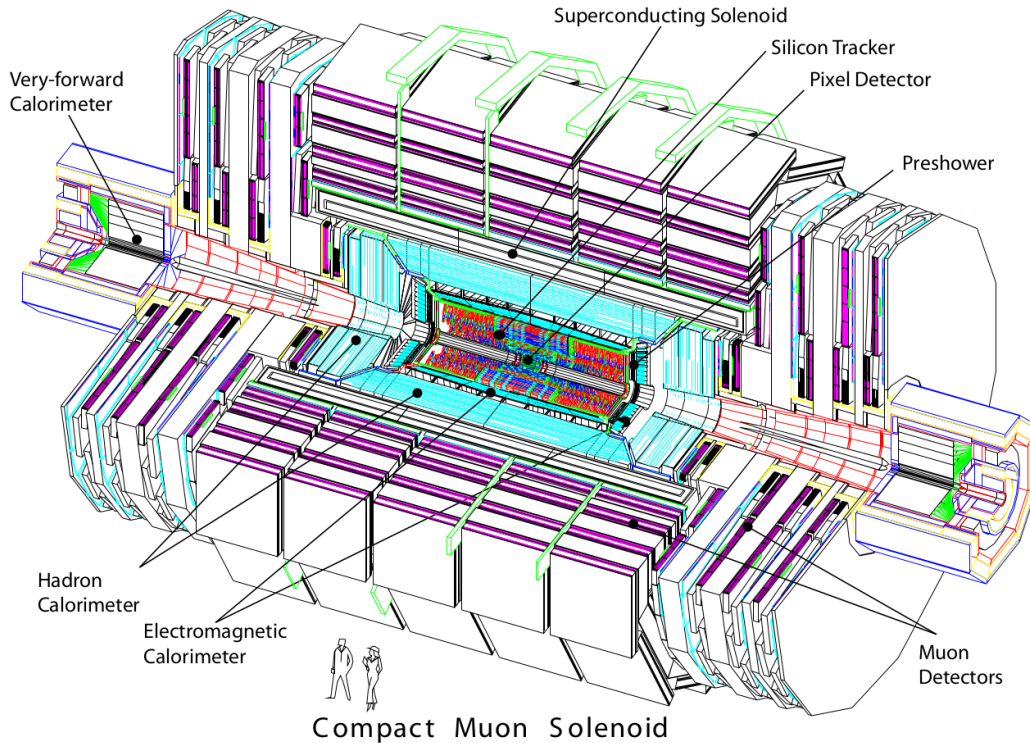


Figure 2.1: Sketch of the CMS detector layout [13].

pixel detector realized for the start of the LHC (Phase-0) covers a pseudorapidity<sup>2</sup> range of  $-2.5 < \eta < 2.5$  with 48 million pixels in the barrel and 18 million in the endcap region [14]. The silicon strip tracker is installed at larger distances to the interaction point to increase the range of precisely measured trajectories. The Phase-0 tracker has more than 24 thousand strip sensors with 15 different geometries. In total this sums up to 9.3 million strips forming a sensitive area of  $198 \text{ m}^2$ .

The next sub-detector going from the inside to the outside is the electromagnetic calorimeter (ECAL). It consists of lead-tungstate ( $\text{PbWO}_4$ ) scintillator crystals which have a high density of  $8.28 \text{ g cm}^{-3}$ , a short radiation length of  $0.89 \text{ cm}$  and a small Molière radius ( $2.2 \text{ cm}$ ) [14]. In total there are 61,200 crystals in the barrel region which are connected to avalanche photodiodes to detect the created photons. The endcap region is instrumented by 7,324 crystals of which the photons are measured using vacuum phototriodes. The ECAL measures the energy of photons and electrons [12]. Both are completely stopped inside the calorimeter. The CMS Preshower is used for the identification of neutral pions in the pseudorapidity region of  $1.653 < |\eta| < 2.6$  [14].

The hadron calorimeter (HCAL) is used to measure the energy of hadrons and thus it is also important for the determination of the missing transverse energy (MET) which for example

<sup>2</sup>The pseudorapidity is a parameter used to describe the flight direction of a particle in a detector. It is defined by  $\eta = -\ln \tan(\theta/2)$  with  $\theta$  being the angle between the particle's flight direction and the beam axis.

emanates from neutrinos in the final state. It is a sampling calorimeter alternately consisting of C26000/cartridge brass absorber material and plastic scintillators in the barrel and the endcaps.

All sub-detectors described above are installed within the superconducting solenoidal magnet made of NbTi. They experience a magnetic field of up to 3.8 T in the free bore of 12.5 m length and a radius of about 3 m [14]. An iron yoke with a mass of about 10,000 t returns the flux in the outer region of the detector up to an extent of 14 m diameter. It consists of five rings in the barrel region and six endcap disks structured as layers.

The outer calorimeter (HO) is positioned in the first layers of the iron return yoke in the barrel. The solenoid material is used as additional absorber material to measure the energy of late starting hadronic showers with the HO as a tail catcher.

The muons are measured using the muon system which is installed at the largest radial distance to the interaction point. Up to  $|\eta| < 1.2$  muons are detected by drift tube chambers [14]. They are arranged in four stations between the layers of the iron return yoke. The endcaps house cathode strip chambers used to detect muons for  $0.9 < |\eta| < 2.4$ . Resistive plate chambers are used as a complementary fast trigger system in both regions.

The CMS detector observes particle collisions up to 40 million times per second [12]. The amount of data cannot be handled if the data of all events would be stored. So a trigger system has been developed to separate interesting events, which have to be stored from the others. The so-called Level-1 (L1) trigger is the first instance. It uses information of the muon system and the calorimetry [15]. The combination of the information determines whether the event is accepted or rejected. Thus the rate is reduced to about 100 kHz. The next instance of event filtering is called High-Level-Trigger (HLT). As more time is available more information (for example tracker data) are used to further reduce the rate to about 300 Hz.

## 2.3 The Phase-2 Upgrade

### 2.3.1 Overview

The CMS detector as described above proved to provide excellent performance. However, the increase of the luminosity delivered by the LHC in the course of the HL-LHC upgrade confronts the CMS detector with challenges. The high integrated luminosity of the LHC causes radiation damage to the CMS detector. Additionally the high collision rate could result in efficiency losses degrading the performance of the detector [3]. The radiation dose delivered to CMS until the start of LS3 is similar to the dose which the HL-LHC will generate each year. So new hardware has to be installed which is able to resist the harsh radiation environment. The second major challenge is the so-called “pile-up” which will be increased

due to the higher instantaneous luminosity: As the LHC beams consist of proton “bunches” with a number of protons in the order of  $10^{11}$ , many protons interact every time when two bunches cross (40 MHz) [3]. In the HL-LHC the average number of interacting protons in a single crossing is expected to be approximately 140. The major part of these are “soft” interactions which do not contain new physics. However, those additional collisions may degrade the measurements and analysis of “hard” interactions.

The muon chambers are expected to be qualified for HL-LHC conditions but the front-end electronics have to be replaced. The new versions will have improved performance and radiation tolerance [10]. Additionally they will have a faster readout. Improved resistive plate chambers and gas electron multiplier detectors will be added in order to enhance triggering, reconstruction performance and the acceptance in this region.

The lead-tungstate crystals of the ECAL will be kept but operated at a lower temperature. Furthermore, the front-end boards will be improved so that single crystals can contribute information for the L1 trigger instead of groups of  $5 \times 5$  crystals [10]. Already before LS3 the hybrid photodiodes, which are used to read out the scintillator tiles of the HCAL, will be replaced by silicon photomultipliers. During LS3 new scintillator tiles will replace the ones close to the beam line. The ECAL and HCAL endcaps will be removed and a new combined electromagnetic and hadronic sampling calorimeter will be installed [10]. It will be based on silicon pad sensors with pad cell sizes of 0.5- 1 cm<sup>2</sup>. The hadronic section will still be instrumented with plastic scintillator tiles with silicon photomultiplier readout at large distances from the beam line. The pileup rejection and thus also the particle identification profit from the high granularity of the new sub-detector.

In Run 4 (after LS3) the L1 trigger rate limitation will be increased to 750 kHz. The rate at the HLT will be limited to 7.5 kHz. Furthermore, tracking information will already be used in the L1 trigger. The track trigger concept and the upgrade of the tracker are described in the following.

### 2.3.2 Tracker upgrade

The entire tracking detector has to be replaced. The new Inner Tracker (IT) and Outer Tracker (OT) modules require a high radiation tolerance because the particle fluence depends primarily on the radial distance to the beam. The radiation exposure of the innermost region of the tracker is expected to be 1 MeV neutron equivalent fluence of  $2.3 \times 10^{16} n_{eq}/cm^2$ , about one order of magnitude higher than the current tracker [10]. Additionally, the granularity has to be increased to achieve efficient tracking performance in spite of high pile-up which also makes track finding more difficult. Therefore, the Phase-2 tracker requires improved two-track separation and robust pattern recognition. As the amount of material in the tracking volume affects the event reconstruction, it should be reduced. Furthermore, the Phase-2

tracker will have an extended tracking acceptance up to about  $|\eta| = 4$  which improves the overall CMS physics capabilities [10].

The goal of including the tracking information into the L1 trigger is achieved by a new concept of module design which is applied in the Outer Tracker. Figure 2.2 presents the trigger concept. The tracker modules of the OT are composed of two single-sided closely-spaced sensors and on-board front-end electronics which correlate the signals [10]. If a particle hits the module at one sensor, an acceptance window is defined for the second sensor as trigger criterion. The hit pairs are called “stubs”. As the particle tracks are bend in the transverse plane by the magnetic field, the window corresponds to a threshold of transverse momentum ( $p_T$ ). That is why the OT modules are also referred to as “ $p_T$  modules”.

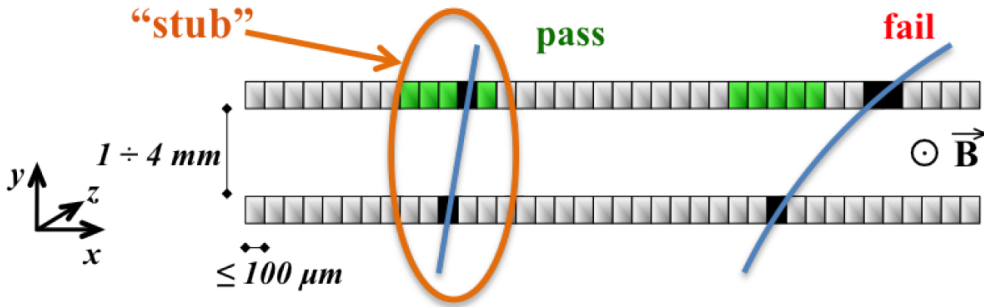


Figure 2.2: Trigger concept of the Phase-2 Tracker [3]. The correlation of the closely aligned sensors allows to define a trigger criterion. The hit pairs are referred to as stubs (black rectangles). Stubs lying within the acceptance window (green) correspond to high- $p_T$  particles. Low- $p_T$  particles are rejected.

Figure 2.3 shows a sketch of the Phase-2 tracker layout displaying one quarter in the  $r - z$  view. The Inner Tracker consists of four detection layers in the barrel part as well as eight small and four large double-disks per side. The double-disks are made of two disks which itself are formed of two D-shaped structures. The pixel size of the thin planar sensors is  $25 \times 100 \mu\text{m}^2$  or  $50 \times 50 \mu\text{m}^2$  which is a significant decrease of the pixel area compared to the Phase-0 and Phase-1 Inner Tracker pixel size of  $100 \times 150 \mu\text{m}^2$ . The total active surface is approximately  $4.9 \text{m}^2$ .

The Outer Tracker consists of six cylindrical barrel layers ( $|z| < 1200 \text{mm}$ ) and five endcap double-disks ( $1200 < |z| < 2700 \text{mm}$ ) [10]. So-called PS modules are installed in the first three barrel layers the endcap of the OT at radial distances from the beam axis between 20 and 60 cm. “PS” is an acronym for “pixel-strip” because the modules are composed of a strip and a macro-pixel sensor. The strip sensor is instrumented by  $2 \times 960$  strips with a pitch<sup>3</sup> of  $100 \mu\text{m}$  which are connected via wire bonds to the front-end (FE) hybrids at two opposite sides of the module. The macro-pixel sensor has  $32 \times 960$  macro-pixels with a pixel size of  $1.5 \text{mm} \times 100 \mu\text{m}$ . There will be three different variants of the PS module: the differences

<sup>3</sup>“Pitch” is a common term for the distance between strips of strip sensors.

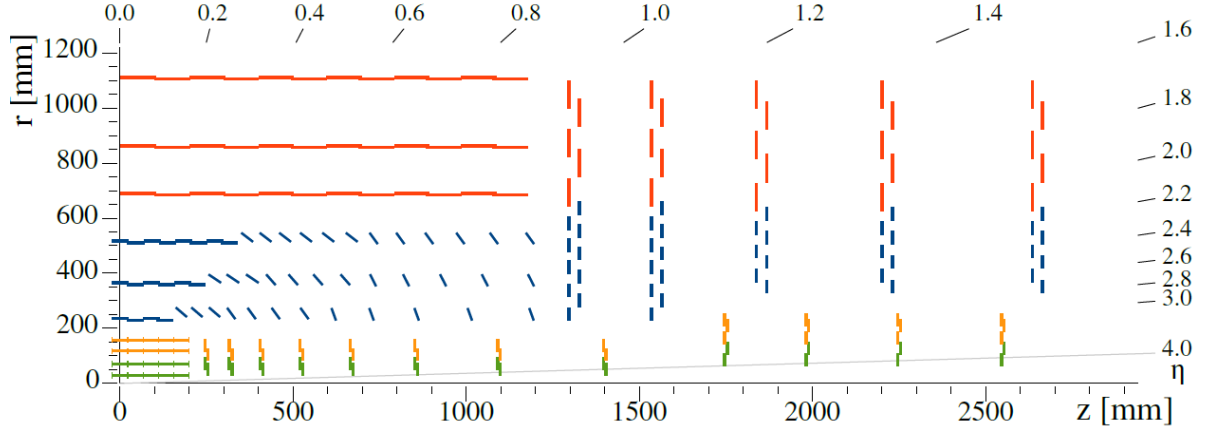
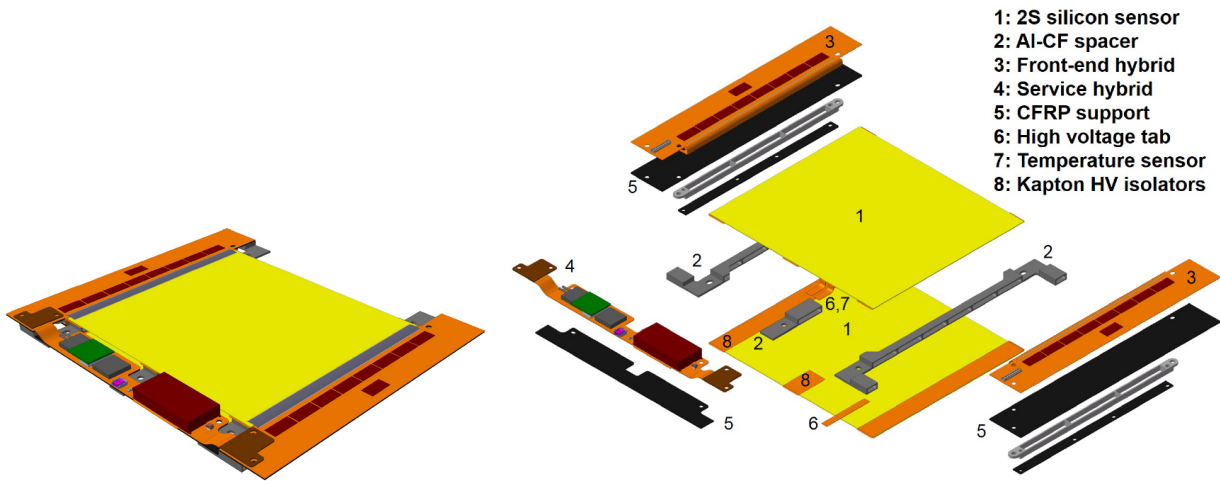


Figure 2.3: Sketch of the Phase-2 tracker [10]. One quarter of the tracker is displayed in the  $r - z$  view. The Inner Tracker consists of pixel modules with two (green) and four (yellow) readout chips. The Outer Tracker is built up of PS modules (blue) and 2S modules (red).

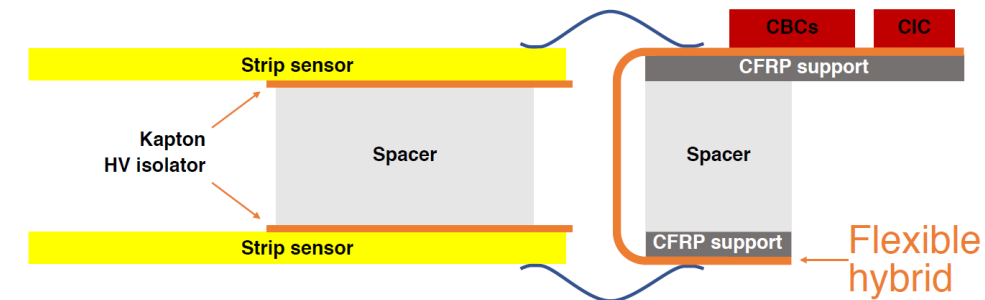
relate to a variation of the distance between the two sensors which will be realized with values of 1.6 mm, 2.6 mm and 4.0 mm. As shown in Figure 2.3 the PS modules are mounted parallel to the beam-axis in the central part of the barrel. PS modules covering  $|\eta| > \sim 0.6$  are mounted with a tilted angle with the active surface lying approximately perpendicular to the trajectory of the particles. The OT endcap is realized analogously to the concept of the IT with double-disks with PS modules in the inner part ( $r < 70$  cm). The total number of PS modules in the Phase-2 OT is 5616 with about half of the modules installed in the barrel and the other half in the endcap.

The 2S modules (shown in Figure 2.4 (a)) are installed in the outermost three layers of the barrel (arranged in parallel to the beam axis) and in the outer part of the five double disks ( $r > 70$  cm) [10]. The name “2S” corresponds to the two strip sensors composed in the 2S module. Each of the two strip sensors provides  $90 \text{ cm}^2$  active area achieved by two rows of 1016 strips with a length of about 5 cm and a pitch of  $90 \mu\text{m}$ . The strips are electrically connected to the flexible FE hybrids on both sides of the module (Figure 2.4 (b) and 2.4 (c)) via wire bonds. The wires are made of aluminum and have a diameter of  $25 \mu\text{m}$ . The sensors are separated by spacers made of aluminum / carbon fibre composite (Al-CF) which are electrically isolated by a Kapton strips glued onto the contact area of the sensor. The material of the spacers is chosen because of high thermal conductivity to achieve efficient heat removal and because its thermal expansion is well matched to silicon [10]. There are two versions of the 2S module with a variation in the distance between the sensors being 1.8 mm and 4.0 mm. The FE hybrids are supported by carbon fibre reinforced polymer (CFRP) and folded around Al-CF spacers to provide the connectivity to the top and bottom sensor and to achieve the height of the two sensors. This is done to minimize the length of the bonded wires between the hybrid and the sensor [10]. A FE hybrid uses eight CMS Binary Chips (CBCs) to readout 127 strips of each of both sensors. The additional Concentrator

Integrated Circuit (CIC) collects data from eight CBCs and acts as a data hub to the service hybrid which is used for powering and the communication to the counting room. Therefore the service hybrid provides DC-DC converters to generate the required voltages for the electronics, the LpGBT (Low-power Gigabit Transceiver) for serialization and the VTRx+ (Versatile TRansceiver plus) optoelectronic transceiver enabling bidirectional optical data transfer. The connection to the FE hybrids is realized either through miniature connectors or via wire bonds.



(a) Sketch of the assembled 2S module. (b) Overview of the composition of the 2S module.



(c) Side view of the 2S module. The blue lines show the wire bonds which connect the sensor strips with the CBCs.

Figure 2.4: Sketches of the 4.0 mm version of the 2S module [10].

# 3 Wire Bonding

This chapter deals with the wire bonding. In Chapter 3.1 an overview is given explaining the process itself and introducing the most relevant parameters which need to be optimized. Then the procedure of wire bond quality tests is introduced in Chapter 3.2. In the following chapter the setup used for wire bonding and quality checks is presented. Chapter 3.4 then deals with the procedure of the parameter optimization. The wire bonding on the 2S modules for the CMS Phase-2 Upgrade is discussed in Chapter 3.5 and first results from the bonding of a 2S dummy module are presented.

## 3.1 Overview

Wire bonding is a well-established method for electrical connections used in a broad field of semiconductor device fabrication since the 1970's [16]. This connection method uses ultrasonic power (US power) and pressure applied by a fine tool called *wedge* to achieve the welding of the connecting wire onto the bond surface. Depending on the material used, the wire diameter and form, wire bonding is differentiated between *wedge-wedge-bonding* and *ball-wedge-bonding* [17]. The *ball-wedge-bonding* method is usually used with gold wires. The wire is heated forming a ball and welded onto the surface using the wedge. Wirebonding is further differentiated related to the diameter and form of the used wire. Usually wires with a diameter in the range of 12-75  $\mu\text{m}$  are categorized as *thin wires*, whereas thicker wires up to diameters of 500  $\mu\text{m}$  are called *heavy wire*. Instead of round wires, wirebonding is also possible with ribbons which are also categorized into *thin* and *heavy ribbon* depending on the ribbon width and thickness. This work only deals with thin wire wedge-wedge-bonding, which will be described in detail in the following.

Figure 3.1 shows step-by-step the process of wedge-wedge-bonding. The aluminum wire is guided through the bond machine to the bond wedge where it is threaded through a hole to the bottom side of the bond wedge [18]. A clamp fixes the wire in this position. The first connection point is made (picture 1) by moving down the bond wedge onto the bond surface and applying a well-defined force which in this thesis is called *touchdown force (TDF)* to achieve a pre-deformation. Then (picture 2) the US power is activated while a force is still applied to the wire. This force is called *bond force (BF)*. The welding process is divided into three phases [18]:

1. In the first milliseconds (between 4 and 10 ms) the deformation is low and the increase of temperature is slow. The bond wedge rubs the wire on the surface which removes the thin oxide layer of the wire and small contamination on the surface. Therefore this phase is called the **cleaning phase**.
2. The wire deformation and the temperature both increase while most of the energy is used to flatten the metal surface. The atomic lattices of the metals get close together and the wire partially melts onto the surface. The bond wedge rubs on the wire, which is almost at rest. This phase is called the **mixture phase**.
3. The deformation applied in this phase is small and the frictional heat at the bond wedge and the wire is conducted to the bond surface. This temperature increase supports the stabilization of the welding by diffusion. So this phase is called **diffusion phase**.

After welding the first bond connection, the clamp opens and the bond wedge is moved to the second connection bond (picture 3 and 4 in Figure 3.1). The path of the bond wedge from the first bond to the second is called **loop**. Figure 3.2 shows exemplarily the most simple setup for the loop. The wedge is moved vertically upward for a distance which is called *Z-Loop Presign*. During the upward motion the wedge is moved in the direction of the second bond (*XY Loop Height Factor*) until the *Loop Height* is reached. Then the wedge is moved to a certain height (*Turn Height 2nd Bond*) above the second bond. As a last step the wedge is vertically moved down to the programmed position of the second bond. It is important to note that this is not the geometry of the wire but the movement which the machine is applying on the bond wedge. The user can decide the point where the clamp is closed. Usually this is done at the reached bond height, at the turn height or just before the second bond is made [17]. For the welding of the second connection bond, point 1 and 2 of Figure 3.1 are repeated. A third (and also more) connection(s) can be done by simply repeating this procedure which is then called **stitch bonding** [17]. After welding of the last bond, the wire is torn off by moving up the bond wedge with the clamp closed.

The *transducer* is mechanically coupled to the bond wedge and creates the US power which is applied on the wire. The commonly used frequencies for wedge-wedge-bonding are in a range of 40 to 160 kHz [19]. For thin aluminum or gold wires usually frequencies between 100 and 140 kHz are used. The amplitude of this oscillation for this kind of wire is in the order of 1 to 2  $\mu\text{m}$ . For heavy wire bonding lower frequencies and higher amplitudes are preferred. The right choice of frequency also depends on how soft and damageable the bonding material is. Higher frequencies have the advantage that less deformation is needed to achieve a strong connection and thus the risk of damaging the material is reduced, especially if thin surfaces are bonded. Furthermore, high frequencies also allow good bond results in case of a soft surface. The disadvantage of higher frequencies is a very small window of parameters and therefore less flexibility in the process. Lower frequencies and higher amplitudes on the

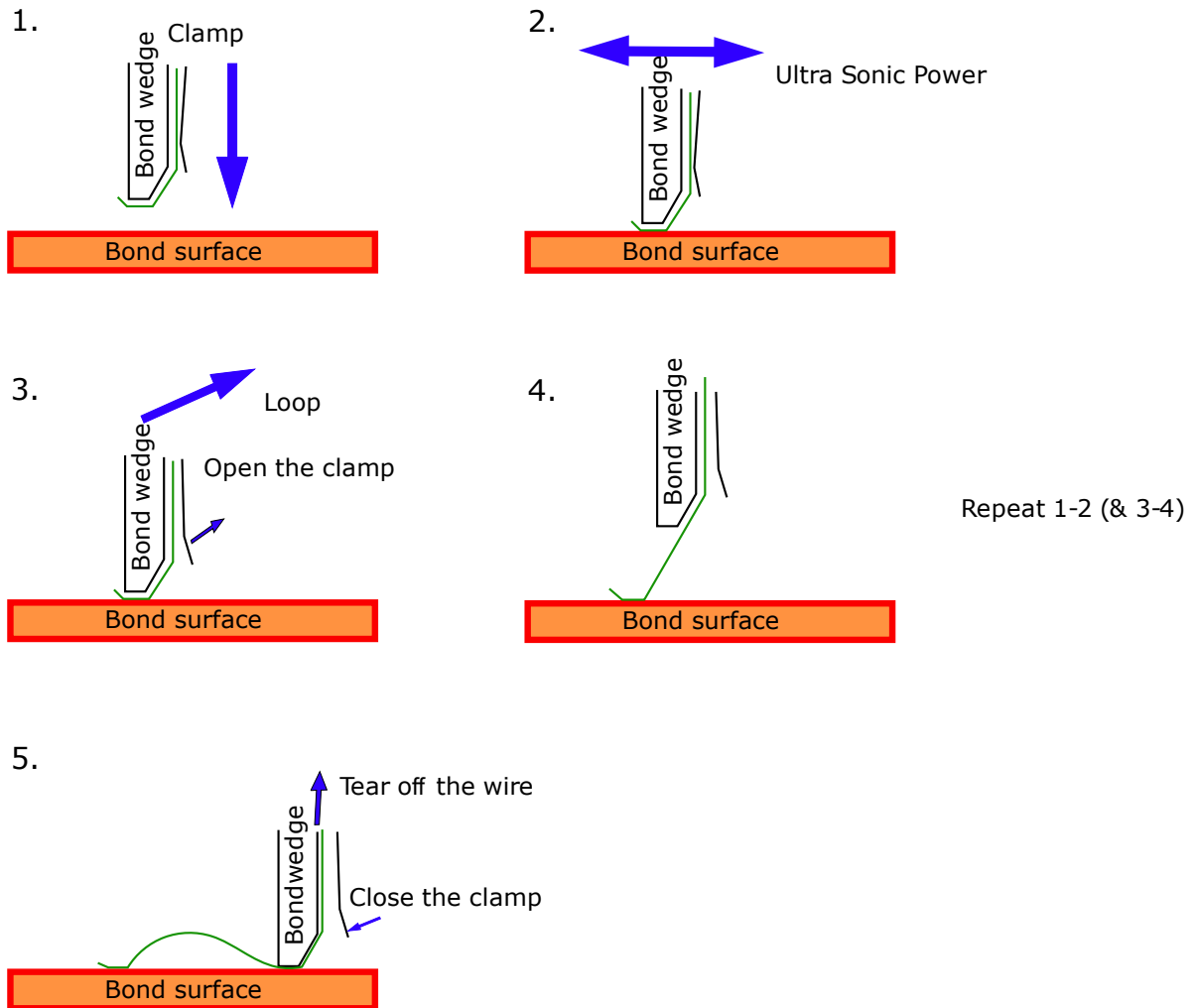


Figure 3.1: Procedure of wedge-wedge-bonding. The green line represents the aluminum wire.

other side allow wire bonding on coarse surfaces by flattening it, with the risk of damaging especially thin materials.

Bond wedges are available in various sizes and material. Figure 3.3 shows two photographs of the bond wedge used for this theses. The bond wedge is usually described by the manufacturers using the marked measures. The front view of the bond wedge is shown in Figure 3.3 (a). The wedge tapers to the tip which has a width described by the parameter  $W$ . If wires have to be bonded on very fine structures or with small distance to each other, a small width should be preferred. The wedge has a slight groove at the tip in which the wire is lying in. Figure 3.3 (b) shows the side view of the bond wedge. By using a wedge with a small hole diameter ( $H$ ) the wire guiding can be improved but also the friction of the wire at the bond wedge increases. The parameter  $BL$  (sometimes  $BF$ ) is the length of the effective bond plane. A larger length can significantly increase the strength of the connection, but more space is needed. The so-called back-radius and front-radius of the bond plane are indicated

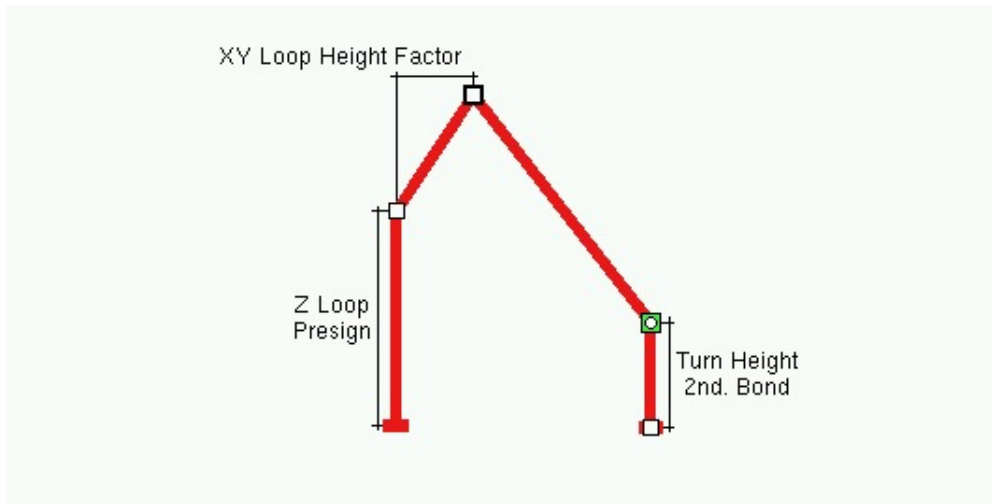
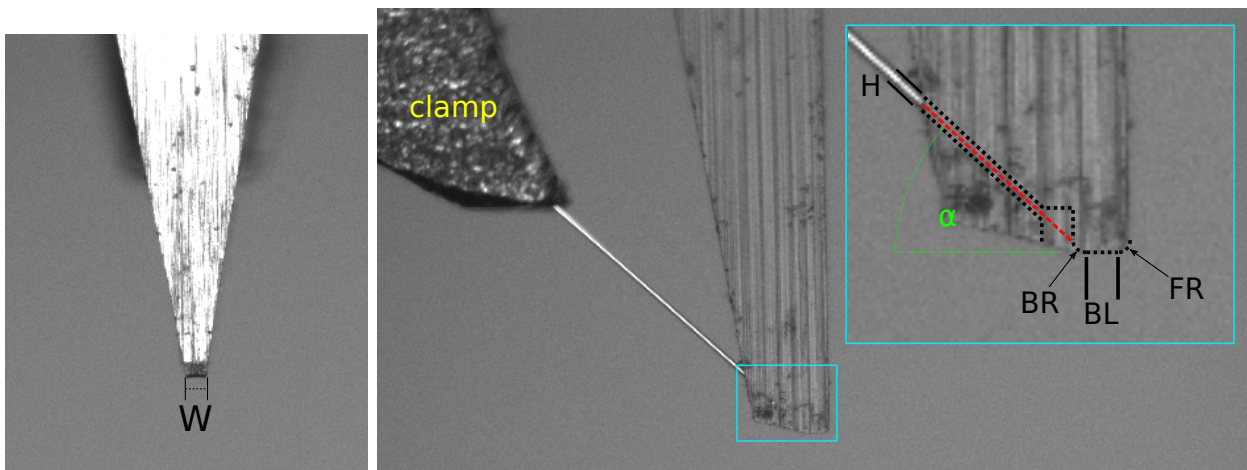


Figure 3.2: Screenshot of the bonding machine software panel for the loop geometry.

by  $BR$  and  $FR$ . The angle  $\alpha$  represents the slope at which the wire is guided to the bond plane. The higher this angle is the less space is needed for the bond wedge but the more stress is applied on the wire while the bonding process.



(a) Front view of the bond wedge.

(b) Side view of the bond wedge.

Figure 3.3: Photographs of the bond wedge taken using the *Tool Check* mode of the bond machine. The red dotted line indicates the position of the wire inside the wedge. The cutout regions and important areas of the bond wedge are highlighted by the black dotted line.

## 3.2 Quality Test Procedure

### 3.2.1 Wire Pull Test

It is very important to perform well defined quality checks to optimize the process of wire bonding and to ensure connections with good quality. The most commonly used testing method for wedge-wedge bonds of thin wire is the pull test method [20]. Pull tests can be differentiated between two different modes:

- **Destructive pull test:** A test hook is carefully moved under the wire to be tested. The hook is then vertically<sup>1</sup> moved up with a defined velocity until the wire breaks. The force that has been applied when the wire broke is measured and the type of failure is documented. The different failure modes are shown in Figure 3.4. The failure is called *Lift-off* if the whole wire lifts off from the surface. If the wire breaks directly at the heel of the bond, the failure mode is called *heel break*. A third failure mode which is called *wire break* is defined by a break of the wire far away from the bonds, usually in the region where the test hook is positioned.
- **Non-destructive pull test:** Again the test hook is carefully moved under the wire. Instead of pulling the wire until it breaks a force is defined which is applied on the wire for a defined time. The test is passed if the wire resists the force.

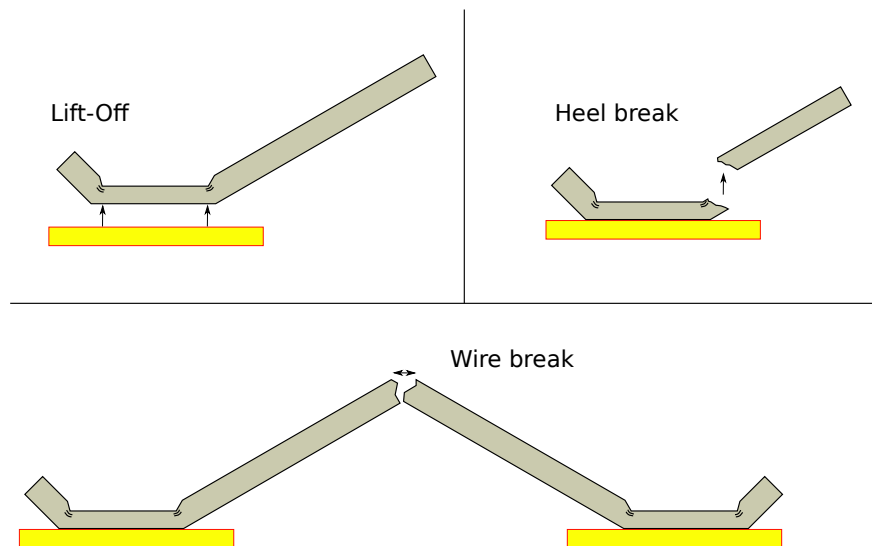


Figure 3.4: Failure modes for destructive pull tests.

If the quality of the whole bonding process should be quantified, the pull tests have to be performed with enough statistics. The manufacturer for wire bond machines *F&K Delvotec*

<sup>1</sup>It is not necessary to move the hook vertically but it is technically the most easy procedure. Additionally, all given correction factors are calculated for vertical movement and would have to be recalculated.

*Bondtechnik GmbH* recommends benchmark values for the passing of pull tests on wedge-wedge thin wire [20]. The benchmark values are shown in Table 3.1.

Minimum force of each pull test	$\geq 0.3 \times \text{WTS}$
Mean force of test series	$\geq 0.5 \times \text{WTS}$
Minimum non-destructive force	$0.2 \times \text{WTS}$
Lift-off	Not accepted
Relative standard deviation of test series	$\leq 0.15$

Table 3.1: Benchmark recommendation for pull tests on wire bonds from *F&K Delvotec Bondtechnik GmbH* [20]. The variable WTS represents the wire tensile strength which is specified by the wire manufacturer.

The effective forces  $F_1$  and  $F_2$  acting on the two bond connections depend on the wire loop shape and the position of the test hook. Therefore the correction factors  $K_1$  and  $K_2$  have to be taken into account. Figure 3.5 illustrates the parameters which are used to perform the calculation of the correction factors. The measured test force  $F$  is scaled by the correction factors to calculate the effective forces on the wire bond connections:

$$F_1 = K_1 \cdot F, \quad (3.1)$$

$$F_2 = K_2 \cdot F. \quad (3.2)$$

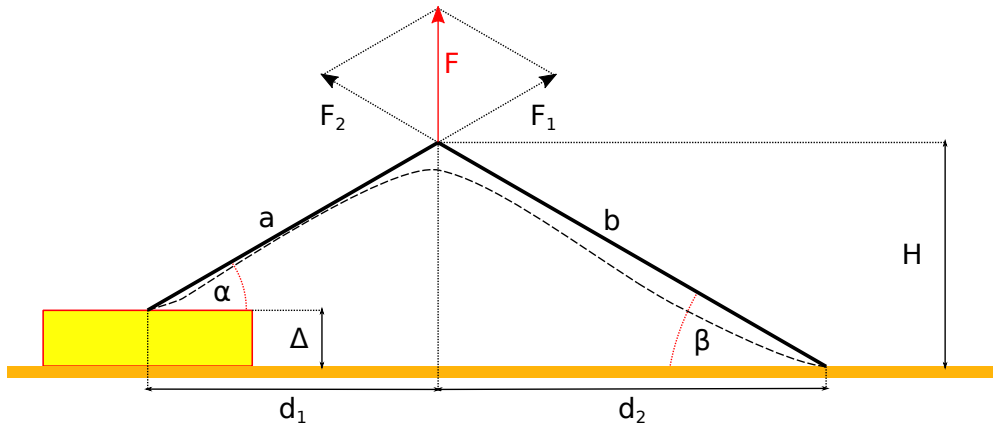


Figure 3.5: Sketch illustrating the calculation of the correction factors for pull tests.

The correction factors can be derived by a simple two-dimensional consideration of the applied forces which are called *simple formulas* in this thesis:

$$K_1^s = \frac{\cos \beta}{\sin(\alpha + \beta)}, \quad (3.3)$$

$$K_2^s = \frac{\cos \alpha}{\sin(\alpha + \beta)}. \quad (3.4)$$

*Fraunhofer Institute for Reliability and Microintegration* from Berlin together with *Berlin University of Technology* studied the forces of pull tests on wire bonds [21]. They developed a mathematical model based on the Capstan model which enables the calculation of the correction factors. The model includes the hook geometry and the friction force between hook and wire. They validated the model with experimental studies on heavy aluminum wire with a diameter of 300  $\mu\text{m}$ . The resulting correction factors are calculated as presented as follows:

$$K_1^D = \frac{1}{e^{0.3 \cdot (\alpha + \beta - (\text{sgn}(2\alpha - \beta) + 1)(2\alpha - \beta))} \sin \beta + \sin \alpha}, \quad (3.5)$$

$$K_2^D = \frac{1}{e^{0.3 \cdot (\alpha + \beta - (\text{sgn}(2\alpha - \beta) + 1)(2\alpha - \beta))} \sin \alpha + \sin \beta}. \quad (3.6)$$

*F&K Delvotec Bondtechnik GmbH* recommends to use Equation 3.5 and 3.6 to calculate the correction factors. Therefore these formulas are called *Delvotec formulas* in this thesis. As it is not clear that the mathematical model which forms the basis of these formulas also holds for thin wires with a diameter of 25  $\mu\text{m}$ , both types of formulas are considered to calculate the effective pull test force. *F&K Delvotec Bondtechnik GmbH* specifies Equations 3.3 and 3.4 to be simple approximation formulas which can be applied if  $\alpha$  and  $\beta$  do not differ by more than  $10^\circ$ . Figure 3.6 shows the relative difference of the correction factor  $K_1$  calculated with the two different formulas<sup>2</sup>. For  $\alpha = \beta$  indeed the two formulas produce the exact same value but already for a difference of  $10^\circ$  relative deviations of up to approximately 30% appear. The maximum relative deviation for  $\alpha$  and  $\beta$  in the range between  $5^\circ$  and  $65^\circ$  is about 57%. This shows that it is important to specify how the pull test is performed and how correction factors are calculated if pull test results are compared.

The variables needed for the calculation require that the wire is stretched. The accurate measurement of  $\alpha$  and  $\beta$  is difficult while a non-destructive pull test is performed. But again with simple geometric considerations both angles can be calculated with measurements using the microscope without applying any forces to the wire. The microscope is used to measure the length of the actually expended wire  $L$  and the distance between the two bonds  $d_1 + d_2$  which can be crosschecked with the value measured with the bonding machine. The parameter  $\Delta$  is measured by the bonding machine during the bonding process. Under

---

<sup>2</sup>The displayed value is calculated by  $(K_1^s - K_1^D) / K_1^s$ .

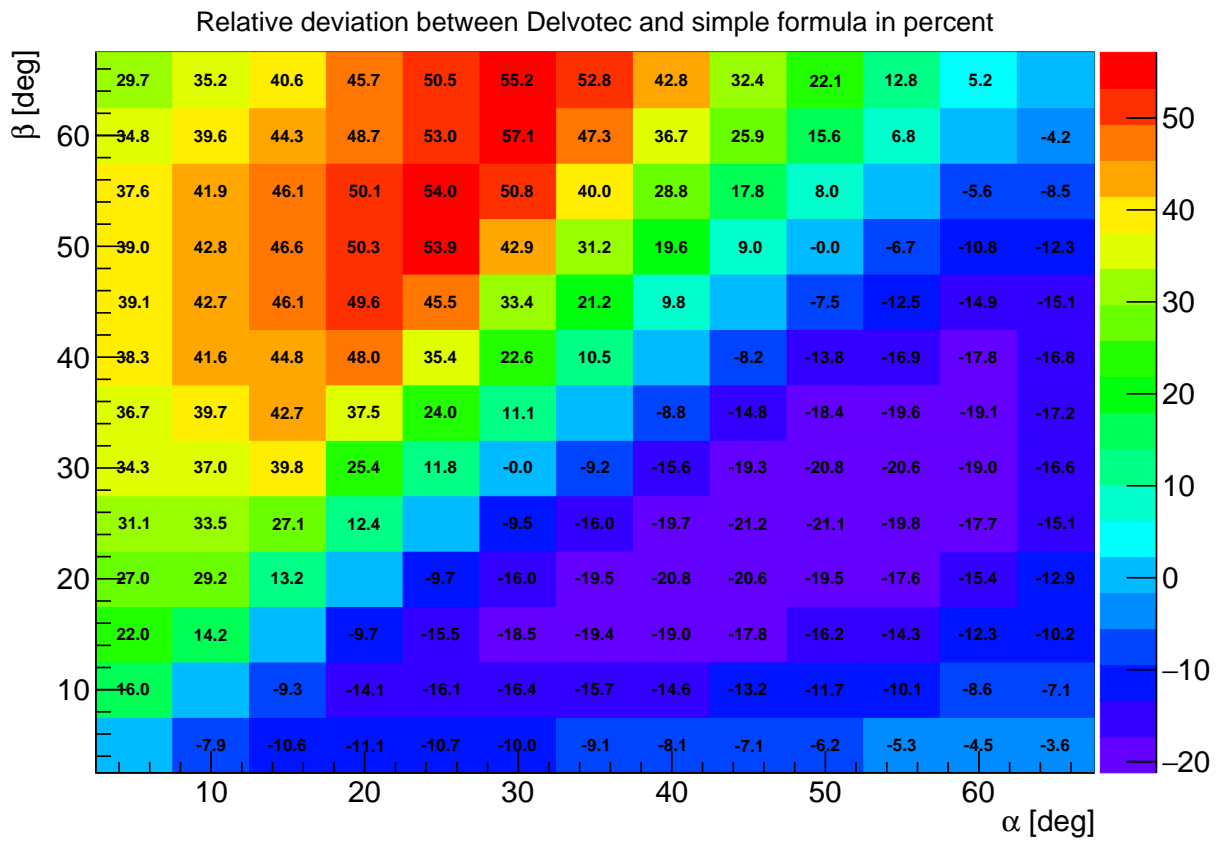


Figure 3.6: This plot shows the relative difference between the correction factors for the first bond calculated by using the Equations 3.5 and 3.3 for  $\alpha$  and  $\beta$  in the range of  $5^\circ$  to  $65^\circ$ .

the assumption that the elongation factor  $\epsilon$  given by the wire manufacturer is correct the following relation holds:

$$\epsilon L = \hat{L} = a + b = \sqrt{d_1^2 + (H - \Delta)^2} + \sqrt{d_2^2 + H^2}. \quad (3.7)$$

As all values of Equation 3.7 except  $H$  are given,  $H$  can be calculated:

$$H = \frac{\sqrt{d_1^4 \hat{L}^2 - 2d_1^2 d_2^2 \hat{L}^2 - 2d_1^2 \hat{L}^4 + 2d_1^2 \hat{L}^2 \Delta^2 + d_2^4 \hat{L}^2 - 2d_2^2 \hat{L}^4 + 2d_2^2 \hat{L}^2 \Delta^2 + \hat{L}^6 - 2\hat{L}^4 \Delta^2 + \hat{L}^2 \Delta^4}}{2(\hat{L}^2 - \Delta^2)} + \frac{-d_1^2 \Delta + d_2^2 \Delta + \hat{L}^2 \Delta - \Delta^3}{2(\hat{L}^2 - \Delta^2)}. \quad (3.8)$$

Then  $H$  can be used to calculate  $\alpha$  and  $\beta$ :

$$\alpha = \arctan\left(\frac{H - \Delta}{d_1}\right), \quad (3.9)$$

$$\beta = \arctan\left(\frac{H}{d_2}\right). \quad (3.10)$$

Based on these formulas a numerical analysis of systematic uncertainties can be performed for every loop geometry that is checked via pull tests. This is especially important if pull test results of different test series are compared because the position of the pull hook ( $d_1$  and  $d_2$ ) will actually change. Within a single test series the position can be assumed to be quite constant. As different loop geometries are used in this theses, the error estimation and consideration of the relevance of the systematic uncertainties is discussed in the corresponding chapters.

### 3.2.2 Visual Inspection

Besides the presented pull test methods it is also recommended to perform visual inspections of the wire bonds [20]. Using an appropriate microscope, the bond surface has to be checked for damages and contamination because dust particles and grease on the bond surface effectively degrade the quality of the wire bond. Additionally, the position and shape of the bond contacts have to be controlled. *F&K Delvotec Bondtechnik GmbH* recommends to measure the deformation  $B$ , tail length  $T$  and asymmetry of the bond contact  $B_{max}/B_{min}$  and also specifies benchmarks. These parameters are visualized in Figure 3.7. The benchmark values for these criteria can be found in Table 3.2. Also, the loop shape and uniformity should be checked.

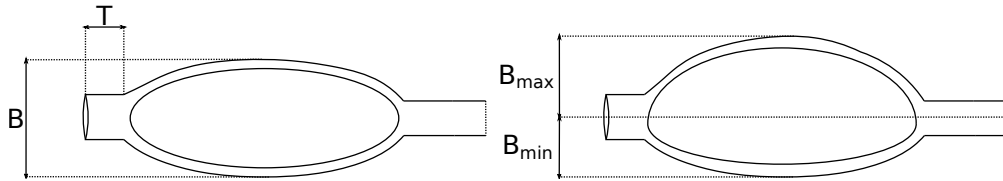


Figure 3.7: Sketch visualizing the most relevant measures for visual inspections.

Deformation $B$	$\leq 2 \times \text{WD}$
Asymmetry $B_{max}/B_{min}$	$\leq 1.25$
Tail length $T$	$\leq 3 \times \text{WD}$

Table 3.2: Benchmark recommendation for the visual inspection of wire bonds from *F&K Delvotec Bondtechnik GmbH* [20]. The variable WD represents the wire diameter.

## 3.3 Setup

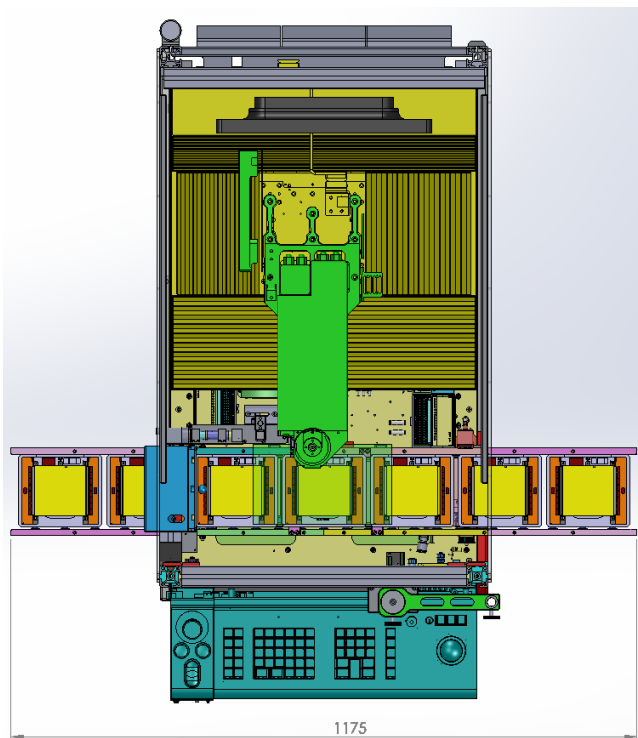
### 3.3.1 Bonding machine and bonding equipment

The bonding machine has been purchased mainly for the series production of the 2S tracker modules for the Phase 2 Upgrade of the CMS detector. Thus some mandatory features have been defined for the purchasing of the machine:

- The bonding machine should be able to be filled with at least four modules and process those without requirement of manual interaction of the operator. Furthermore it should have a pattern recognition system installed.
- The machine should provide process control features.

The first feature was required to enable automated wire bonding. This simplifies the production of a high quantity of detector modules. Also the production rate might be increased. The process control feature was requested because it enables analysis-based optimization of the bond process with the objective of reducing the error rate and increasing the quality (and also maybe the lifetime) of the detector module. A reduced error rate would additionally further reduce the number of manual interactions of the operator during the bonding process. Monitored data could also be used for the development of a software to fast and efficiently identify potentially bad bonds.

The specifications have been fulfilled by the *Bonder 64000 G5* machine acquired from *F&K Delvotec Bondtechnik GmbH* [22]. The automatized processing of four modules is realized by a conveyor system. The system is visualized in Figure 3.8 (a) which shows a sketch of the bonding machine from a top view. Figure 3.8 (b) presents a photograph of the actual bonding machine located in the bond lab at the Physics Department of University RWTH Aachen. In principal, the conveyor system enables a permanent filling and unloading of the machine without the requirement of stopping the bonding process.



(a) A technical sketch of the bonding machine. The sketch was designed and provided by *F&K Delvotec Bondtechnik GmbH*.

(b) Photograph of the bonding machine in the bond lab.

Figure 3.8: The bonding machine.

The *Bonder 64000 G5* provides a so called Bond Process Control (BPC) system [18, 22]. Instead of applying a constant US power for a constant time, the BPC measures and analyzes the wire deformation to regulate the US power while bonding if this is necessary and stops the machine when a defined target deformation is reached. However, this feature only supports the bonding process. Bond parameters as well as BPC parameters still have to be optimized. The time development of the wire deformation is displayed during the bonding process. The operator can use this feature to immediately identify errors and adjust bond parameters, if necessary. Figure 3.9 presents an example of a deformation curve that is shown and saved for offline analysis during the wire bonding. The machine saves seven data points<sup>3</sup> of time and deformation of each bond. The deformation is measured using a proximity sensor which measures the downward motion of the wedge after the registration of the touchdown. The adjustment of the US power has been implemented because the phases of wire bonding (described in Chapter 3.1) require different levels of energy deposition [18]. Stopping the machine after a reached target deformation prevents so called over-bonding, which degrades the quality of the bond. The measured deformations, bonding times and other machine

<sup>3</sup>Data points are saved at 10 %, 20 %, 30 %, 50 %, 70 %, 90 % and 100 % of the maximum deformation value.

parameters are stored and available for further offline analyses. *F&K Delvotec Bondtechnik GmbH* does not specify uncertainties of the measured values.

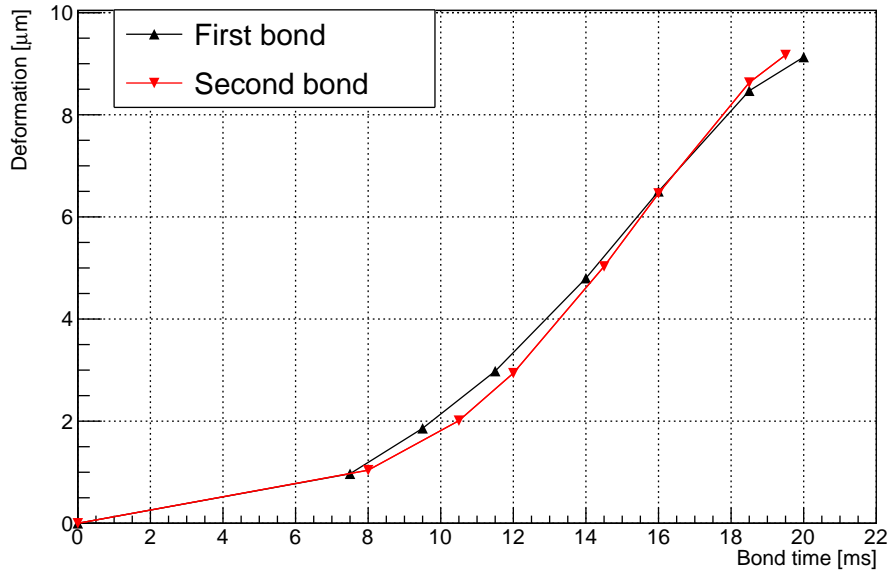


Figure 3.9: Example of a deformation curve which is displayed during the wire bonding process and saved for offline analysis.

The bonding wedge *UT45A-W-2525-1.00-C* by *Small Precision Tools* has been used for this theses [23]. The relevant parameters as described in Chapter 3.1 and shown in Figure 3.3 on page 14 are summarized in Table 3.3:

Material	H	$\alpha$	BL	BR	FR	W
Tungsten carbide	64 $\mu\text{m}$	45°	64 $\mu\text{m}$	25 $\mu\text{m}$	25 $\mu\text{m}$	102 $\mu\text{m}$

Table 3.3: Properties of the used bonding wedge *UT45A-W-2525-1.00-C* [23].

This bonding wedge is designed for wire bonding of aluminum wire with a diameter between 25 and 33  $\mu\text{m}$ . The work for this theses has been done using aluminum (with 1 % silicon) wire with a diameter of 25  $\mu\text{m}$  from a 100 m spool by *Heraeus* [24]. The wire tensile strength is specified to be 15-17 cN with an elongation of 1-4 %.

The conveyor system and the technical arrangement within the bonding machine have been designed for wire bonding with the bonding jig for the 2S module which holds the module using vacuum and supports the bond surface. The design of the jig has been performed by CERN<sup>4</sup>. Figure 3.10 displays the bonding jig for the 2S module. The jig is made of aluminum. The six black vacuum cups adhere to the bottom sensor. The cups are made of conductive silicone rubber to prevent electrostatic discharge (ESD). As the vacuum of

<sup>4</sup>Few modifications have been made for the compatibility of the bonding jig to the machine.

the bonding machine is activated the module is pulled down so that the bottom sensor lies on the surface surrounding the vacuum cups. This surface is laminated with 100  $\mu\text{m}$  thin ESD-safe plastic foil. Two alignment pins located at the side of one FE-hybrid ensure that the module is in the right position. Both FE-hybrids are supported by aluminum rods whose contact areas with the module are again laminated with ESD-safe plastic foil. The height of the support racks can be adjusted using screws at the side.

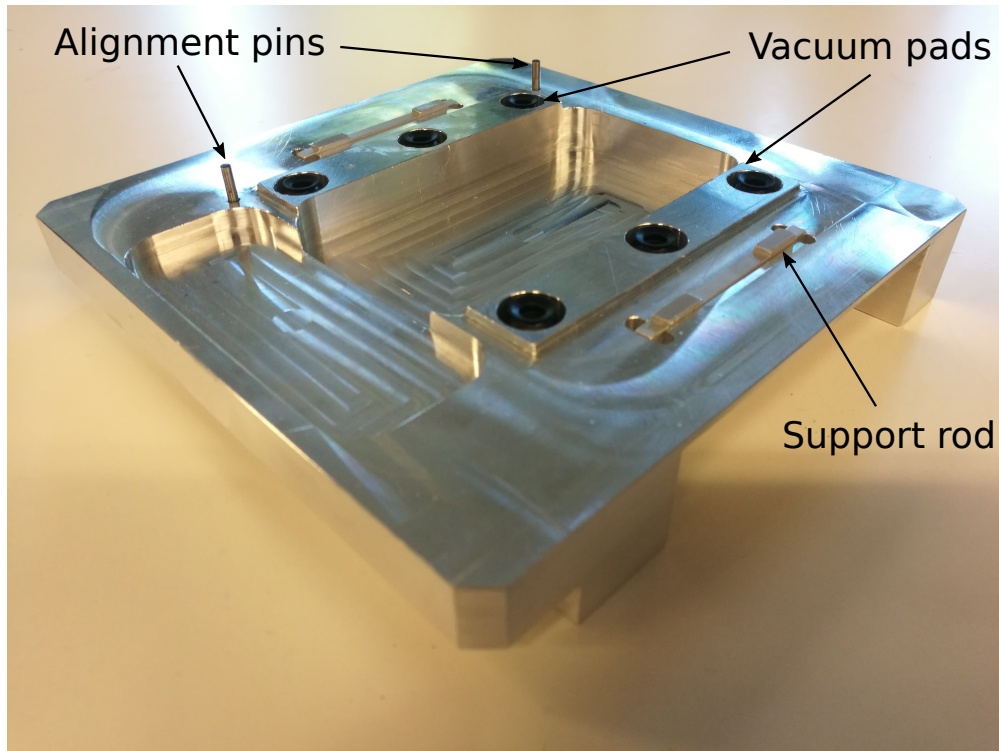
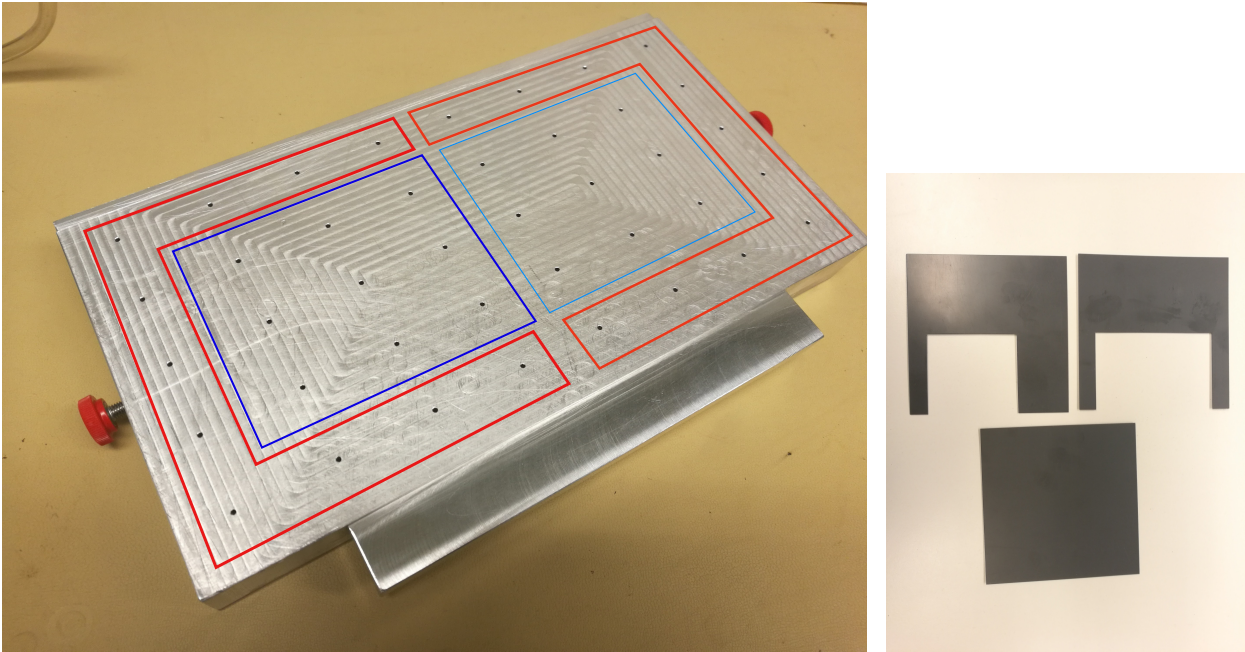


Figure 3.10: Photograph of the wire bonding jig for the 2S module.

For probes with a flat bottom side another jig has been designed. A photograph of this *standard-jig* is shown in Figure 3.11 (a). On the top side of the jig are 40 holes which are connected to the vacuum. They have a diameter of 2 mm and distances of about 3.2 cm in  $x$ -direction and about 2.4 cm in  $y$ -direction of the machine to each other. The  $x$ -direction points to the movement direction of the conveyor system and the  $y$ -direction is perpendicular to it. The dimensions of the standard jig are chosen so that the working area of the bonding machine is utilized in the maximum possible way with 254 mm ( $x$ )  $\times$  134 mm ( $y$ ). The regions which are connected to the vacuum can be selected by switching the screws on the left and the right side of the standard jig. The selectable regions are highlighted in blue and red in Figure 3.11 (a). Using plastic templates with cut-outs of different sizes (Figure 3.11 (b)) the vacuum region can be further customized.



(a) Photograph of the standard-jig with highlighted regions for the vacuum access.

(b) Photograph of plastic templates with different cut-out sizes.

Figure 3.11: Standard jig.

### 3.3.2 Quality Checks

The pull tests are performed using the pull test machine *Dage Series 3000* [25]. Figure 3.12 shows a photograph of the pull test machine. The technical data sheet does not provide any information about uncertainties. In order to optimize the accuracy of the pull test results, calibrations are performed regularly with the internal calibration mode. For the chosen setup range of 25 g calibration weights of 25 g, 10 g, 5 g and 2 g are used. After adjusting the correct position of the calibration hook to pull the weights, they are lifted six times and the mean value is used to check the linearity. The machine outputs test result values with significant numbers down to milligram in the chosen range. Thus systematic uncertainties generated by the pull test machine are assumed to be suppressed by systematic uncertainties from variations in the positioning of the test hook and statistical uncertainties.

The pull tests performed for this theses have been done with the pull test hook *4000-HK-5-2* by *Dage* with a length of  $125\ \mu\text{m}$  and a diameter of  $50\ \mu\text{m}$ . The setup pull velocity is  $500\ \mu\text{m s}^{-1}$ .

The efficiency of the test procedure has been improved by connecting the pull test machine's RS-232 output port with an external computer via a null-modem cable with USB-converter. The pull test results are automatically stored and formatted for further analyses.

Visual inspections are done using the microscopes installed on the bonding machine (*Nikon SMZ460* [26]) and on the pull test machine (*Nikon SMZ645* [27]). For quantitative anal-



Figure 3.12: Photograph of the pull test machine *Dage Series 3000*. An extra light source is positioned on top of the pull test machine. The installed hook is a special hook which is only used for calibrations.

ysis the digital microscope *VHX-900F* by *Keyence* with an implemented absolute scale is used [28].

## 3.4 Optimization of bond parameters

### 3.4.1 Boundary conditions

The studies of the optimization of the bond parameters have been performed under certain boundary conditions that have been kept stable. The conditions strongly differ from those which have to be faced in the module's series production because it is easier to understand the process and the different parameters if the tests are performed on substrates which are easy to support, flat and clean. Therefore Chapter 3.4 can be understood as a general study of the machine parameters and features and as a development of an optimization method which can be applied to other processes.

The studies presented in this chapter have been done on bonding test substrates by the manufacturer *Cicorel* which have been provided by *F&K Delvotec*. The plates consist of a material called *electroless nickel immersion-gold (ENIG)*. ENIG is specified to be a chemically applied layer of nickel of 3 up to 6  $\mu\text{m}$  with a top coating of at least 50 nm of gold [29]. Figure 3.13

shows a photograph of such a test substrate. The red colored square in Figure 3.13 exemplarily highlights the part of the structure which is used for test programs. This square region has an area of  $4 \times 4 \text{ mm}^2$ .



Figure 3.13: Photograph of the wire bond test material by *Cicorel*. The structure highlighted with red color indicates the regions used for test programs.

All tests have been programmed with the same loop setup and logic to achieve good comparability between the different test series. Figure 3.14 shows the geometry of the test programs. A bonding program consists of so called *chips*. A chip contains information about the height of the substrate but also the bond parameters and the loop parameters. For example this can be used to define different chips for the source and the destination bond which are placed on other materials and bond heights. So a different set of bond parameters can be defined for each different type of material. The loop parameters of the source chip are used for the wire bonding. For the test program presented in Figure 3.14 the chips are only used to easily define groups with different sets of parameters. Each group consists of eight wires with a loop distance of  $(1000 \pm 50) \mu\text{m}$  with twelve groups in total. Small deviations in the loop length appear because of programming-related issues. Variations in the loop length do not have an effect on the angles  $\alpha$  and  $\beta$  which are used to calculate the correction factors, because all loop parameters including the loop height scale with the loop distance. Within the groups the wires have a distance of  $100 \mu\text{m}$  to each other. The groups are separated by a distance in the order of  $250 \mu\text{m}$  to be able to clearly distinguish the groups from each other when quality checks are performed. The chips are defined with reference pictures of significant recognition features to align the wires if the substrate has been moved. In the test program, all chips use the opposite edges of the squares as reference marks.

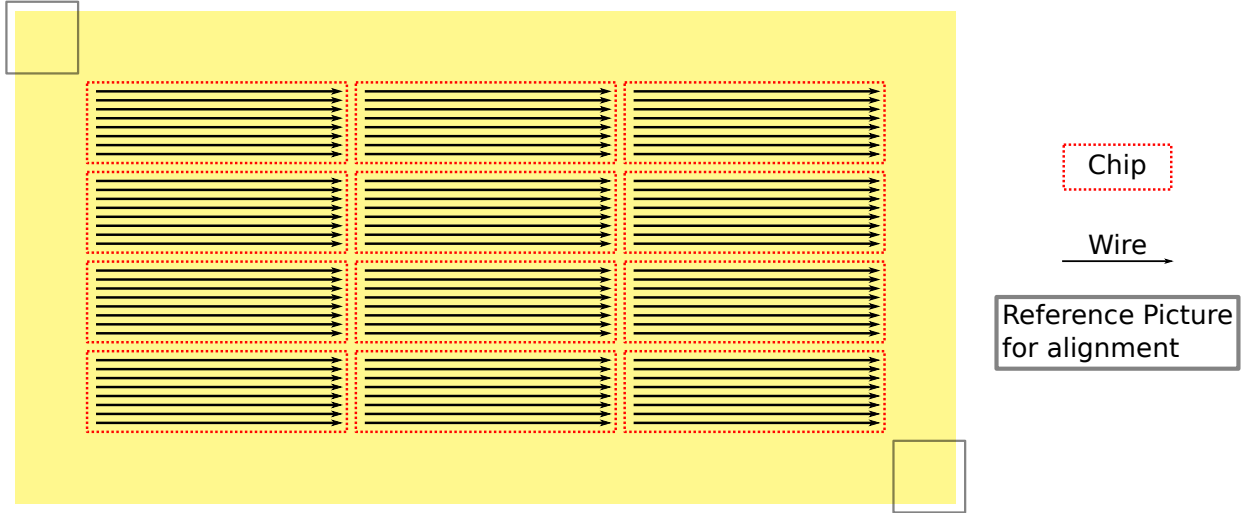


Figure 3.14: Sketch of the geometry of the test programs. The sketch is not to scale. The yellow area represents one of the  $4 \times 4 \text{ mm}^2$  squares.

The loop parameters have been chosen by eye so that the correction factors for pull tests are approximately  $K_1 \approx K_2 \approx 1$  (Chapter 3.2.1) and the wire is preferably symmetric<sup>5</sup>. Thus, locating the highest point of the wire as position of the test hook is easier and systematic uncertainties are thereby minimized. Figure 3.15 shows the wire geometry of the test program. The distance between the two bonds as well as the actual length of the wire are measured in numbers of pixels using the picture editing software *Inkscape 0.92* [30]. By using the measurement value of the loop distance in number of pixels and the bond machine setup value, a conversion factor can be calculated. For this, the measurements of the loop distance in number of pixels are averaged. This average value corresponds to  $1000 \mu\text{m}$ . The average value of the digitally measured wire length is converted to  $1270 \mu\text{m}$ . As a last step, the region where the test hook is set is determined. The estimated region is illustrated in Figure 3.15 as a red bar. The range for the parameter  $d_1$  is measured analogously as the wire length<sup>6</sup>. Table 3.4 summarizes the results of this procedure, which enable the calculation of the correction factor and systematic errors. It is important to note that  $d_1$  is kept quite stable within different pull tests (also within different pull test series) but the actual position is not known.

Loop distance $d_1 + d_2$	Wire length $L$	Position of hook $d_1$	
		minimum	maximum
$1000 \mu\text{m}$	$1270 \mu\text{m}$	$372 \mu\text{m}$	$567 \mu\text{m}$

Table 3.4: Results of digital measurements of the wire geometry realized in the test program.

<sup>5</sup>This is achieved if  $\alpha = \beta = 30^\circ$ .

<sup>6</sup>This also determines  $d_2$  because  $d_1 + d_2 = 1000 \mu\text{m}$ .

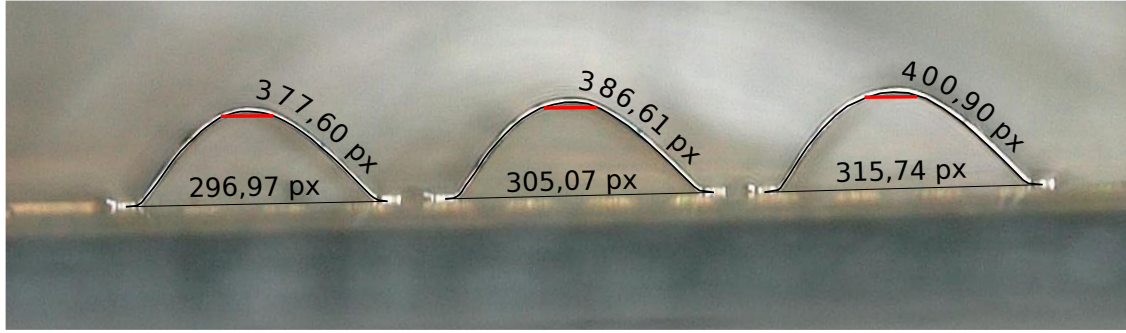


Figure 3.15: Microscope picture of the test program wire geometry. The red bar illustrates the estimated region of the position of the pull hook.

The measured values are used to calculate the correction factor as described in Chapter 3.2.1. Figure 3.16 shows the calculated correction factors  $K_1^D$  (using Equation 3.5) and  $K_1^s$  (using Equation 3.3) in dependence of  $d_1$ . Each correction factor is calculated with an elongation of 1% and 4%. The region contained in between the green dotted lines marks the estimated position of the test hook. The variation of the elongation factor results in a minor change of the correction factor but the different formulas used for the calculation differ strongly.

For the determination of a correction factor and systematic errors, both formulas are used with both elongation factors to calculate the correction factor with ten thousand randomly generated values for  $d_1$ . The generator uses a uniform distribution over the discussed  $d_1$  region. The correction factors are filled into histograms. Figure 3.17 shows those four histograms and Table 3.5 presents the mean and RMS values of the histograms. The correction factor calculated with all four calculation methods is about 0.8 and they are compatible within their uncertainties. The highest relative error on the effective pull test value of 14% is generated by the calculation using the Delvotec formula with 1% elongation. The corresponding correction factor is  $0.85 \pm 0.12$ . The smallest relative uncertainty of 4% is calculated for the simple formula with 4% elongation. Because it is not clear, which formula should be preferred, the worst case has to be taken into account. So the corrected pull test result has a systematic uncertainty of 14%.

Formula	Elongation	Correction factor $K_1$		
		Mean $\mu$	RMS $\sigma$	Relative error $\sigma/\mu$
Delvotec	1%	0.85	0.12	14%
	4%	0.82	0.11	13%
Simple	1%	0.81	0.03	4%
	4%	0.78	0.03	4%

Table 3.5: Summary of means and RMS of the histograms of calculated correction factors (Figure 3.17).

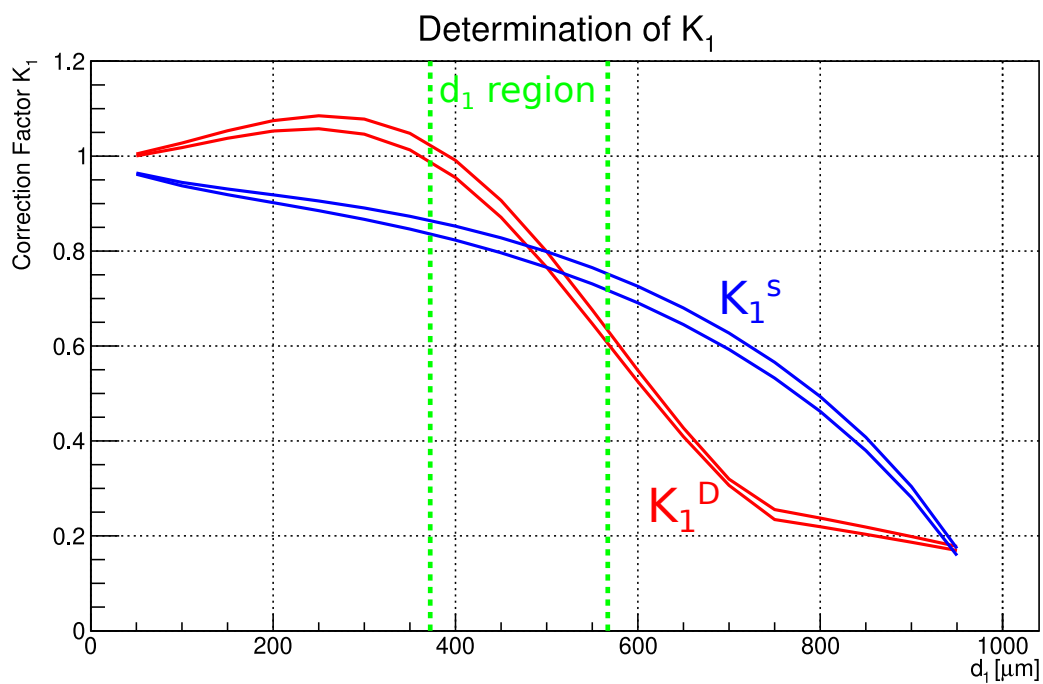


Figure 3.16: Calculation of the correction factor. The red curves shows the correction factor  $K_1$  calculated by using the Delvotec formula. The same correction factor calculated using the simple formula is displayed as blue curve. The upper curve of those is calculated with an elongation factor of 1%, the lower curve with an elongation factor of 4%. The region highlighted by the green dotted lines represents the estimated region of the hook position.

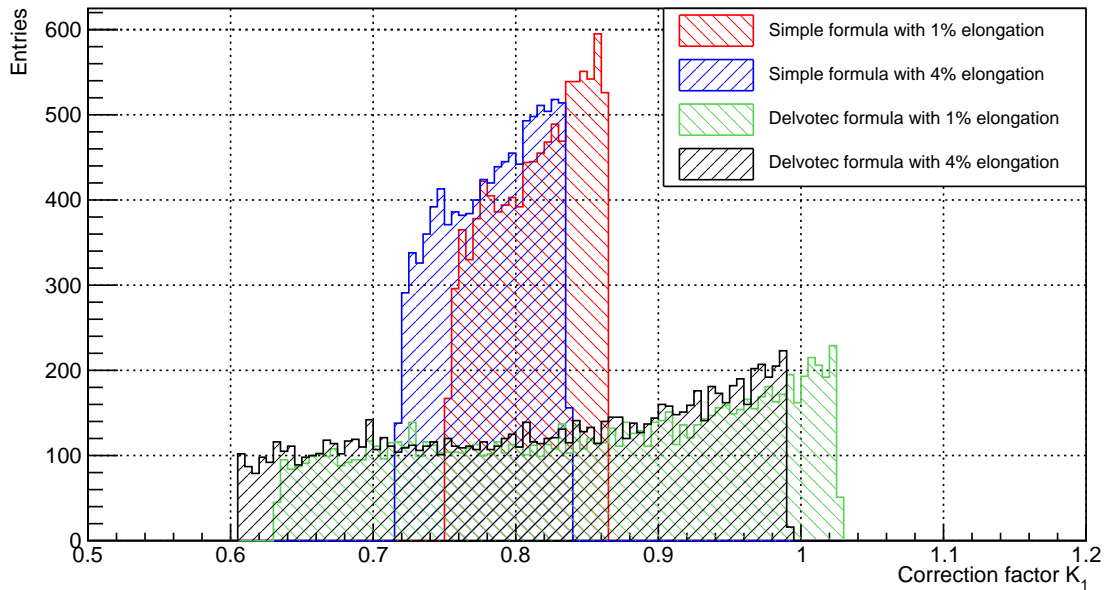


Figure 3.17: Randomly generated  $K_1$  using the two different formulas with an elongation of 1 or 4%.  $d_1$  is generated within the region highlighted in Figure 3.16.

From pull test to pull test the variation of the hook position is much smaller than the estimated region of the hook position. This variation is estimated to be at most 20 % (39  $\mu\text{m}$ ) of the region of the hook position (Figure 3.15 and 3.16). The worst case appears if the hook is positioned in the last 20 % of the test hook region because the slope of all four formulas is the highest there and the correction factor itself is the smallest. Figure 3.18 shows the distribution of the correction factors analogously calculated with both formulas. In this case the highest relative systematic uncertainty of 4.1 % is generated using the Delvotec formula with an elongation of 4 %. This systematic uncertainty has to be taken into account for each pull test result.

The studies presented in this chapter focus on the different parameters and their impact on the bond quality. The effective absolute pull force is less relevant than the effect generated by variations of the parameters. The correction factor would only scale the pull test result. Therefore all pull test results presented in this chapter are not corrected.

Only the correction factor  $K_1$  is studied because 99.7 % of all wires which have been pull tested have broke at the first bond. The first bond tends to be more fragile because the bending of the wire is much higher when the loop is made. Figure 3.2 on page 14 shows the loop setup for the test program. After the welding of the first bond the wedge is moved vertically upwards, while at the second bond the wire is only bend to reach the final position. This means that the pull test only gives information about the quality of the first bond. Because the test series have been performed on the described ENIG test material the first

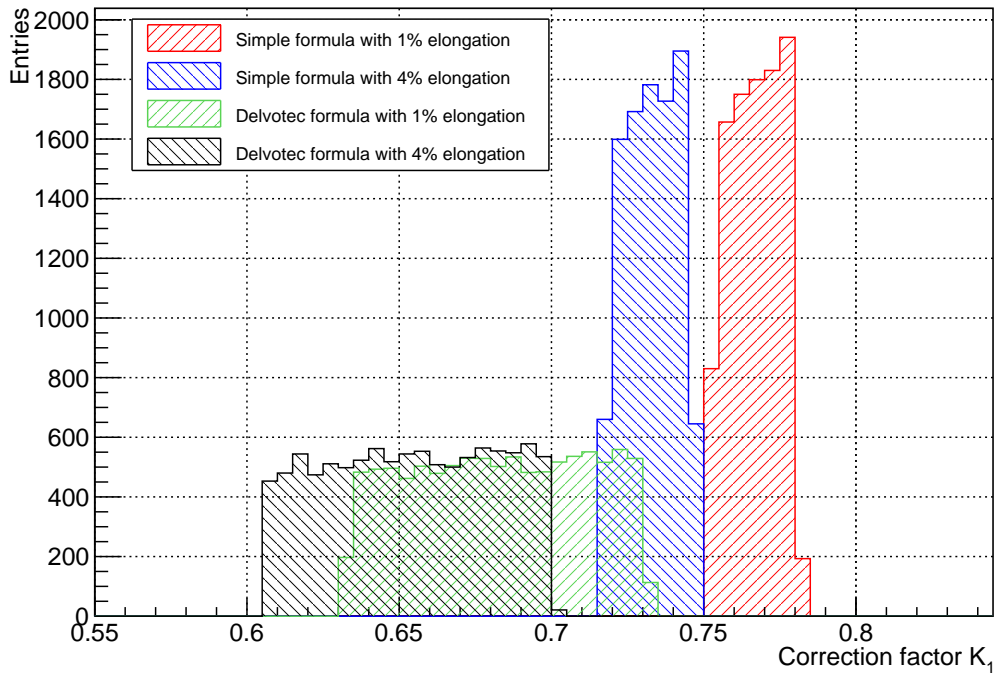


Figure 3.18: Randomly generated  $K_1$  using the two different formulas with an elongation of 1 and 4%.  $d_1$  is generated within the last 20% of the estimated region for the hook position.

and the second bond are made on the same kind of surface. So, the same set of parameters is used for the first and the second bond.

All tests presented in Chapter 3.4 have been performed using a module bonding jig because the standard jig has been in production at that time. Few modifications have been done to the jig to improve the support for the wire bonding. The vacuum pads and the ESD-safe foil have been removed on the side where the ENIG-plate is positioned because the material has not been pulled down onto the surface but lay on top of the flexible vacuum pads which effectively degraded the support.

### 3.4.2 Studies of the bond parameters with deactivated Bond Process Control

As a first step the different bond parameters are studied with deactivated Bond Process Control (BPC) to investigate their impact on deformation and especially on quality in terms of pull test results. The parameters which have been studied are US power<sup>7</sup>, bond force (BF), touchdown force (TDF) and bond time (BT). Each test series uses the set of default

<sup>7</sup>The US power is set up with the unit *digit*. This is a pure machine-related unit as it is internally converted in a power by the US power generator. There is no information available how the digit value converts to an actual power.

parameters shown in Table 3.6. Also the test range of each parameter is summarized in Table 3.6. The default parameters are set arbitrary but in a way that the wires most certainly do not fail.

Parameter	US power [digits]	BT [ms]	TDF [cN]	BF [cN]
Default value	85	30	30	30
Test range	60 .. 100	5 .. 60	7 .. 60	20 .. 42

Table 3.6: Default parameters for first parameter studies.

One parameter is varied and the remaining three are kept constant in every test series. In the following the different test series are discussed. Each set of parameters is tested with eight wires.

### Variation in US power

The US power is varied in the range from 60 to 100 digits. Figure 3.19 shows the wire deformation dependence on the setup value of the US power. The wire deformation value is measured by the bonding machine. The blue triangles indicate the maximum and minimum values. The displayed error is the standard deviation of the deformation distribution per setup value of US power. The graph shows the expected behavior: when the US power is increased, the wire deformation increases. The deformation increases linearly from about 4 to 16  $\mu\text{m}$  over the tested range of US power.

The development of the deformation slope is shown in Figure 3.20. The plotted slope is determined by calculating the slope of the line through neighboring data points of the deformation curve of each tested wire (Figure 3.9 on page 22). The time value of the plotted points is the mean value of the data points used for the slope calculation. The shape of the slope distribution is almost independent of the actual US power setup. The slope rises until about 15 ms and then falls slowly. This corresponds to the three phases of the welding process described in Chapter 3.1. By increasing the US power only maximum slope value is increased and the shape of the slope distribution becomes sharper.

The mean values of the uncorrected pull test results is shown in Figure 3.21 in dependence of the US power. The pull tests are performed destructively and the actual pull test result is the force measured in the moment of the wire break. Again the error bars indicate the standard deviation of the pull test forces and the blue triangles mark the maximum and minimum value. The graph shows that high setup values of the US power do not result in higher pull test forces. Instead there is a maximum at a US power of about 65 digits, followed by a steady decrease of the pull test value.

Figure 3.22 shows the uncorrected pull test result plotted against the deformation. Furthermore the failure mode is indicated by colored markers. The maximum pull test force is

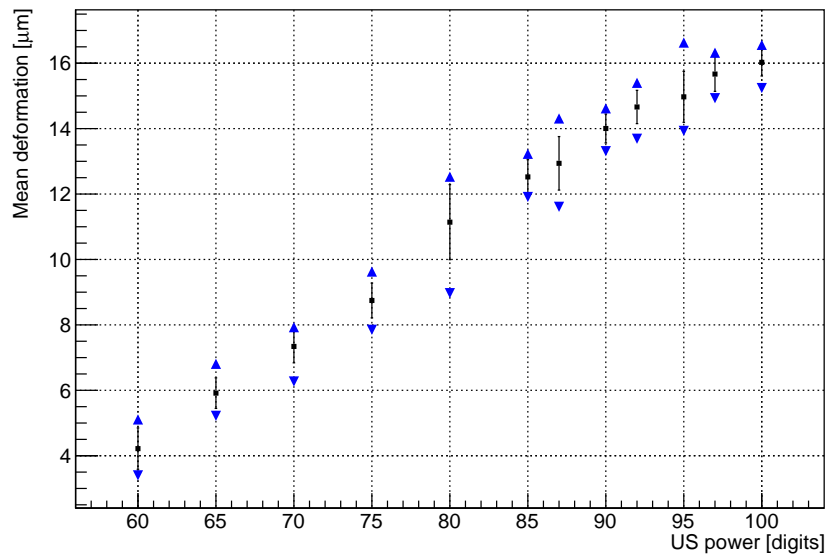


Figure 3.19: Mean values of the wire deformation plotted against the setup value of the US power. The blue triangles indicate the maximum and minimum values. The displayed error is the standard deviation of the deformation distribution of a single setup value.

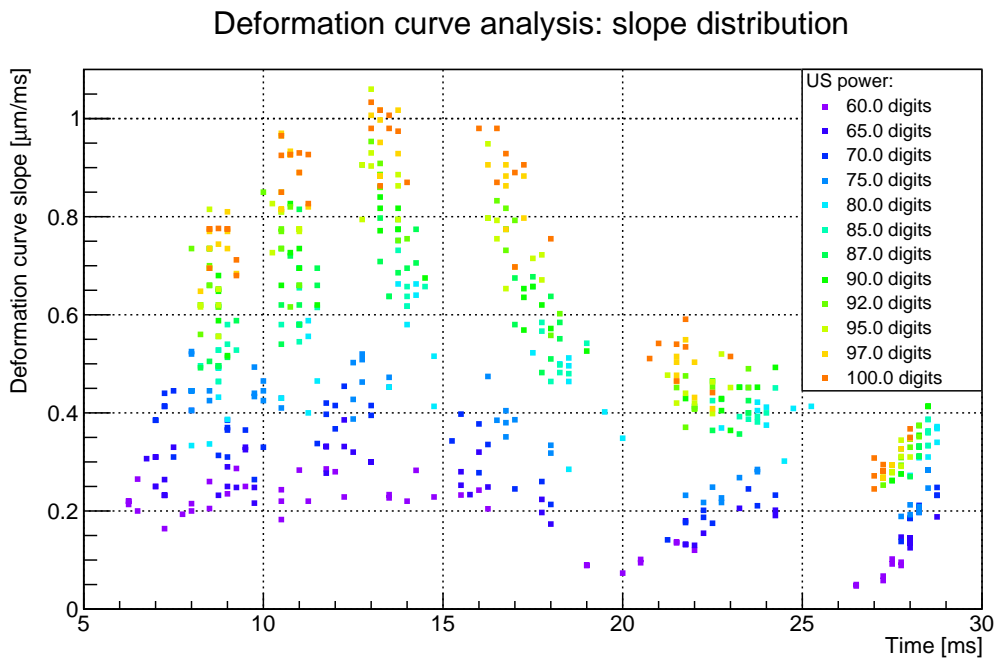


Figure 3.20: Deformation slope development for variation of the US power. The different US power settings can be distinguished by differently colored markers as specified in the legend.

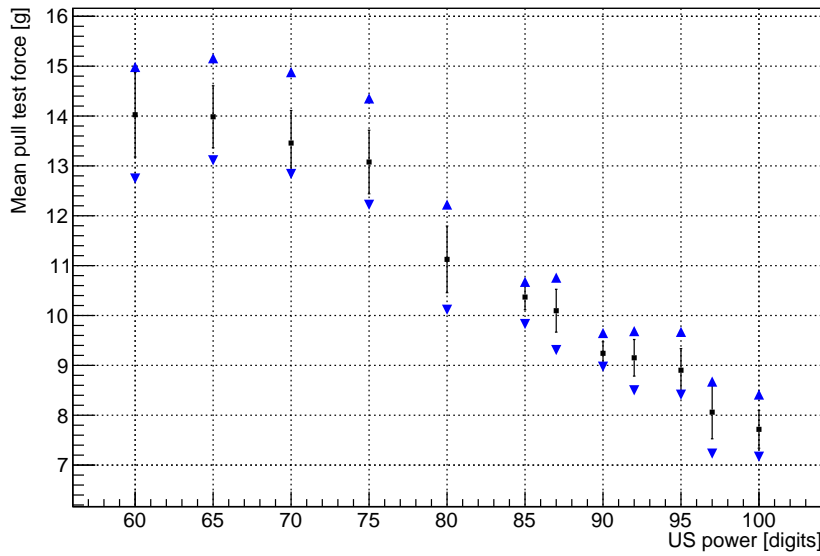


Figure 3.21: Uncorrected pull test results in dependence of the US power setup value. The blue triangles indicate the maximum and minimum values. The displayed error is the standard deviation of the pull test result distribution of a single setup value.

achieved with a vertical deformation of about  $5\ \mu\text{m}$ . For deformation values lower than  $5\ \mu\text{m}$  mainly lift-offs are detected. For higher deformations than  $6\ \mu\text{m}$  the failure mode is always heel break. Since lift-offs should be avoided (Table 3.1 on page 16), the preferred region of deformation and US power is not the region of maximum pull test results but a region with highest possible pull test results and low risk of lift-offs. A preferred vertical deformation could be about  $8\ \mu\text{m}$ . Comparing with Figure 3.19 on page 33, a deformation of  $8\ \mu\text{m}$  can be achieved with a US power setup of approximately 73 digits under the assumption that the remaining parameters are kept at the default values.

### Variation in bond force

Analogously to the studies of the US power the bond force is varied and analyzed. The BF is varied in a range from 20 to 42 cN while the US power is set to the default value of 85 digits. Figure 3.23 shows the machine measured deformation value in dependence of the applied BF. The deformation achieved with this parameter range is higher than the wire deformation values measured for the chosen variation of the US power. Therefore the saturation effect is clearly visible. For lower values of BF than 25 cN the relative variance of the wire deformation is much higher compared to those achieved with a set up BF higher than 25 cN. This might indicate that the force is too low or that the chosen default set of parameters does not fit well to low values of BF.

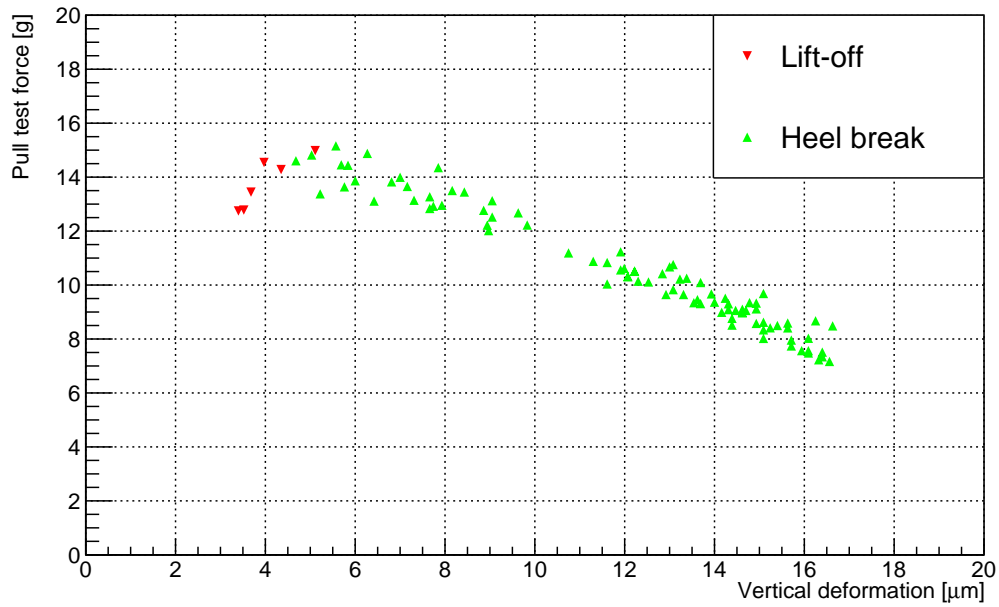


Figure 3.22: Uncorrected pull test results in dependence of the machine measured deformation. The variation of deformation is achieved by a variation of the US power. The failure mode is indicated by green (heel break) and red (lift-off) colored markers.

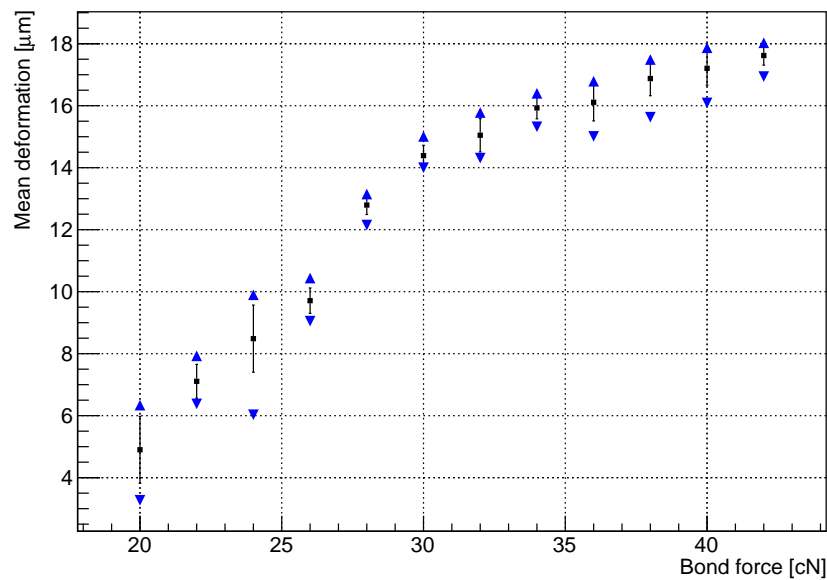


Figure 3.23: Mean values of the wire deformation plotted against the setup value of the BF. The blue triangles indicate the maximum and minimum values. The displayed error is the standard deviation of the deformation distribution of a single setup value.

The deformation slope development is displayed in Figure 3.24. The detected deformation slope ranges from about  $0.1 \mu\text{m ms}^{-1}$  to  $1.3 \mu\text{m ms}^{-1}$  which is slightly wider than in the variation of US power. The highest deformation slope is reached after 15 ms for every setup value of BF which is the same time value as in the variation of the US power. The plot shows an interesting feature for the last five milliseconds. The small peak indicates that for a high BF the deformation is done fast until no further deformation is possible and the slope decreases. If BF is relatively low, higher deformation slopes can be maintained until the end of the bonding process. The deformation does not yet run into saturation.

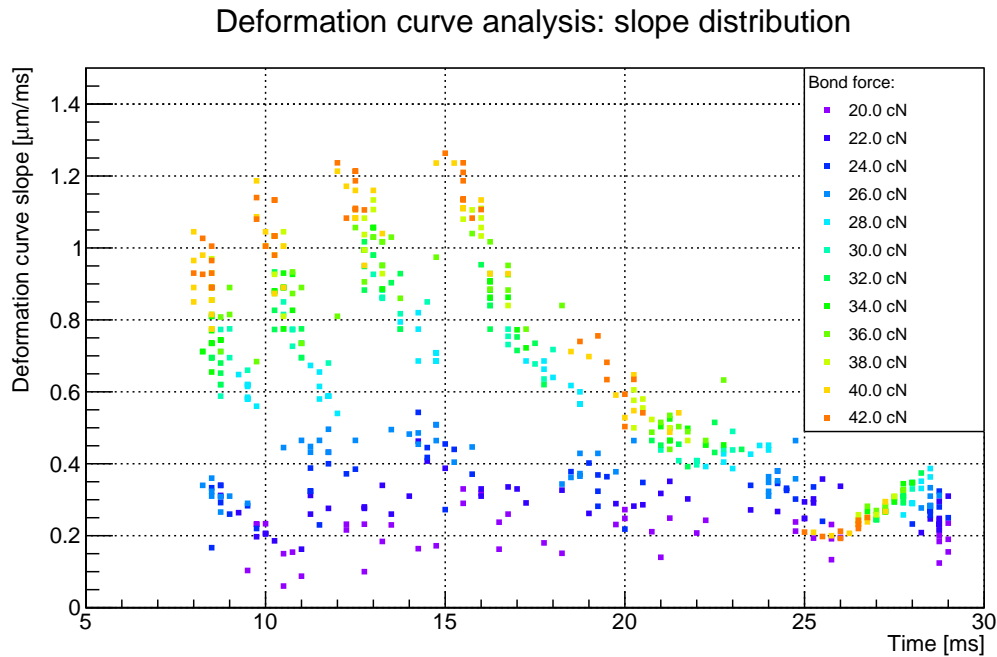


Figure 3.24: Deformation slope development for variation of the BF. The different BF settings can be distinguished by differently colored markers as specified in the legend.

The uncorrected pull test results are shown in Figure 3.26 in dependence of BF. The pull test result is decreasing over the whole tested range. A maximum value is expected to lie in the region of even lower values of BF.

Figure 3.26 presents the uncorrected pull test result including the information of the failure mode. Although the minimum deformation values are similar compared to those from the US power variation study, no lift-offs are detected over the whole range of BF setup values. The reason for this discrepancy might be a fluctuation because there is not much statistics in the relevant region of deformation. Another reason might be that the US power is a more critical parameter in terms of bond quality, which seems plausible as it is the most important parameter in all three phases of the welding process (Chapter 3.1 on page 11).

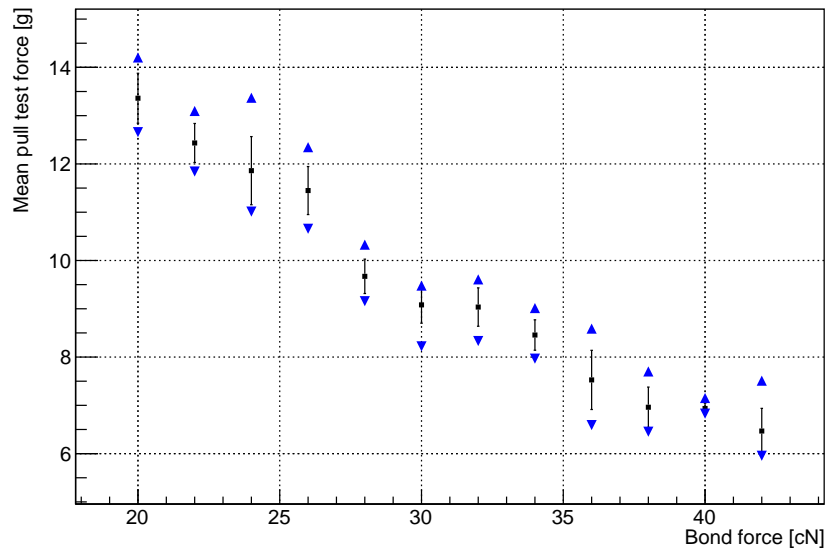


Figure 3.25: Uncorrected pull test results in dependence of the BF setup value. The blue triangles indicate the maximum and minimum values. The displayed error is the standard deviation of the pull test result distribution of a single setup value.

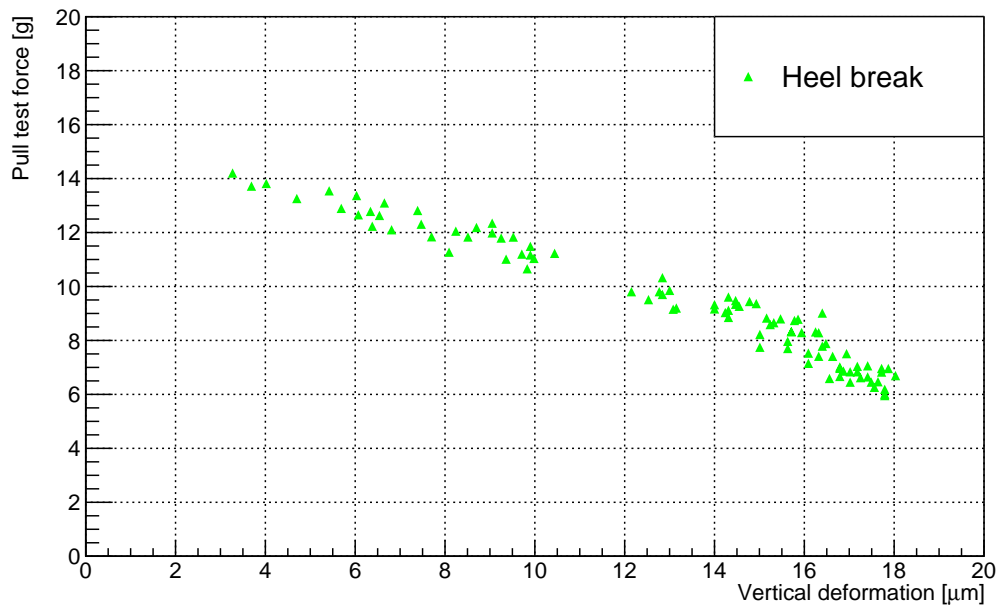


Figure 3.26: Uncorrected pull test results in dependence of the machine measured deformation. The variation of deformation is achieved by a variation of the BF.

## Variation in touchdown force

The impact of the touchdown force is tested over a range from 7 cN to 60 cN. It is important to keep in mind that the TDF is responsible for the pre-deformation, which is not part of the machine measured deformation<sup>8</sup>. The effect of the TDF on the machine measured deformation is shown in Figure 3.27. For low values of TDF up to 15 cN the deformation is rising with increasing TDF. Additionally the variance of the deformation measurements is much higher than deformation achieved with setup values higher than 15 cN. In the range between 20 cN to about 50 cN the deformation is almost constant. For higher setup values of TDF the measured deformation again drops and seems to become unstable. These results can be interpreted such that the pre-deformation is too low for TDF lower than 20 cN and too high for TDF higher than 50 cN. A low pre-deformation might lead to a smaller contact area between the wire and the bond surface. If the pre-deformation is too high, the wire might lose the flexibility to further deform during the welding process.

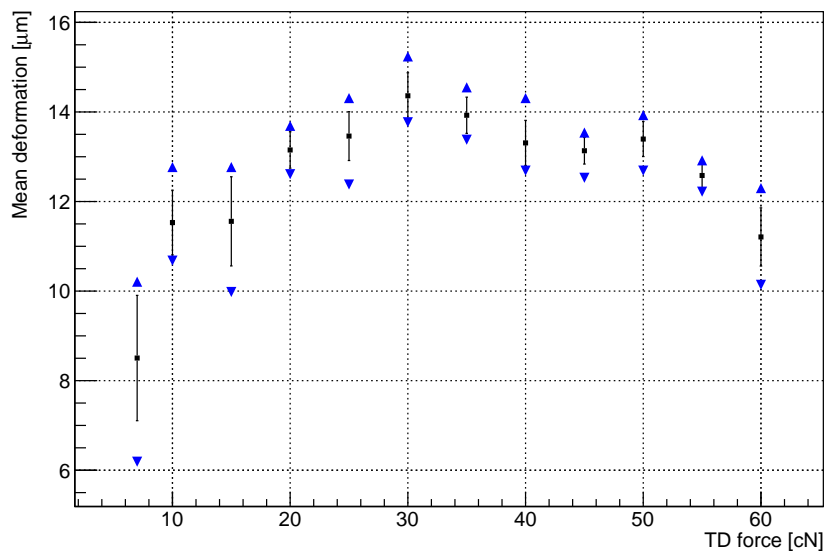


Figure 3.27: Mean values of the wire deformation plotted against the setup value of the TDF. The blue triangles indicate the maximum and minimum values. The displayed error is the standard deviation of the deformation distribution of a single setup value.

Figure 3.28 shows the development of the deformation slope. Compared to the recently discussed slope development plots (Figure 3.20 and 3.24), the shape is remarkably disordered. But if only the range from 20 cN to 50 cN is considered the shape is comparable with the recently shown ones.

The uncorrected pull test results of this test series are shown in Figure 3.29. The large uncertainty for a TDF of 7 cN corresponds to a single bond of which the bond has had a

<sup>8</sup>This is a personal interpretation of the information provided in the machine manual [22].

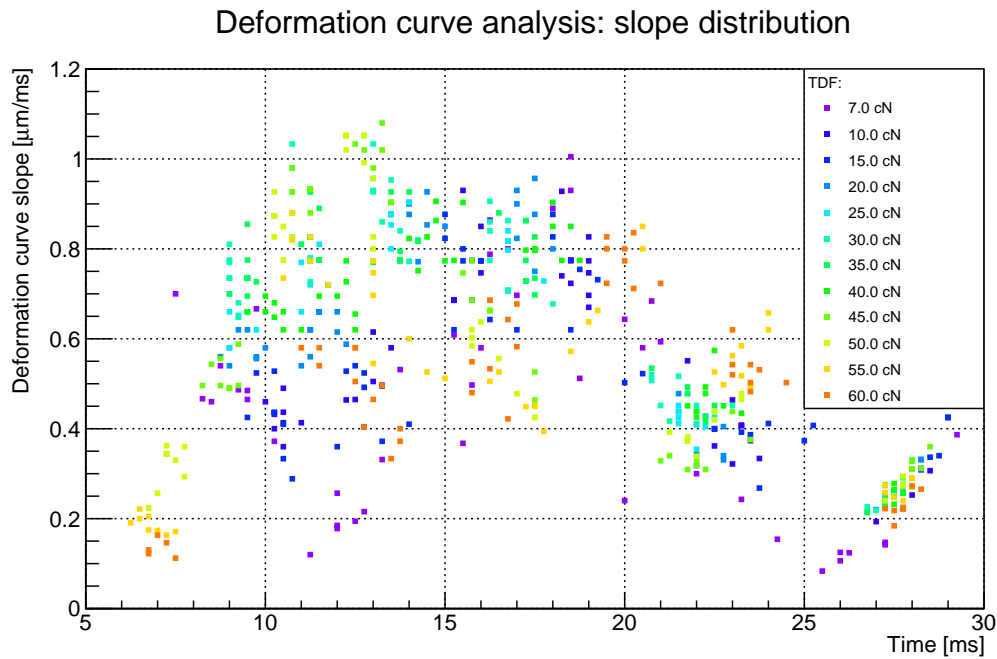


Figure 3.28: Deformation slope development for variation of the TDF. The different TDF settings can be distinguished by differently colored markers as specified in the legend.

lift-off without applying a measurable force. In this case the pull test result was set to 0 g. Aside from this setup value, the pull test result is almost constant over the whole test range, with a slight decrease of the pull test result with rising TDF.

Figure 3.30 displays the pull test result dependence of the wire deformation. Although a wide range of TDF has been tested, the wire deformation and the pull test results only cover a small area. So the TDF is a parameter which should be setup in the correct range (here between 20 and 50 cN) but the parameter range which can be used is broad compared to the US power or the bond force.

### Variation in bond time

As a last parameter the bond time is analyzed over a range from 5 to 60 ms. Figure 3.31 shows the wire deformation resulting from different setup values for BT. The deformation curve again is quite similar to what is measured in the variation of the US power and the bond force. The wire deformation rises until a saturation effect sets in.

The slope development for the variation of BT is shown in Figure 3.32. The plot shows that the deformation slope is the same for all setup values of BT. However, if a small BT is set up, the welding process may not go through all three phases. This may result in a worse quality of the wire bond.

The uncorrected pull test results are shown in Figure 3.33. It shows that for a BT value of 5 ms there is a large variance in the pull test results. The graph reaches its maximum at

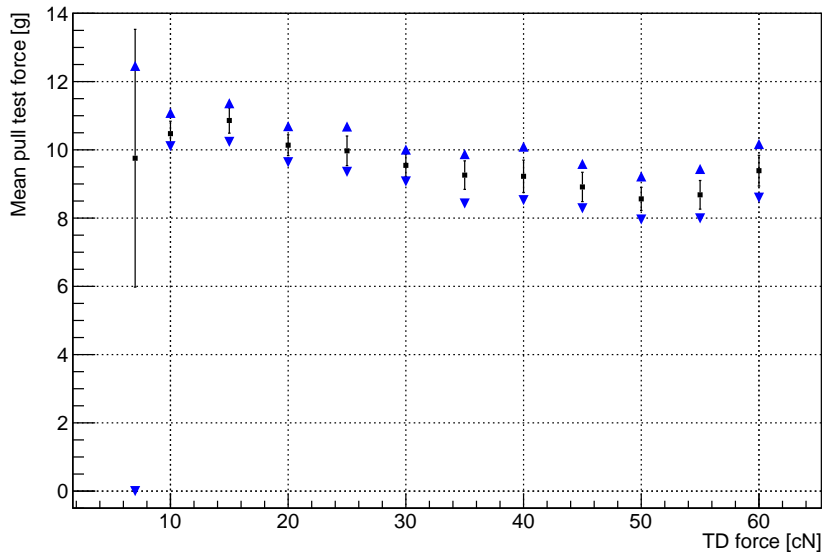


Figure 3.29: Uncorrected pull test results in dependence of the TDF setup value. The blue triangles indicate the maximum and minimum values. The displayed error is the standard deviation of the pull test result distribution of a single setup value.

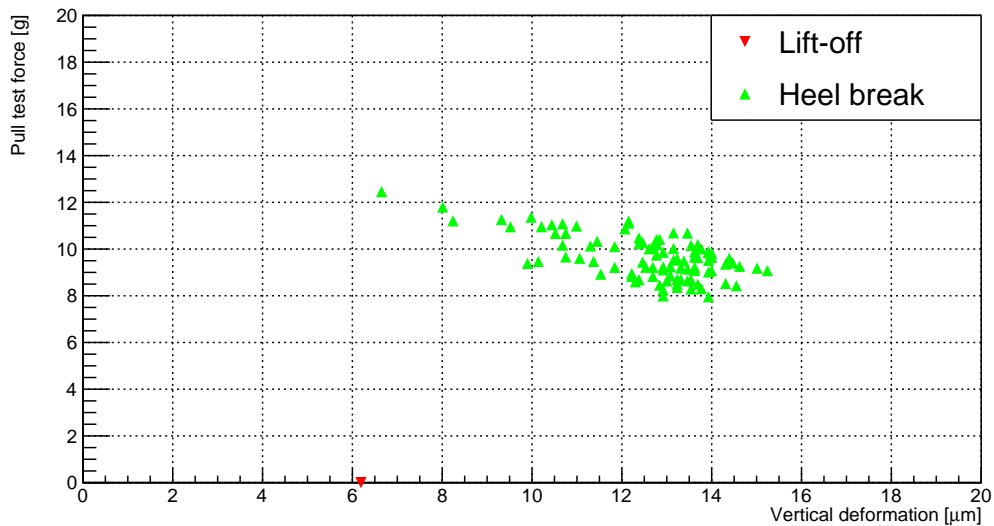


Figure 3.30: Uncorrected pull test results in dependence of the machine measured deformation. The variation of deformation is achieved by a variation of the TDF. The failure mode is indicated by green (heel break) and red (lift-off) colored markers.

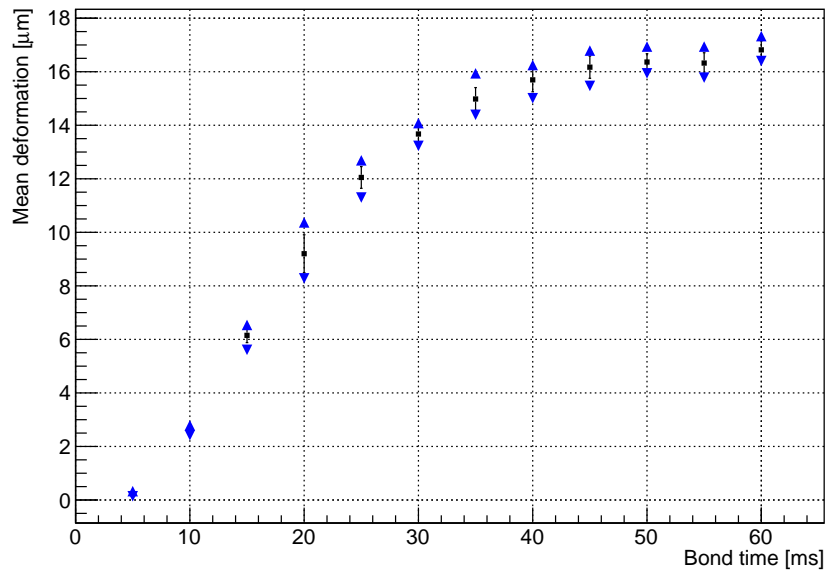


Figure 3.31: Mean values of the wire deformation plotted against the setup value of BT. The blue triangles indicate the maximum and minimum values. The displayed error is the standard deviation of the deformation distribution of a single setup value.

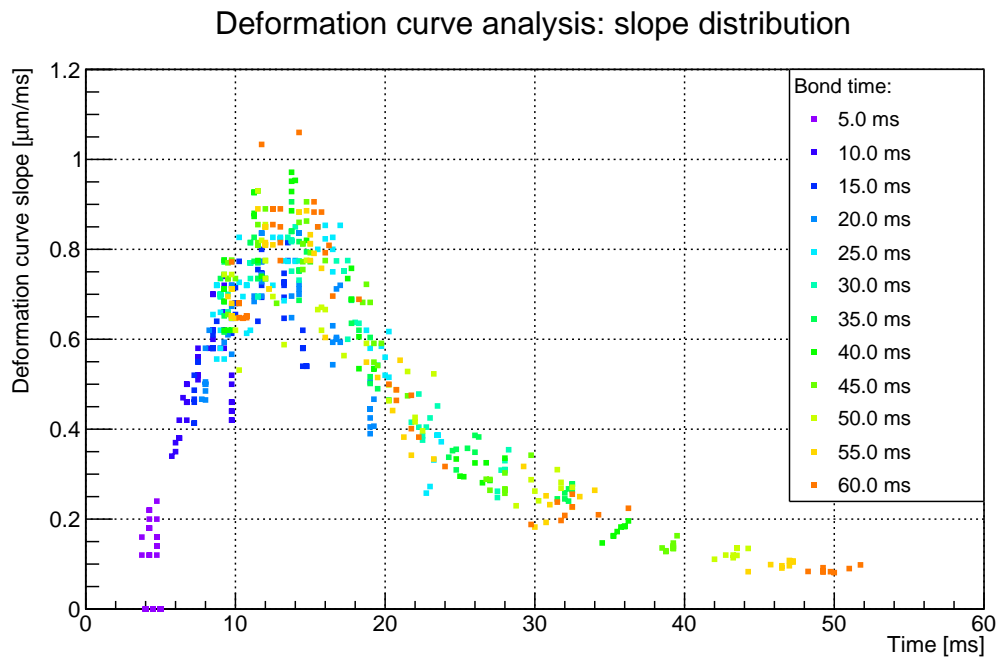


Figure 3.32: Deformation slope development for variation of BT. The different BT settings can be distinguished by differently colored markers as specified in the legend.

10 ms and decreases linearly up to a setup value of 40 ms. For even higher values of BT the decrease of the pull test result is softened but the variance is increased.

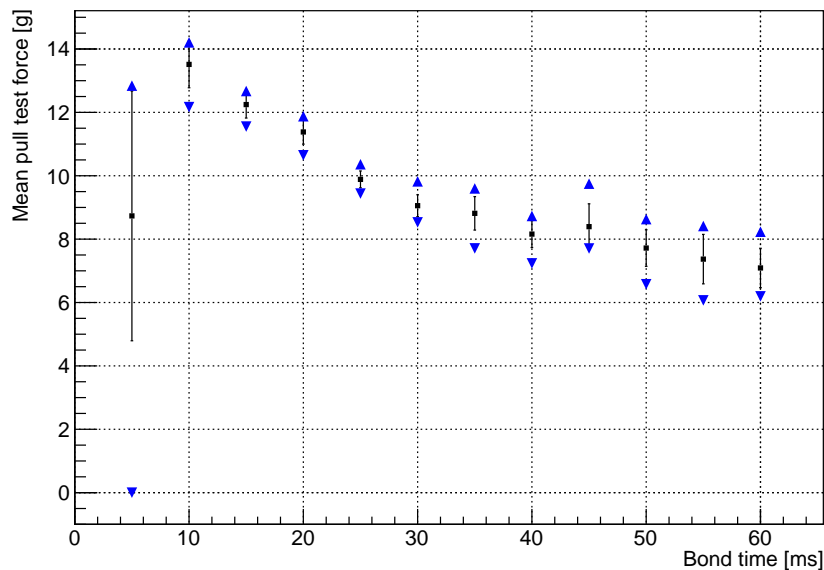


Figure 3.33: Uncorrected pull test results in dependence of the BT setup value. The blue triangles indicate the maximum and minimum values. The displayed error is the standard deviation of the pull test result distribution of a single setup value.

As shown in Figure 3.34, up to a deformation of  $3\ \mu\text{m}$  lift-offs are regularly detected. A preferred BT value could be 20 ms, which would result in a deformation of about  $9\ \mu\text{m}$ . This would ensure that on the one side lift-offs can be avoided, while on the other side all three phases of the welding process should take place.

## Conclusion

The discussed studies of the four most relevant bond parameters can be used to define an optimization method for the bonding process. The deformation slope plots of all four test series have shown a similar structure which represents the three phases of the welding process. The structure (with the maximum deformation slope after about 15 ms) itself seems to depend on the bond material properties. The bond time should be chosen high enough so that all three phases are passed. So high values of the bond time are definitely preferred. The US power should be chosen in a way that lift-offs are avoided but the pull test forces are as high as possible. The same applies to the bond force. When those two parameters are compared, the US power seems to be the more critical one, as in the studies lift-offs appeared much earlier. The touchdown force is the only parameter of those which has almost no impact on the pull test force. However, it is the parameter responsible for the pre-deformation. If the pre-deformation is too low or too high this affects the machine measured deformation.



## Variation of the BPC-slope

The slope parameter can be set in a range of  $10^\circ$  to  $89^\circ$ . The unit “degree” is not intuitive and there is only little information about this setup value provided. Figure 3.35 shows an exemplary deformation curve (red) and lines representing different slope setup values (black dotted). It is important to note that the axes have BT and the target deformation as units, so this plot represents the slope setup for all setup values of BT and target deformation. It is obvious that if the target deformation is set up with a small tolerance, with small values for the BPC slope setup the target deformation might not be reached within this tolerances because the machine stops as the BT is exceeded. This also means that a high slope setup might cause problems if the minimum bond time is high, because then the machine will work until the minimum bond time is exceeded and probably the maximum value of wire deformation has already been reached.

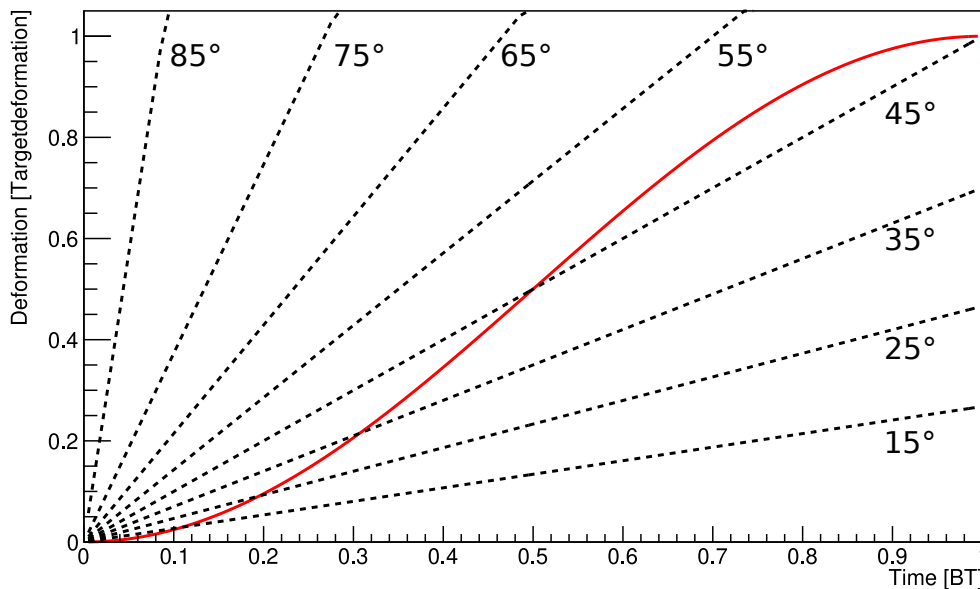


Figure 3.35: Sketch presenting the different slope setup values. The red graph shows an artificial wire deformation curve. The black dotted lines present the slopes generated with the setup values. Note that the axes are plotted in units of bond time and target deformation.

Nevertheless, the BPC slope setup value is tested in a wide range from  $25^\circ$  up to  $80^\circ$  with the recently used set of default parameters listed in Table 3.6 (page 32). This set of parameters has been used to achieve good comparability. The additional BPC parameters are summarized in Table 3.7. They are chosen in a way that the machine can adjust the US power in a wide range and stop the bonding process over a long time to avoid the problems discussed above as much as possible.

US power [digits]		Minimum BT [ms]	Wire deformation [ $\mu\text{m}$ ]		
Minimum	Maximum		Minimum	Target	Maximum
55	115	10	8	9	10

Table 3.7: Set of BPC parameters.

The mean deformation values are plotted against the BPC slope value in Figure 3.36. For a BPC slope smaller than  $45^\circ$  it is clearly visible that the target deformation is mostly not reached. Also the deformation has a big variance. For a BPC slope equal or higher than  $45^\circ$  the variance of the machine measured deformation values is extremely small with standard deviations in the order of  $0.05\mu\text{m}$ . Furthermore, the wire deformation stays within the set tolerances although there is a slight increase with rising BPC slope.

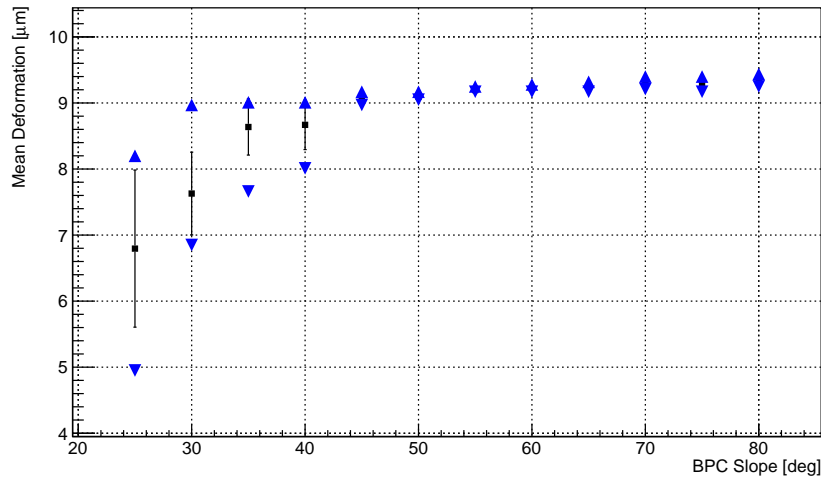


Figure 3.36: Mean values of the wire deformation plotted against the setup value of the BPC slope. The blue triangles indicate the maximum and minimum values. The displayed error is the standard deviation of the deformation distribution of a single setup value.

Analogously to the studies of Chapter 3.4.2, the deformation slope is measured and plotted for the different BPC slope setup values. Figure 3.37 displays the measured deformation slope data for the different setup values. Indeed the measured deformation slope is increasing approximately linearly with the corresponding setup value. If the plot is compared with the one from the US power variation test series, this one seems to be less broad in shape because the slope in the second phase of the welding process (at half of the bonding time) is much higher. This is because the initial US power is the setup value regardless of which slope is set. The BPC then analyzes whether this fits to the setup slope and adjusts it.

The uncorrected pull test results are shown in Figure 3.38. The measured pull tests decrease with rising BPC slope. An explanation for this is that the initial US power has been too high and low BPC slopes make the machine lower the US power. Additionally all three phases

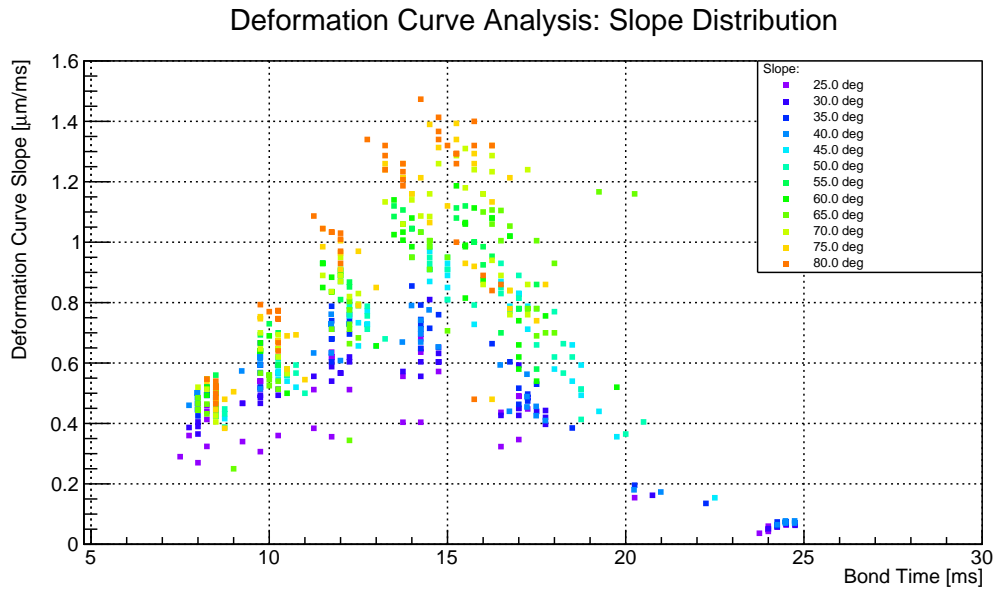


Figure 3.37: Deformation slope development for variation of BT. The different slope settings can be distinguished by differently colored markers as specified in the legend.

of the welding process have been passed because at low BPC slopes the actual bond time is higher.

An interesting characteristic appears in the plot of the uncorrected pull test results against the deformation shown in Figure 3.39. The corresponding plots with deactivated BPC (Figures 3.22, 3.26, 3.30 and 3.34) show that the data points lie on a smooth curve. However, there is a clearly visible kink at the target deformation. There are two possible reasons for this:

1. The BPC prevents the deformation from strongly exceeding the target deformation by immediately stopping the machine. But if the actual bond time is too short and the US power is too high compared to an ideal case, the quality in terms of pull test results decreases even though the deformation is almost stable.
2. The machine measured deformation is wrong if the deformation exceeds the setup target deformation.

The second hypotheses is tested in the following by studying the consistency of deformation measurements.

### Consistency of deformation measurements

The machine measured wire deformation is measured as vertical movement of the bond wedge after the touchdown during the bonding process. As the wire has a diameter (WD) of 25 µm this vertical deformation is of the order 10 µm. Optical measurements of this parameter are

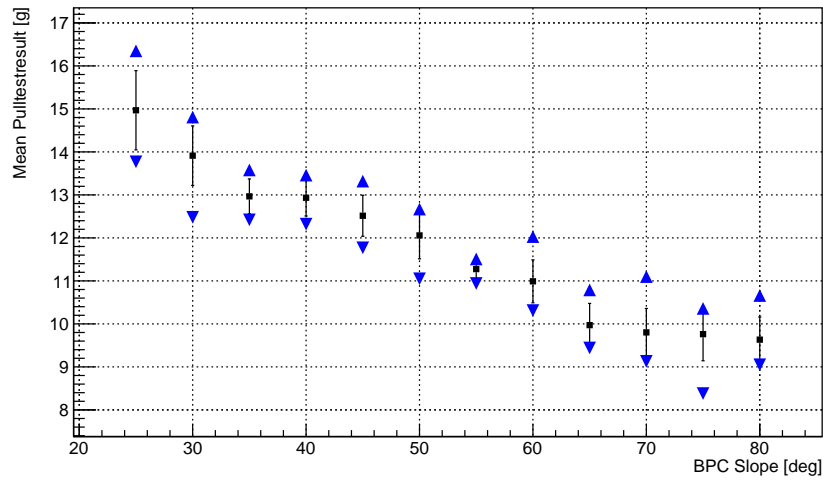


Figure 3.38: Uncorrected pull test results in dependence of the BPC slope setup value. The blue triangles indicate the maximum and minimum values. The displayed error is the standard deviation of the pull test result distribution of a single setup value.

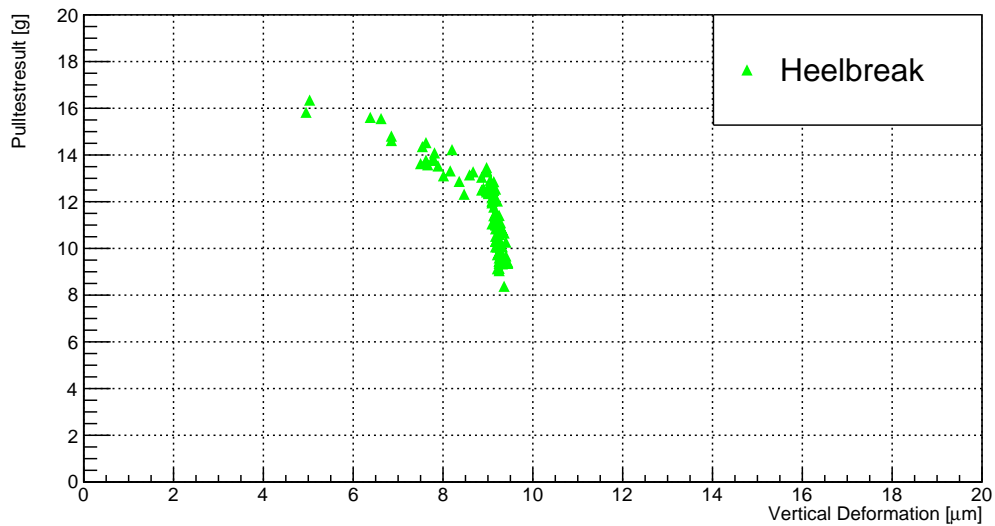


Figure 3.39: Uncorrected pull test results in dependence of the machine measured deformation. The variation of deformation is achieved by a variation of the BPC slope. The failure mode of all tested wires is heel break.

very challenging. Therefore, instead of a vertical deformation, the extrusion of the wire is measured as horizontal deformation. This is illustrated in Figure 3.40 (also Figure 3.7 on page 20). The horizontal deformation  $x = B - \text{WD}$  can approximately be calculated from the vertical deformation  $y = \text{WD} - h$  by assuming that the cylindrical shaped wire is pressed in a form of a cylinder with elliptical base:

$$L \cdot \pi \cdot \left(\frac{\text{WD}}{2}\right)^2 \approx h \cdot \frac{L}{2} \cdot \frac{B}{2} \cdot \pi \quad ,$$

$$\Leftrightarrow \quad h \approx \frac{\text{WD}^2}{B} \quad .$$

In doing so, the transition area is not included. It will be added as a correction constant  $C_{\text{corr}}$ . The horizontal deformation  $x$  and the vertical deformation  $y$  are then set in:

$$\text{WD} - y \approx \frac{\text{WD}^2}{x + \text{WD}} \quad ,$$

$$\Leftrightarrow \quad x \approx \frac{\text{WD} \cdot y}{\text{WD} - y} \quad ,$$

$$\Rightarrow \quad x \approx \frac{\text{WD} \cdot y}{\text{WD} - y} + C_{\text{corr}} \quad . \quad (3.11)$$

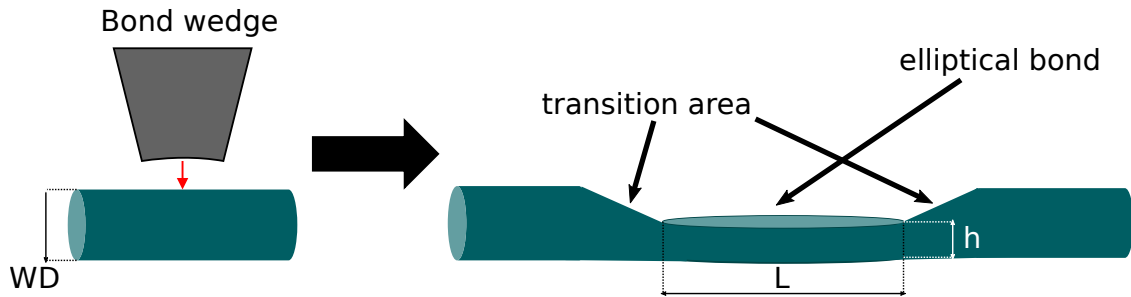


Figure 3.40: Visualization of the wire deformation to describe the mathematical model.

The horizontal deformation is measured with a self-made picture analysis program based on the *OpenCV* library [31] which recognizes contours and fits ellipses at the bonds. The horizontal deformation is extracted from the bond width, which is one of the fitted ellipse parameters.

The derived mathematical model of the wire deformation is tested on a test series with activated BPC and deactivated BPC. The deformation is changed by varying the bond force. For each setup value of BF the horizontal deformation and the vertical deformation are averaged. The standard deviation is used as error. Figure 3.41 shows the dependence of the horizontal deformation from the vertical deformation in the case of deactivated BPC.

The model (Equation 3.11) fits well to the data. However, the fit value of the wire diameter is not reproduced correctly. The reason might be that the model is a coarse approximation. The fit values of wire diameter (WD) and  $C_{\text{corr}}$  are at least in the correct order of magnitude.

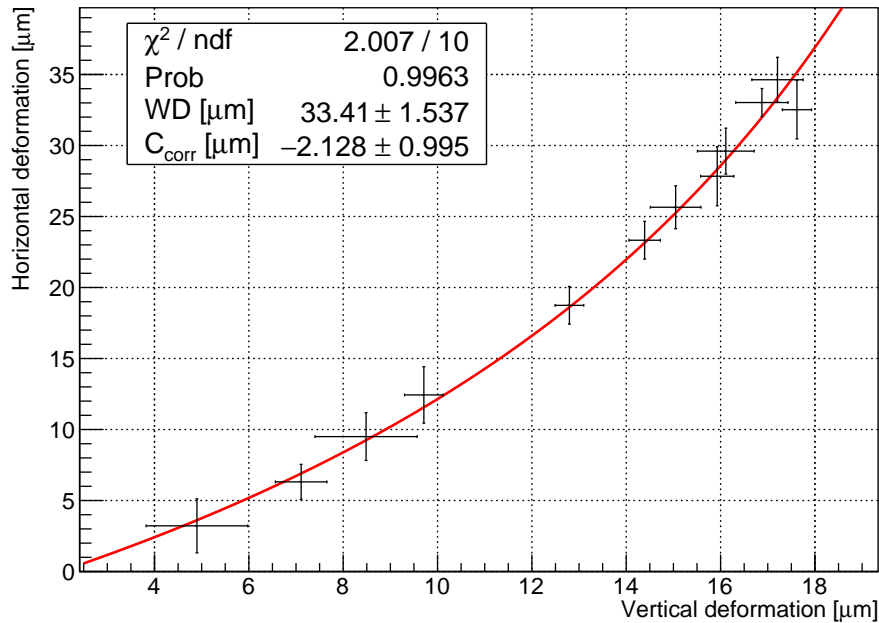


Figure 3.41: The mean horizontal deformation is plotted against the mean vertical deformation with the standard deviation as error. The deformation is changed by a variation in BF with *deactivated* BPC.

The model fit in case of an activated BPC is shown in Figure 3.42. It is clearly visible that the model fit does not provide physically reasonable results. The change in the horizontal deformation is smaller than in case of a deactivated BPC. This is an expected behavior as the machine adjusts the US power to achieve the target deformation. However, the change of the horizontal deformation is still significant compared to the vertical deformation, which is almost constant at the target deformation. This leads to the conclusion that the bonding machine does not measure the actual deformation of the wire correctly if the BPC is activated and the target deformation is reached.

### Comparison of wire bond quality with and without BPC

The effect of the BPC on the bond quality is tested by varying the BF with activated and deactivated BPC. The BPC slope setup value has been set to  $60^\circ$ . Figure 3.43 shows the distribution of uncorrected pull test results with activated BPC indicated in blue and the ones with deactivated BPC in red. The red graph has been discussed already in Chapter 3.4.2. It shows that pull test results are very sensitive to variations in BF if the BPC is deactivated. In contrast, if the BPC is activated, the pull test results are kept almost constant over the

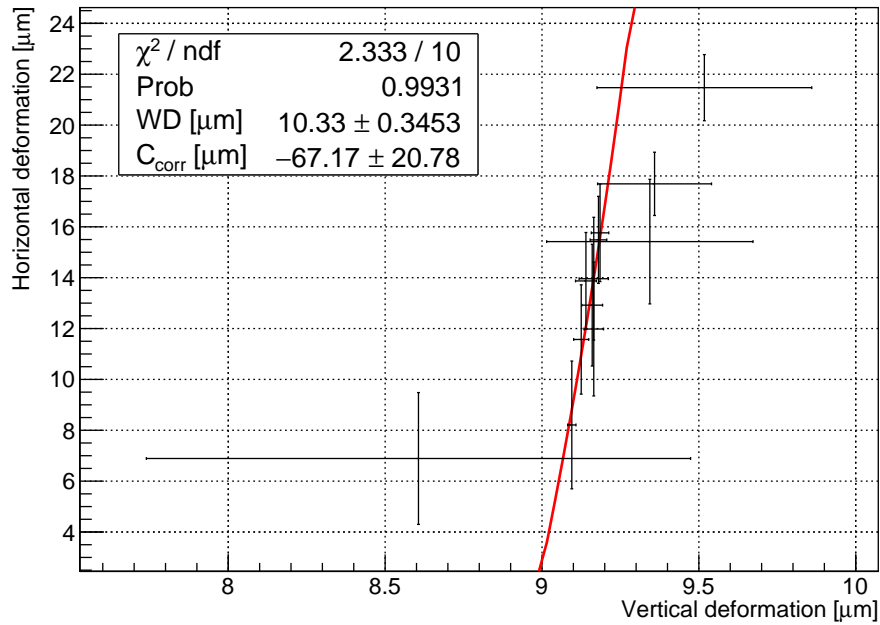


Figure 3.42: The mean horizontal deformation is plotted against the mean vertical deformation with the standard deviation as error. The deformation is changed by a variation in BF with *activated* BPC.

whole range of BF parameters. The machine effectively compensates for bad setups of the BF by adjusting the US power and regulating the actual bond time. This is an advantage as mistakes in parameter optimization and variations in surface quality might be balanced by the machine. The highest pull test results shown in this plot have been achieved with deactivated BPC. This is because the setup target deformation of 9 μm is not optimal.

## Conclusion

The presented studies show that the BPC provides features which can stabilize the bonding process and avoid errors. For this the BPC parameters have to be optimized as well as the other bond parameters. The BPC-slope is defined in a way that slopes below 45° mostly result in too low wire deformation values, which leads to an error stopping the machine. On the other side higher bond times should be preferred. Thus, BPC-slopes of the order 50° to 60° are reasonable setup values. The target deformation can be chosen during the optimization of the BF or US power as presented in Chapter 3.4.2. The machine measured deformation value has to be handled with caution as the values do not fit to the corresponding crosscheck values of horizontal deformation.

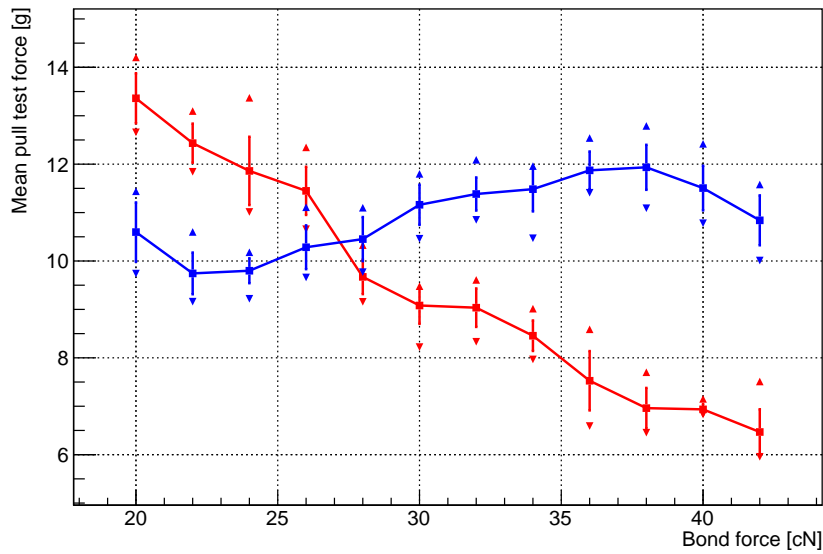


Figure 3.43: Comparison of the quality of bonds with activated (blue) and deactivated (red) BPC. The pull test results are uncorrected. The displayed error is the standard deviation. The triangles indicate maximum and minimum values.

## 3.5 Bond procedure in module series production

The bond parameter optimization methods presented in Chapter 3.4 are applied on one of the four sides of a 2S dummy module in this chapter. Furthermore module preparations relevant for the series production are discussed as well as the general bonding program. There are additionally special module bonding programs which provide extra wires for pull tests. They will be described and used to test the quality of the module wire bonds.

### 3.5.1 Description of the dummy module and its preparation

The dummy module consists of non-functional parts. The two sensors have bond pads only on one side. On the other side the strips are connected by a broad band of aluminum which can be used as bond surface. This appears on the left top side (Figure 3.44 (a)) and left bottom side (Figure 3.44 (b)) of the dummy module. The FE hybrids are not identical. One of the hybrids does not provide bond pads on the bottom side (on the right side of Figure 3.44 (b)).

The top left side has already been wire bonded during the bond machine acceptance. The right top side has been used to optimize the bond parameters during the machine acceptance and is furthermore used for this purpose for the studies of this theses. The actual module wire bonding as part of this theses is performed on the left bottom side because it is the only remaining side, as wire bonding is not possible on the right bottom side. Table 3.8 summarizes the status and usage of the different bond regions of the dummy module.



Figure 3.44: Photographs of the 2S dummy module.

Side	Bond pads on sensor	Bond pads on hybrid	Used for ...
Left top	X	✓	... bond machine acceptance
Right top	✓	✓	... parameter optimization
Left bottom	X	✓	... <a href="#">module bonding</a>
Right bottom	✓	X	Wire bonding not possible

Table 3.8: Summary of the status and usage of the bond regions of the dummy module.

The first step in the wire bonding process of the module production has to be the visual check of the bonding material. The bond pads on the FE hybrids and the sensors have to be clean and must not be scratched. The dummy module has been used for other tests before and therefore it has several scratches and contamination. Thus, it was cleaned carefully with cotton buds and clean room tissue using cleansing material for circuit boards.

The module positioning and alignment of the bonding jig is a very important step in the preparation of the bonding process. Especially the aluminum rods supporting the FE hybrids have to be vertically aligned with high precision. The alignment has to be done under vacuum because the whole module is pulled down by about one millimeter when the vacuum is activated. Figure 3.45 shows the view through the microscope onto a dentist mirror used to see the rod during the alignment. Several tries have shown that if the rod is too low so that a gap between rod and hybrid is visible, the hybrid is badly supported. This can be tested by carefully pressing onto the surface with a soft and clean tool while watching the surface through the microscope. On the other hand if the rod is set too high, the sensor is badly supported as it lifts off from the surface.

The loop parameters are chosen in a way that the wire height is as low as possible. This is done to decrease the risk of touching and breaking the wires. The CERN bond lab suggests a total wire height of 300 to 400  $\mu\text{m}$ . This cannot be achieved with this dummy module because the Kapton foil, which electrically isolates the hybrid from the high voltage of the

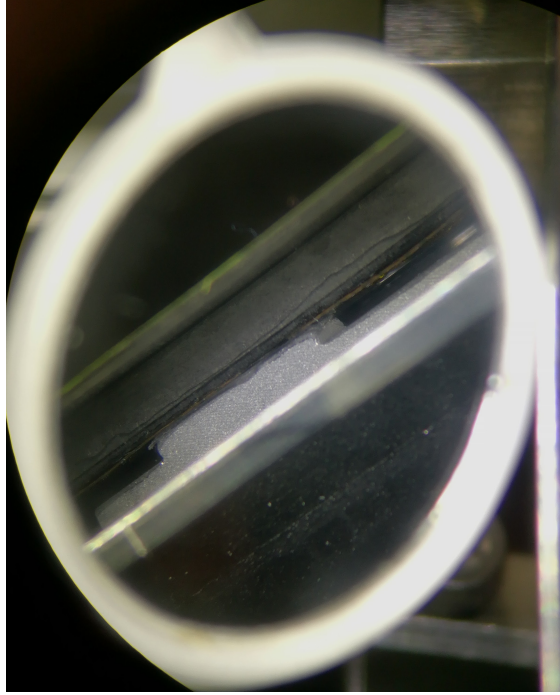


Figure 3.45: Photograph of the alignment of the hybrid support rod.

sensor, sticks out of the small gap between the hybrid and the sensor. The maximum height of the Kapton foil sets the minimum wire height. So the wire height has to be in the order of 400 to 600  $\mu\text{m}$ . The bond direction is chosen to be from hybrid to sensor. This enables to set up an asymmetric wire geometry to achieve a higher distance to the sensor edge with high voltage.

### 3.5.2 Determination of the correction factors and systematic uncertainties for parameter optimization

The systematic uncertainties and the correction factors are determined analogously to the procedure presented in Chapter 3.4. The bond material is not flat like the ENIG plates but there is a step between the hybrid and the sensor. The step is not the same for the top right side and the bottom left side. So the determination of the correction factor and systematic uncertainties has to be done separately for the two sides. To be able to optimize the bonds on both bond surfaces, the hybrid (source) and the sensor (destination), a second hook position region has to be considered to force the wire to break at the destination bond which is necessary to gain the information about the quality of the destination bond on the sensor.

Figure 3.46 shows the calculated correction factors  $K_1$  and  $K_2$  using the Delvotec formula and the simple formula, each with an elongation of 1% and 4%. The estimated hook positions for the optimization of the source and destination bonds are indicated in green.

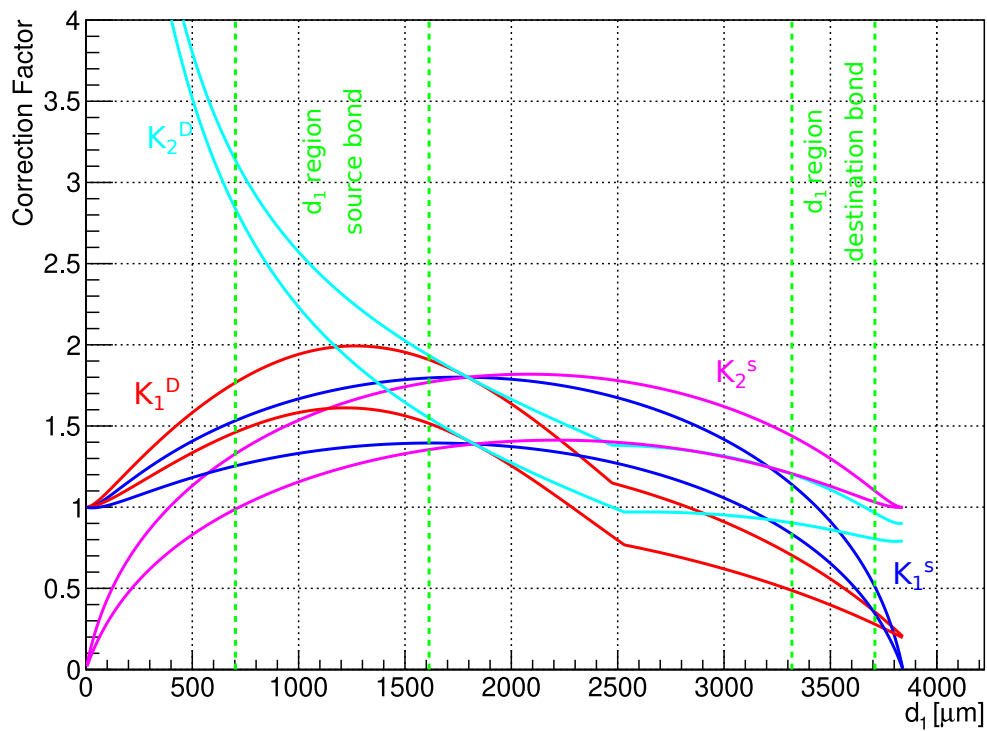


Figure 3.46: Calculated correction factors  $K_1^D$  (red),  $K_2^D$  (turquoise),  $K_1^S$  (blue) and  $K_2^S$  (pink) plotted against the position of the pull test hook.

First the correction factors with the hook position region for the optimization of the source bond are discussed. However, the correction factors  $K_1$  and  $K_2$  are calculated to be able to compare both. The mean correction factors are again determined by filling histograms with ten thousand randomly generated hook positions in the estimated region. The resulting values are summarized in Table 3.9. The discrepancy between the different values for  $K_1$  and  $K_2$  is huge. Based on these values the correction factor for the source bond lies within the limits  $1.35 \pm 0.04 \leq K_1 \leq 1.93 \pm 0.06$  and the correction factor of the destination bond is  $1.21 \pm 0.11 \leq K_2 \leq 2.42 \pm 0.34$ . It is remarkable that  $K_2$  is much bigger than  $K_1$  if the Delvotec formula is used, because almost every wire has broken at the source bond. Also, the correction factor  $K_2$  is naively expected to be small compared to  $K_1$  if the pull hook is positioned near the source bond. Using the Delvotec formula it  $K_2$  rises enormously when  $d_1$  is decreased. This indicates that the simple formula might be the better one.

Formula	Elongation	Correction factor $K_1$			Correction factor $K_2$		
		$\mu$	$\sigma$	$\sigma/\mu$	$\mu$	$\sigma$	$\sigma/\mu$
Delvotec	1 %	1.93	0.06	3 %	2.42	0.34	14 %
	4 %	1.57	0.04	3 %	2.06	0.36	17 %
Simple	1 %	1.70	0.08	5 %	1.60	0.13	8 %
	4 %	1.35	0.04	3 %	1.21	0.11	9 %

Table 3.9: Summary of means and RMS of the histograms of calculated correction factors for the optimization of the **source bond** on the top right side of the module. The parameter  $\mu$  is the mean correction factor and  $\sigma$  is the standard deviation.

The systematic uncertainty of single pull tests is estimated by considering the first 20 % of the  $d_1$  region of the source bond. This is the worst case as this is the part with highest slopes in the correction factors. The errors are determined by filling again ten thousand  $K_1$  with randomly generated  $d_1$  uniformly within this region. Only  $K_1$  is considered since almost all wires have broken at the source bond. The error is determined as relative standard deviation. The worst case appears with a relative systematic uncertainty of 4 ‰ applying the Delvotec formula with 1 % elongation. This uncertainty is totally suppressed by statistical uncertainties, so it can be neglected.

The values for the optimization region of the destination bond are shown in Table 3.10. The correction factor for the source bond is determined to be  $0.39 \pm 0.06 \leq K_1 \leq 0.87 \pm 0.18$ . The correction factor for the destination bond on the other side lies within the limits  $0.86 \pm 0.03 \leq K_2 \leq 1.28 \pm 0.10$ .

The systematic uncertainty of single pull tests for the optimization of the destination bond is determined analogously to the systematic uncertainty for the optimization of the source bond.  $K_2$  is considered instead of  $K_1$  because almost all wires have broken at the destination bond. The highest relative systematic uncertainty is 3 ‰ calculated by using the Delvotec formula

Formula	Elongation	Correction Factor $K_1$			Correction Factor $K_2$		
		$\mu$	$\sigma$	$\sigma/\mu$	$\mu$	$\sigma$	$\sigma/\mu$
Delvotec	1%	0.54	0.10	19%	1.09	0.07	6%
	4%	0.39	0.06	15%	0.86	0.03	3%
Simple	1%	0.87	0.18	21%	1.28	0.10	8%
	4%	0.62	0.14	23%	1.12	0.05	4%

Table 3.10: Summary of means and RMS of the histograms of calculated correction factors for the optimization of the **destination bond** on the top right side of the module.  $\mu$  is the mean correction factor and  $\sigma$  is the standard deviation.

with 4% elongation. The systematic uncertainty is completely suppressed by statistical errors. So the systematic uncertainty is neglected.

As the differences between the determined correction factors are huge, the plots in the following chapters still present uncorrected pull test forces but limits of the corrected values are discussed.

### 3.5.3 Optimization of the bond parameters

The optimization of the bond parameters is done on the top right side (Figure 3.44 (a)). Note that the optimal set of bond parameters might not be the same for the top right side and the left bottom side since the goodness of the support and the contamination level might vary.

The bond parameters of the source bond are optimized first. The first parameter which is studied is the US power because it is the most critical parameter in terms of bond quality. The US power is scanned in the range from 95 to 125 digits in steps of 5 digits. This range is not arbitrarily chosen but based on tests of single wires. Each setup value is applied on four wires. The bond time is set to 35 ms, the bond force and touchdown force are both set to 35 cN. The correct setup of the bond time is checked by studying the deformation slope development, shown in Figure 3.47. The tail of the slope development curve is included. So all three phases of the welding process can be passed and the setup value of BT is large enough.

Figure 3.48 shows the wire deformation and the uncorrected pull test results for the variation of the US power. The wire deformation rises with increasing US power with a visible saturation effect (Figure 3.48 (a)). However, the pull test results are almost stable for US power setup values higher than 100 digits (Figure 3.48 (b)). Up to this setup value lift-offs are detected, as shown in Figure 3.48 (c). So for this set of parameters the optimal setup value of US power is chosen to be in the region around 117 digits because the risk of lift-offs is low and the deformation and pull test results show little variances. The uncorrected pull

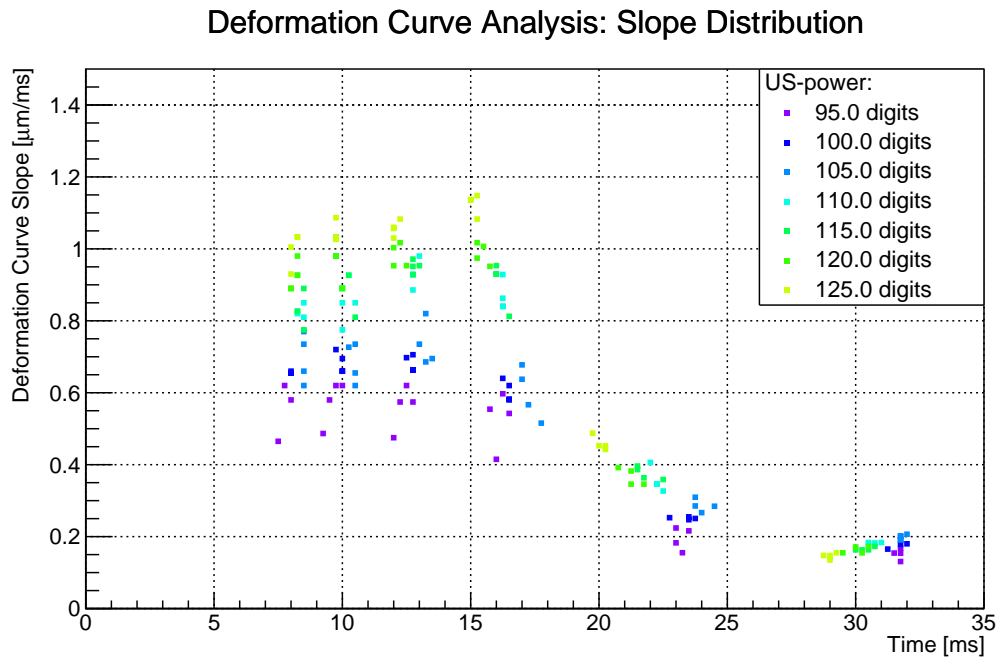
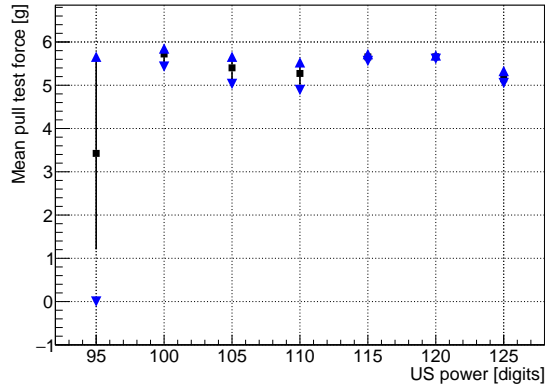
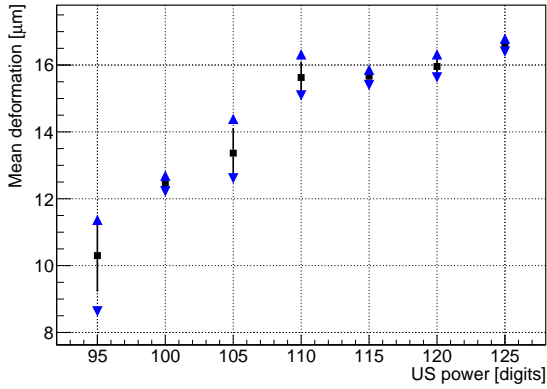


Figure 3.47: Deformation slope development of the source bond in the variation of the US power.

test results are about  $(5.7 \pm 0.1)$  g. The corresponding corrected pull test result lies between  $(7.7 \pm 0.3)$  g and  $(11.0 \pm 0.4)$  g. The errors are determined using Gaussian error propagation. In the next step the bond force and the touchdown force are optimized with  $BF = TDF$ . The studied parameters range from 24 to 40 cN with a step size of 2 cN. The wire deformation and the uncorrected pull test results are shown in Figure 3.49 (a) and 3.49 (b). The wire deformation shows the known behavior. At a setup force of 24 cN the wire deformation is very unstable. The pull test results on the other hand decrease with rising setup force. There are no lift-offs detected over the whole range. So the optimal force value is in the region of 28 cN, still providing high and stable pull test results. The uncorrected pull test result is  $(6.0 \pm 0.1)$  g for this set of parameters. This corresponds to corrected pull test results of  $(8.1 \pm 0.3)$  g in the worst case or  $(11.6 \pm 0.4)$  g in the best case.

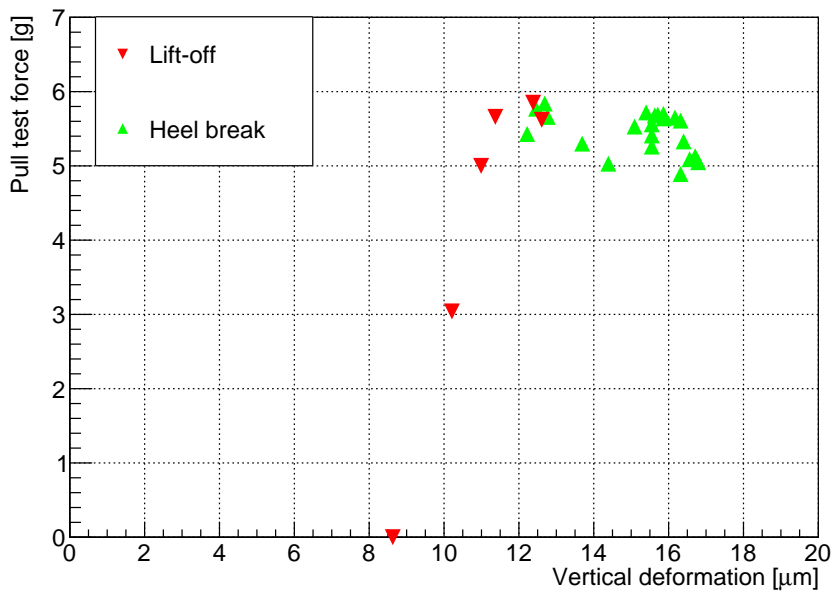
Both, the US power and the setup force, have been tested analogously a second time to further optimize or verify the determined setup values. After that, the US power is set to 110 digits and the bond / touchdown force is set to 28 cN. This set of parameters achieves mean uncorrected pull test results of  $(6.2 \pm 0.2)$  g. The corrected pull test result lies between  $(8.4 \pm 0.3)$  g and  $(12.0 \pm 0.5)$  g.

In the next step, the parameters of the destination bond are optimized. The bond time is checked by studying the deformation slope development shown in Figure 3.50 with variation in US power. The shown distribution is much broader and more flat than the corresponding distribution for the source bond. However, if the single data point at about 34 ms with a



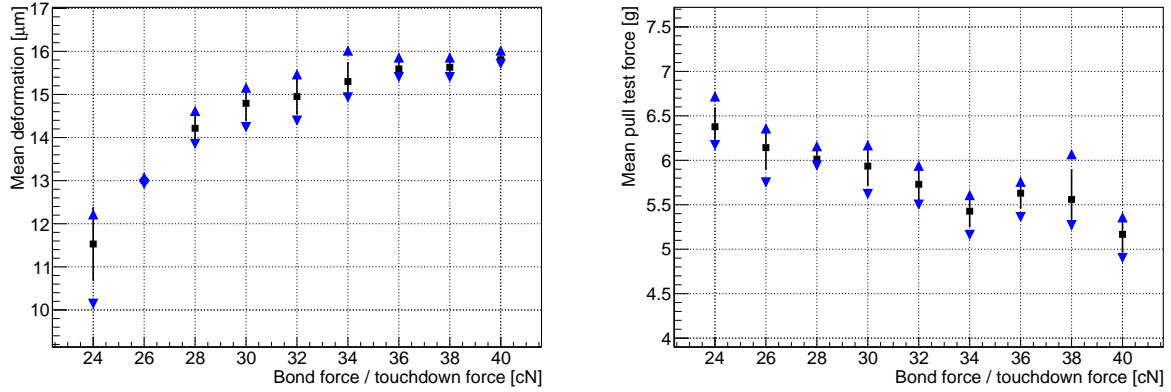
(a) Dependence of the deformation and the setup US power.

(b) Dependence of uncorrected pull test results and the setup US power.



(c) The machine measured deformation is plotted against the pull test result including the failure mode.

Figure 3.48: The plots (a) and (b) show mean values of deformation and uncorrected pull test result in variation of the US power for the source bond. The error is the standard deviation of the results. The blue triangles indicate the minimum and maximum values. Figure (c) combines both plots including the failure mode.



(a) Dependence of the deformation and the setup BF and TDF. (b) Dependence of uncorrected pull test results and the setup BF and TDF.

Figure 3.49: The plots (a) and (b) show mean values of deformation and uncorrected pull test results of the source bond for the variation of the setup BF and TDF. The error is the standard deviation of the results. The blue triangles indicate the minimum and maximum values.

slope of approximately  $0.56 \mu\text{m ms}^{-1}$  is treated as an outlier, for all setup values of the US power the slope is falling after 35 ms. So the setup value of BT should be high enough. The broad and flat distribution might indicate a problem in the bonding process, like for example a very fine scratch on the bond pads of the sensor. Such a scratch has been found after the wire bonding during visual inspections with a microscope.

The US power is studied over the range from 65 to 105 digits with a step size of 5 digits. The wire deformation and uncorrected pull test results are plotted against the different setup values of US power in Figure 3.51. The wire deformation increases almost linearly with increasing setup value of US power as expected (Figure 3.51 (a)). The bonds with US power in the range between 70 and 90 digits have very low variance in the measured wire deformation. The mean uncorrected pull test results are maximized in the same range (Figure 3.51 (b)). The smallest variances are achieved at about 85 digits. This value results in a wire deformation of about 11 to 12  $\mu\text{m}$ . As shown in Figure 3.51 (c) lift-offs are detected for wire deformations up to 10  $\mu\text{m}$ , corresponding to a US power setup value of 80 digits. So the optimal US power setup value is chosen at 90 digits, which has achieved good pull test results and prevents lift-offs.

The optimization study of the BF and TDF setup values is presented in Figure 3.52. Again the TDF is set to the same value like BF over the whole range from 22 to 38 cN with a step size of 2 cN. No lift-offs have been detected but the failure mode wire break appeared twice with the force parameters set to 22 cN. So, lift-offs are expected to appear for values lower than 22 cN. The pull test results slightly decrease with increasing force parameter with a non negligible drop at 34 cN (Figure 3.49 (b)). A force parameter of 27 cN is chosen in order to avoid

### Deformation curve analysis: slope distribution

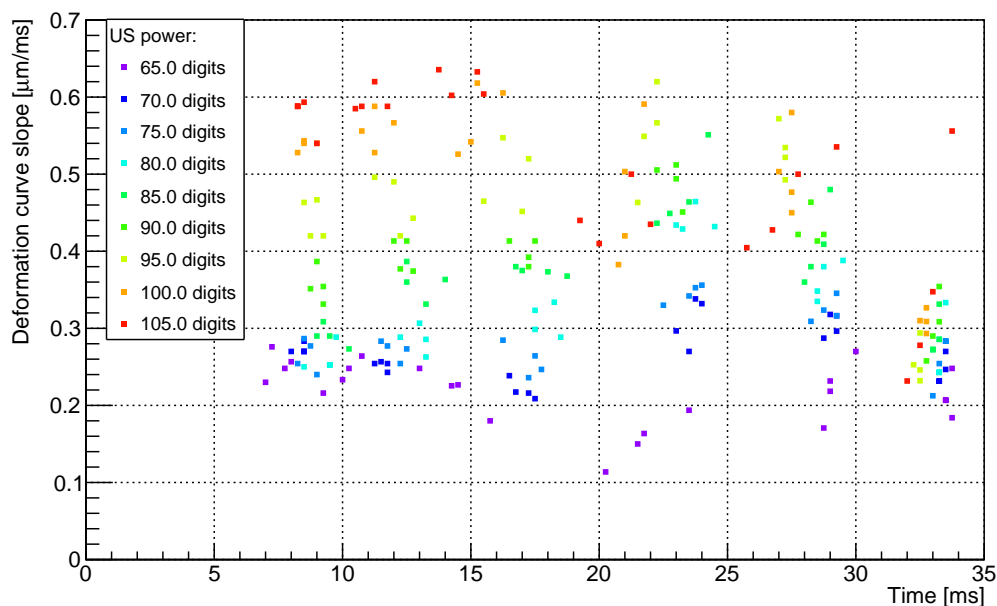
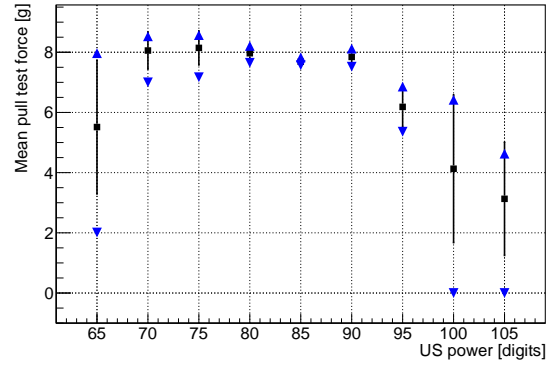
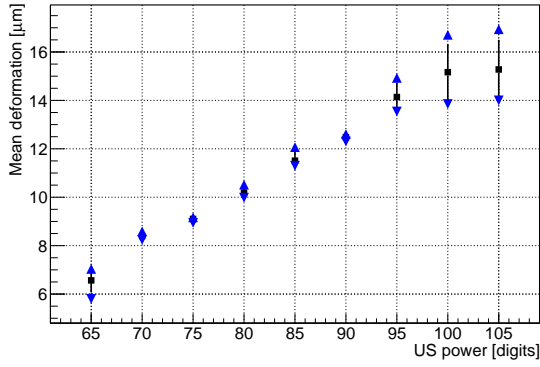


Figure 3.50: Deformation slope development of the destination bond for the variation of the US power.

lift-offs at lower force setup values and still achieve high pull test results with small variances. This value corresponds to a wire deformation value of about  $13\ \mu\text{m}$  (Figure 3.49 (a)). The uncorrected pull test result for this setup value is determined by a linear interpolation to be  $(7.8 \pm 0.4)\ \text{g}$ . The corrected pull test result lies between  $(6.69 \pm 0.43)\ \text{g}$  and  $(9.96 \pm 0.95)\ \text{g}$ . The bond parameters for the module wire bonding are summarized in Table 3.11 including the BPC parameters. The initial US power and the force setup values are used as described. The BPC can adjust the US power in a range of  $\pm 10$  digits. The range is kept small to ensure that the US power stays in the parameter space which generated “good” bond results. Additionally the bond time is increased up to 40 ms. So the machine has more time to achieve the target deformation. As the bonding process is stopped when the target deformation is reached, the expected mean actual bond time is about 35 ms. The target deformation setup is chosen based on the studied wire deformation values of the optimal parameter sets. The deformation tolerances do not affect the bonding process itself but they control the sensitivity of error warnings which stop the machine so that the user can analyze the problem and intervene if necessary. The BPC slope is set to  $55^\circ$  so the machine is able to achieve the target deformation in time without forcing the process to finish too early.

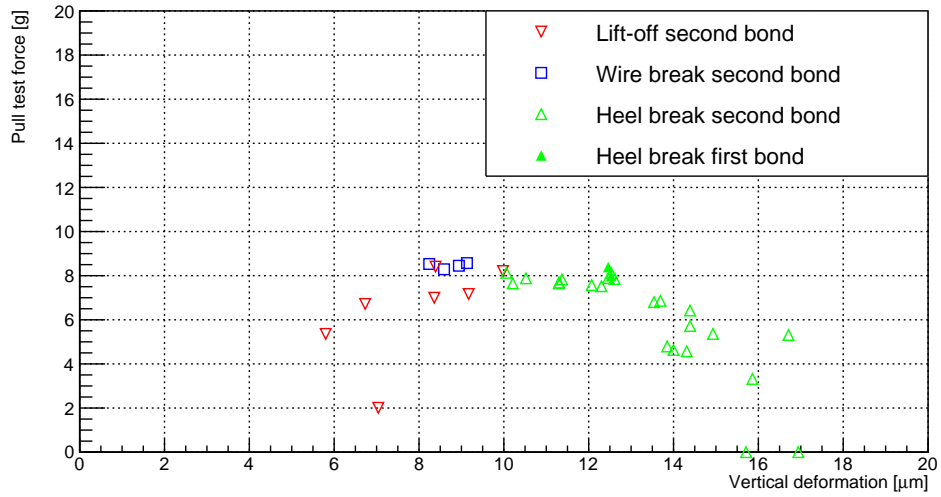
### 3.5.4 The bonding program

The four sides of the 2S module are identical regarding the wire bonding process except for small differences in the height of the sensor and the hybrid. So one side is discussed



(a) Dependence of the deformation and the setup US power.

(b) Dependence of uncorrected pull test results and the setup US power.

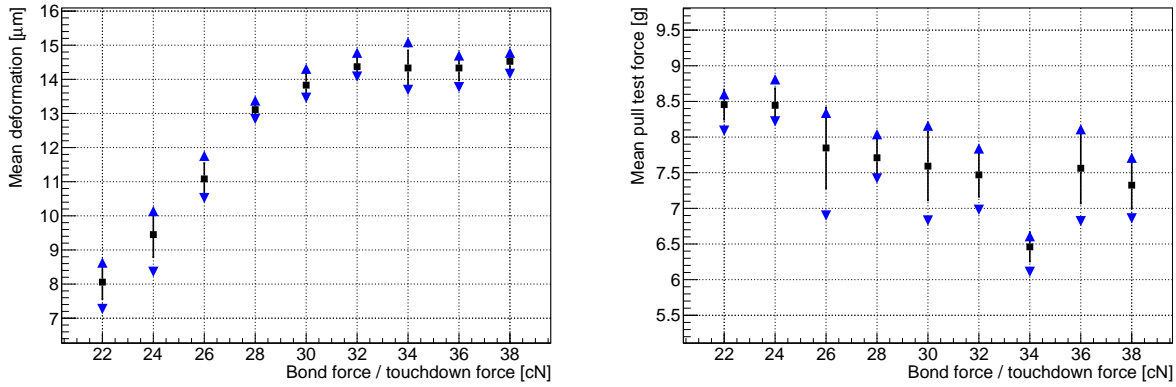


(c) The machine measured deformation is plotted against the pull test result including the failure mode.

Figure 3.51: The plots (a) and (b) show mean values of deformation and uncorrected pull test result in variation of the US power for the destination bond. The error is the standard deviation of the results. The blue triangles indicate the minimum and maximum values. Figure (c) combines both plots including the failure mode.

Side	US power [digits]			BT [ms]	Force [cN]	Deformation [ $\mu\text{m}$ ]			Slope [ $^\circ$ ]
	min.	init.	max.			min.	target	max.	
Hybrid	100	110	120	40	28	10.5	12	13	55
Sensor	80	90	100	40	27	11	12.5	13.5	55

Table 3.11: Summary of the optimized bond parameters for the module wire bonding.



(a) Dependence of the deformation and the setup BF and TDF. (b) Dependence of uncorrected pull test results and the setup BF and TDF.

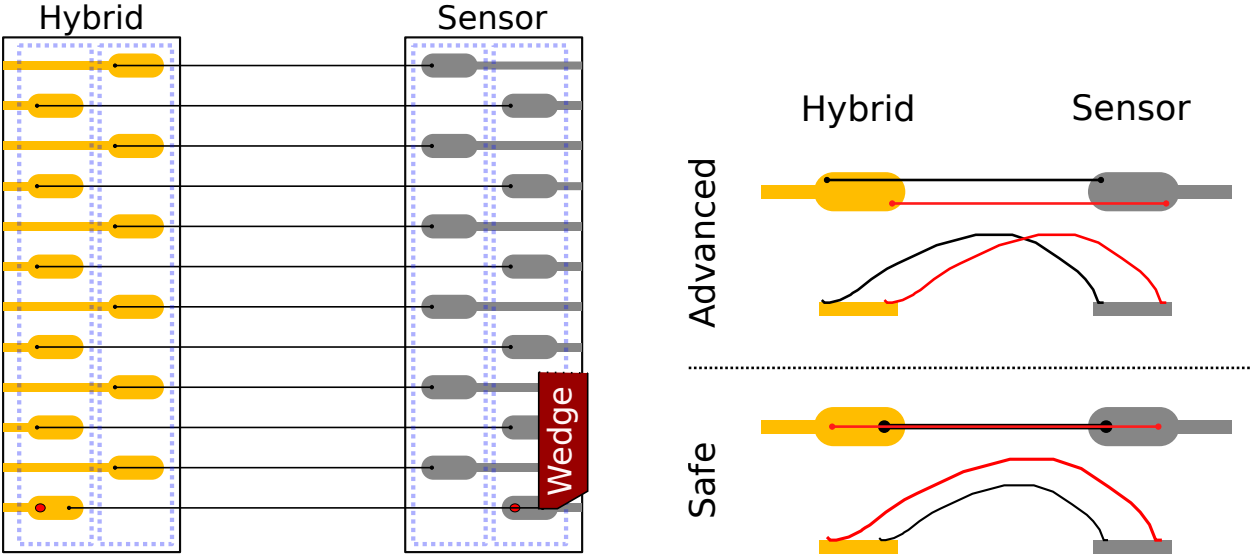
Figure 3.52: The plots (a) and (b) show mean values of deformation and uncorrected pull test result of the destination bond for the variation of the BF and TDF setup value for the source bond. The error is the standard deviation of the results. The blue triangles indicate the minimum and maximum values.

which represents the wire bonding program logic for the whole 2S module. The bonding direction is always chosen from the hybrid to the sensor to achieve a higher distance between the wire and the sensor edge, that is on high voltage. Figure 3.53 (a) shows a sketch of the general module bonding program. There is an inner row of shorter wires and an outer row of longer wires each with 508 wires. The distance from wire to wire within the inner (or outer) row is 180  $\mu\text{m}$ . The bonds of the inner and outer row as well as the hybrid and sensor bonds are programmed on different chips. This is indicated by blue dotted rectangles in Figure 3.53 (a). So for the general module bonding program there are four different chips that can have individual sets of bonding and loop parameters. The loop height is programmed as a constant relative to the loop distance. So the inner wire have a smaller wire height than the longer wires. This increases the actual distance between the wires and might be an advantage in the encapsulation process.

All of the wire bonds are positioned in the corner of the bond pad which is on the side pointing away from the bonding direction (from hybrid to sensor). The advantage is shown for the lowermost wire of the sketch in Figure 3.53 (a) which has to be repaired. In the repairing process the bad or broken wire is removed so that only the bonds remain (shown in red). After removing the bad wire, there is enough space on the other side of the bond pad to place a new wire. The advantage in setting the bonds in this corner of the bond pads is that the bond wedge is not touching the remaining bonds of the bad wire which might decrease the quality of the repair wire bonds.

There is the plan to do periodic quality checks with pull tests during the series production. A possible scenario could be that one module is tested per day. This module is provided

with extra wires for pull tests. These wires are bonded as a second wire for example at every fiftieth wire. Two different methods of placing the extra wire on the same bond pad like the normal one have been tested. The two methods are shown in Figure 3.53 (b). In the *advanced* method the normal wire is placed in the corner of the bond pad pointing away from the bond direction but with a shift perpendicular to the bonding direction. So the extra wire can be bonded in the other corner of the bond pad with a shift in the other direction. This method has the advantage that the extra test wire has the exact same wire geometry like the normal wire. Thus, the test results better represent the actual quality of the module wire bonds. The major disadvantage is that the bond wedge could touch the normal wire during the bonding of the extra wire. The bond pads have a width of about 70  $\mu\text{m}$ . The bond itself is deformed to about 35 to 40  $\mu\text{m}$  in width. So the bond wedge has to be very fine to achieve good results with this method. The width of the bond wedge used for this theses (Table 3.3 on page 22) is 102  $\mu\text{m}$ . The *safe* method avoids this problem by bonding the extra wire enclosing the normal wire. This is also shown in Figure 3.53 (b). The bond wedge can only touch the normal wire at the bond on the hybrid during the bonding of the extra wire if the bond wedge is too long. The disadvantage of this method is that the wire geometry of the tested wire is different and the normal wire is shorter than the other normal ones.



(a) Sketch of the general bonding program logic. The light blue dotted lines highlight the programmed chips. The last wire is shown during the repairing process. The red dots indicate the remaining bonds of the bad wire.

(b) Sketch presenting the two different types of test wires. The red wire represents the test wire, the black wire remains.

Figure 3.53: Sketches visualizing the bonding programs.

The first modules of the production process should be wire bonded with bonding programs that separately bond the inner and the outer row of wires. In doing so, the inner row can

be checked easier and there is more space for repairs. Later the inner and outer row will be bonded in a single program.

The inner and outer wire rows of the dummy module are bonded separately. Each row is provided with 26 extra wires of both methods. So there are in total 52 pull test wires of the advanced bonding method and 52 of the safe method. This enables a quantitative evaluation of the wire bonding process on the dummy module.

### 3.5.5 Determination of the correction factor for the test wires

At this side the hybrid is at a lower height than the sensor due to imperfections of the dummy module. The used formulas assume that the bond, which is corrected with  $K_1$  lies higher than the other bond. This means that the correction factor for the hybrid side has to be  $K_2$ . As the source bond is set on the hybrid, more than 96 % of the wires have broken at the hybrid side. Thus only the corresponding correction factor  $K_2$  is considered. Furthermore, the inner and the outer wires have significantly different lengths so that the correction factors have to be calculated separately.

Figure 3.54 shows the calculated correction factor  $K_2$  for the source bond. The red and turquoise graphs present the correction factor for the inner and outer row of wires using the Delvotec formula. The blue and pink graphs show the correction factor for the inner and outer row of wires using the simple formula. The estimated hook position for the inner row is displayed between the black dotted lines. The green dotted lines contain the estimated hook region for the outer row of wires. The mean correction values for the different graphs in the  $d_1$ -regions are determined analogously to earlier discussed correction factors for the top side of the module. They are summarized in Table 3.12. The correction factor of the inner row lies between  $1.24 \pm 0.21$  and  $1.50 \pm 0.19$ . The correction factor of the outer row of wires is limited by  $1.00 \pm 0.14$  and  $1.54 \pm 0.03$ . Again the correction factors cover relatively wide ranges. So uncorrected pull test forces are plotted and the limits of the corrected pull test forces are discussed.

Formula	Elongation	$K_2$ of the inner row			$K_2$ of the outer row		
		$\mu$	$\sigma$	$\sigma/\mu$	$\mu$	$\sigma$	$\sigma/\mu$
Delvotec	1 %	1.50	0.19	13 %	1.26	0.13	10 %
	4 %	1.24	0.21	17 %	1.00	0.14	14 %
Simple	1 %	1.59	0.05	3 %	1.54	0.03	2 %
	4 %	1.28	0.05	4 %	1.28	0.02	2 %

Table 3.12: Summary of means  $\mu$  and RMS  $\sigma$  of the histograms of calculated correction factors for the pull tests of the inner and outer row of wires.

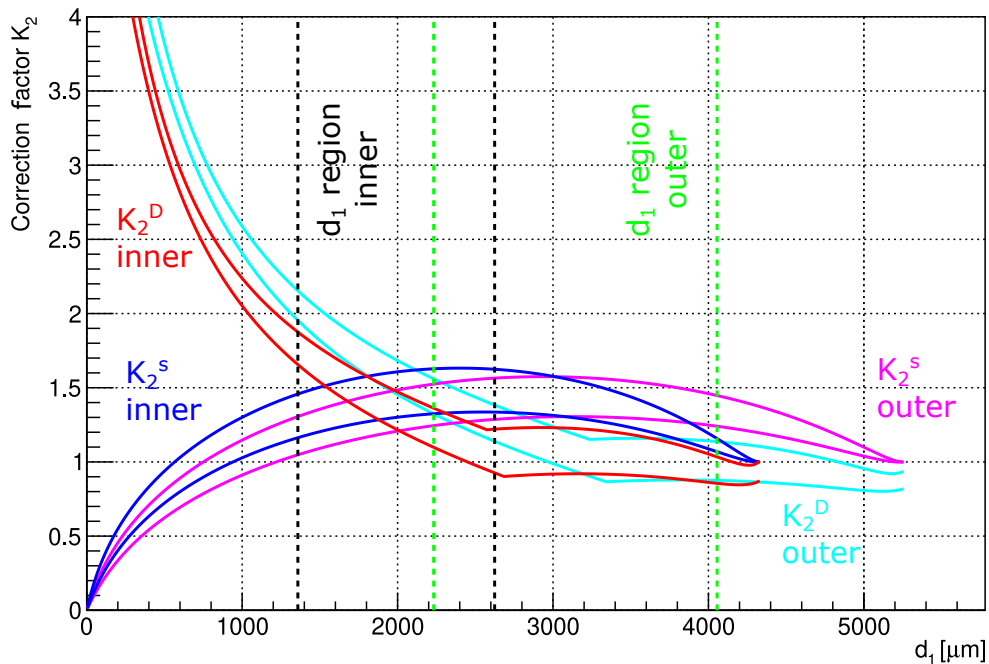


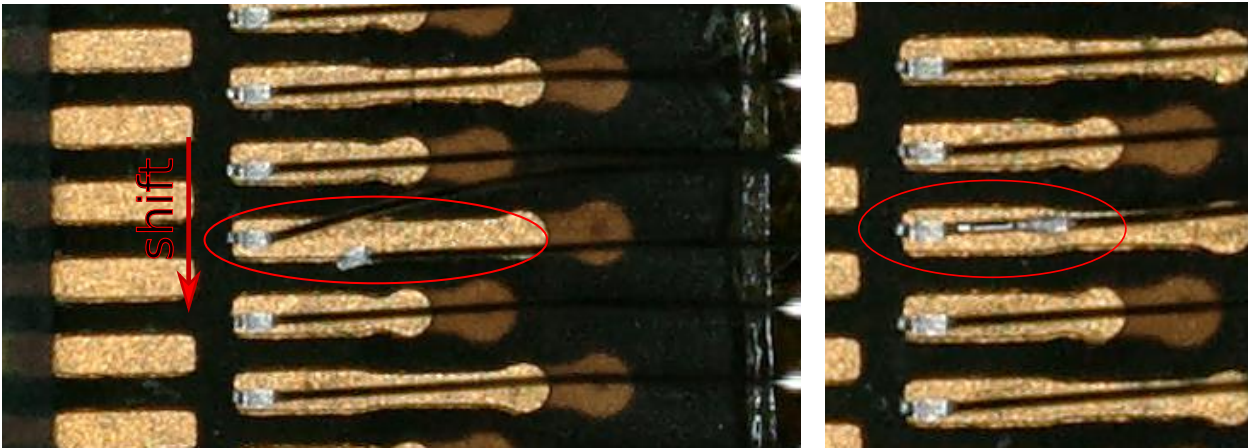
Figure 3.54: The calculated correction factor  $K_2$  plotted against the hook position. The correction factor is calculated using the Delvotec formula for the inner (red) and outer row (turquoise) and using the simple formula for the inner (blue) and outer row (pink). The region contained between the black / green dotted lines presents the estimated hook position for the inner / outer row of wires.

The systematic uncertainty of single pull tests is determined in the hook position region reduced to the most critical 20 % in terms of high relative uncertainties. In case of the inner row of wires, the most critical region is the first 20 %. The worst case appears if the Delvotec formula is correct with an elongation of 4 %. This results in a systematic uncertainty of 4 % for each pull test. In case of the outer row of wires, the most critical region is the last 20 %. The worst case is calculated with the simple formula with an elongation of 1 %. This generates a systematic uncertainty of 1 % for each pull test in the outer row of wires.

### 3.5.6 Analysis of quality tests and issues

The bonding machine has stopped only very few times during the general bonding program in the wire bonding process of the inner row. The machine stopped because minimum deformation has just not been reached. Major problems have been detected during the wire bonding of the additional test bonds, especially the advanced test bonds. All bonds have been wire bonded with a shift of approximately 20  $\mu\text{m}$  perpendicular to the bonding direction, as shown in Figure 3.55 (a). This does not affect the quality of the normal module wires. But in case of the advanced test wires the correct placement is very important as there is

only little space on the bond pad. Therefore many of the advanced test wire bonds are only partially or not at all bonded onto the bond pad. Also, the remaining normal wire is clearly bend to the side by the bond wedge. Figure 3.55 (b) shows another problem. Sometimes the advanced pull wire is not bonded but the wedge welds the normal wire which is already bonded onto the bond pad.



(a) Microscope picture of inner row bonds on the hybrid. The bonds are slightly shifted as indicated by the red arrow. Only half of the advanced pull test bond bonded onto the bond pad (highlighted by a red ellipse). The remaining wire is bend.

(b) Microscope picture of inner row bonds on the hybrid. The advanced pull test bond could not be bonded. Instead the remaining wire is bonded a second time (highlighted by a red ellipse).

Figure 3.55: Problems regarding the wire bonding of the inner row of wires.

The uncorrected pull test results of the test wires of the inner row are shown in Figure 3.56. The blue line separates the advanced from the safe test wires. The displayed error is the relative uncertainty for single wires of 4%. Exactly half of the advanced test wires have not successfully been wire bonded because of the shift problem. These wires are shown with a pull test result of 0 g. The other half consists of 15% heel breaks and 85% lift-offs. If only the successfully bonded wires are considered, the mean pull test result is  $(4.5 \pm 0.3)$  g. The corresponding corrected pull test result lies between  $(5.6 \pm 1.0)$  g and  $(6.8 \pm 1.0)$  g. The safe pull test wires have been bonded successfully at a ratio of 96%, only one wire failed. Most of the successfully bonded wires are detected with heel break (88%). The mean uncorrected pull test value of the successfully bonded wires is  $(5.7 \pm 0.1)$  g. This corresponds to a corrected test result in the limits of  $(7.0 \pm 1.2)$  g and  $(8.5 \pm 1.1)$  g.

Because of the described shift of the bonds, the camera of the bonding machine has been calibrated again before the outer row of wire has been bonded. This has not solved the problem. So the bonds have been programmed with a shift in the opposite direction which compensates the problem. As a result more advanced test bonds have been wire bonded successfully.

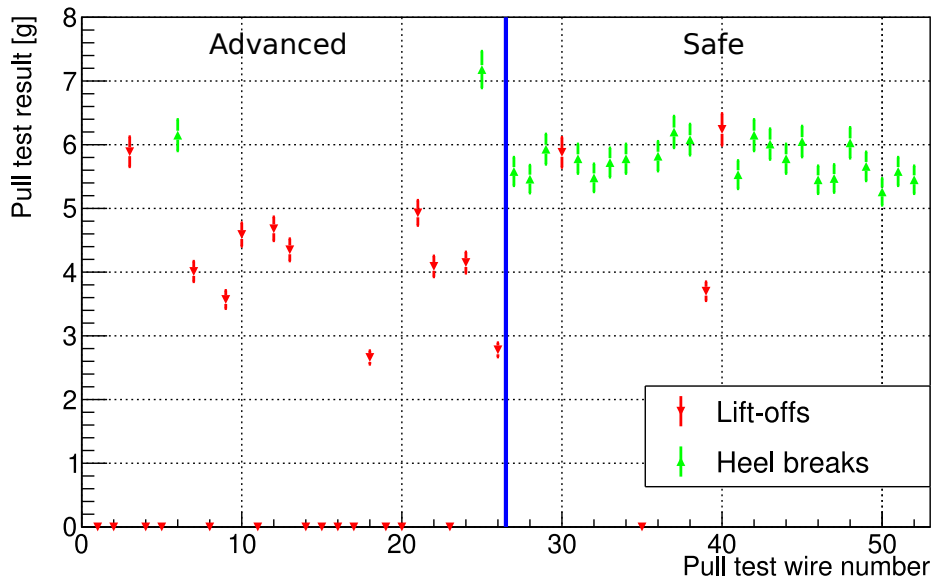


Figure 3.56: Uncorrected pull test results of the inner row test wires.

Figure 3.57 shows the test results of the outer row test wires. The results are again displayed with the relative error of 1 %, but the error is too small to be visible. Instead of 50 % failed advanced test wires, there are 19 % of failed bonded wires after the adjustment of the bond position. Additionally, the part of the successfully bonded test wires which have heel breaks increases from 15 % in the inner row to 38 %. The mean uncorrected pull test result of the successfully bonded advanced test wires is  $(5.8 \pm 0.3)$  g, which translates to a corrected test result between  $(5.8 \pm 0.9)$  g and  $(9.0 \pm 0.4)$  g. Again only a single wire of the safe pull test wires has failed. Surprisingly it is again the test wire with pull test wire number 35, which means that the failed wires lie close together (about  $270 \mu\text{m}$ ). Both wires failed during the wire bonding of the destination bond on the sensor side. Although no contamination or damage has been found in this region, this might be a local problem. There is only one safe test wire of the successfully bonded wires which has a lift-off, making up 4 %. The mean uncorrected pull test result is  $(5.8 \pm 0.1)$  g. This corresponds to a corrected value between  $(5.8 \pm 0.8)$  g and  $(8.9 \pm 0.2)$  g. If only the pull test results of advanced and safe pull wires with heel breaks are compared, the advanced pull wires generate higher results. The mean of the advanced method is  $(6.6 \pm 0.1)$  g and the mean of the safe method is  $(5.8 \pm 0.1)$  g. This difference might be the result of the slightly different wire geometries.

The pull tests performed on the dummy module have shown that the advanced method requires a wedge which is finer than the used one. Almost all failed bonds of the advanced test wires originate from bad positioning on the bond pad. Furthermore, the remaining wire has always been scratched and bend by the wedge. So, further tests have to be done to study the feasibility of the advanced method. The safe method seems to be a good alternative with

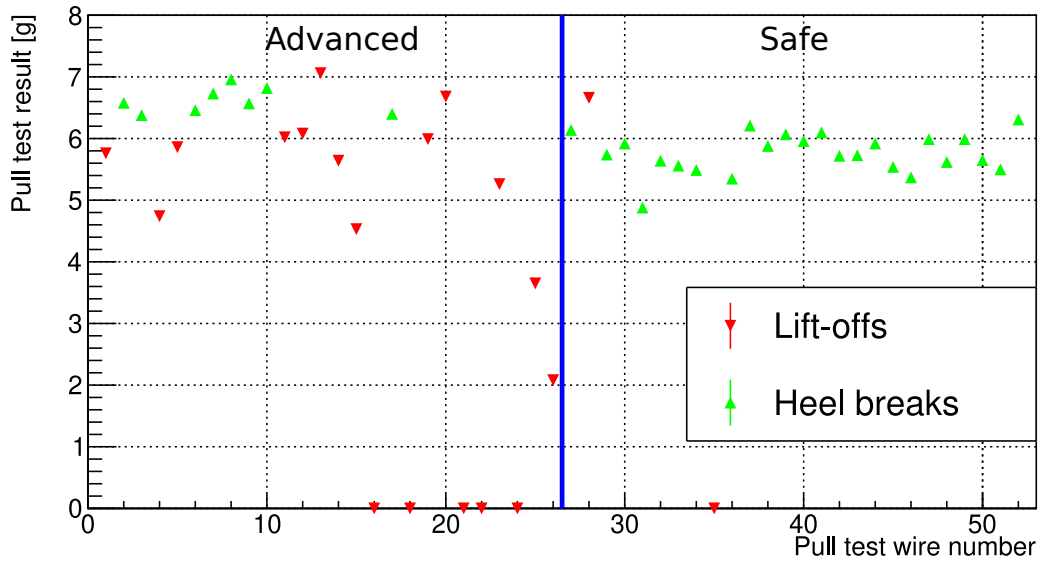


Figure 3.57: Uncorrected pull test results of the outer row test wires.

the disadvantage that the different wire geometry seems to have an impact on the pull test result.

# 4 Encapsulation

This chapter deals with the wire bond encapsulation. In Chapter 4.1 the encapsulation process is introduced and the boundary conditions are described. Furthermore different glue candidates for the wire bond encapsulation of the 2S module are discussed. In Chapter 4.2 a self made automated dispensing system is described. Chapter 4.3 presents the results and findings gained in dispensing tests of the discussed glues. In Chapter 4.3.3 electrical effects on actual detector modules are tested.

## 4.1 Overview

Wire bond encapsulation is done to protect the thin and fragile wires from damage. There is always the risk to mechanically damage the wires by touching them or during the transport to the experiment. As the 2S module has wire bonds on the top and bottom side at each FE-hybrid there is a high risk to accidentally touch wires during the installation in the experiment without even recognizing the accident. Furthermore, the wires could break because of corrosion. A third source of danger for the wires is the the change of electric current in a strong magnetic field which might cause Lorentz resonances that could break the wires.

The goal of the encapsulation is to completely wrap the wires with the encapsulant. The encapsulation process has to be achieved with high repeatability and precision as the material budget is very important in the design of tracker detectors. For this an appropriate glue has to be found and a dispensing system for the series production has to be set up. As the modules are designed to work in a harsh radiation environment, the glue has to be radiation resistant. So tests have to be performed to show that the properties of the encapsulant are stable up to 1.25 MGy [32]. Additionally, the glue has to pass aging tests with rapid thermal cycles in the range from  $-35^{\circ}\text{C}$  to ambient temperature to simulate the environment in the detector. The glue has to be soft and must not shrink or expand too much during thermal cycles so that wires might break. It has to be electrically highly resistive to prevent sparkover at the high voltage at the sensor and of course crosstalk between the wires. The encapsulant has to have the optimal viscosity so that it can flow through the wires but does not flow

through the gap between the sensor and the FE-hybrid. The pot life<sup>1</sup> and the curing method also play an important role in the process during the series production.

Three glues have been recommended for test studies by the CERN bond lab. They are listed with the most important properties in Table 4.1. The *Polytec EP 610* is a transparent two-component (2K) epoxy glue with low viscosity of 0.8 Pa·s at room temperature (RT) and relatively high flexibility [33]. The resin is mixed with the hardener at a ratio of 100:50. *Sylgard 184* and *Sylgard 186* are both silicone based 2K encapsulants with very different viscosity values (RT) of 3.5 Pa·s and 66.7 Pa·s and differences in flexibility [34, 35]. They are both mixed at a ratio of 10:1. The three encapsulant candidates additionally have very different pot life times which has to be considered in the dispensing process. Polytec EP 610 has the highest pot life of six hours. Sylgard 184 and Sylgard 186 only have a pot life of 1.4 and 1.65 hours. So both Sylgard glues have to be processed quickly as the viscosity changes directly after the mixing.

Encapsulant	Polytec EP 610	Sylgard 184	Sylgard 186
Pot life [h]	6	1.4	1.65
Viscosity (RT) [Pa·s]	0.8	3.5	66.7
Mixing ratio [resin:hardener]	100:50	10:1	10:1
Elongation [%]	60	120	255
Durometer shore	65	44	24

Table 4.1: Overview of the tested encapsulant candidates.

There are two commonly used methods for the encapsulation of electronic components [36]:

1. **Glob top:** the encapsulation with the glob top method is sketched in Figure 4.1 on the bottom side. A single encapsulant material is dispensed over the component. The encapsulant has to be chosen in a way that it disperses over the complete component without contaminating neighboring parts of the component. The encapsulant has to be chosen precisely according to an appropriate viscosity to achieve good results.
2. **Dam-and-fill:** the glob top method can be quite difficult as the feasible range of viscosity of the encapsulant is very small. This problem is eliminated by using two different glues instead of a single one. The first glue with a high viscosity is used to form a dam. The dam is filled with the second glue which is a very fluent encapsulant. Figure 4.1 presents the result of this method on the top side.

The glob top procedure requires far less gluing steps resulting in much shorter production times during the series production. So this method is focused on.

---

<sup>1</sup>The pot life is the time from from mixing a glue until the velocity changes so that it cannot be dispensed anymore.

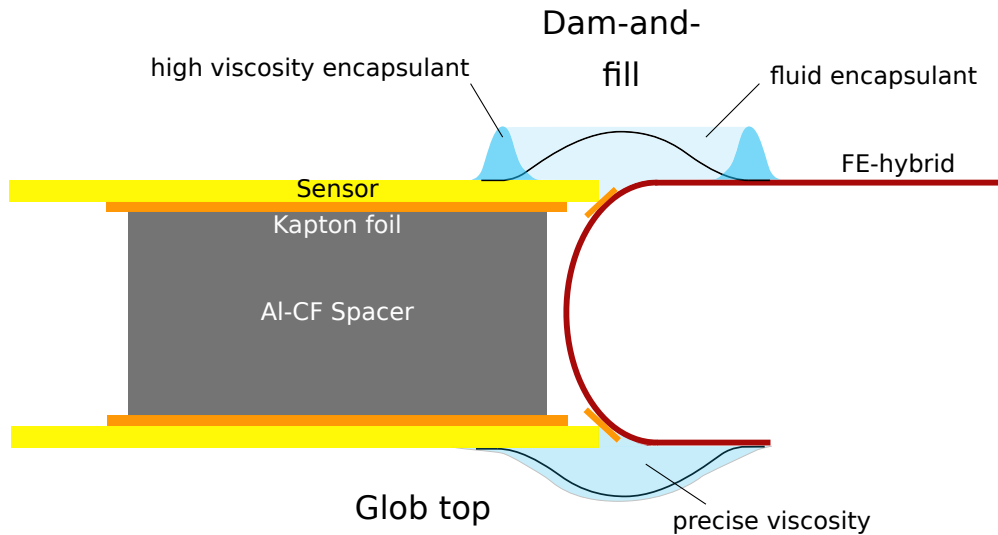


Figure 4.1: Sketch of an encapsulated 2S module using the dam-and-fill method on the top side and the glob top method on the bottom side.

## 4.2 Encapsulation setup

The glues are mixed using the *Smartmix X2* by the manufacturer *Amann Girbach* [37]. Individual mixing programs can be programmed for different glues. The mixing is carried out with applied vacuum to erase bubbles and achieve a good homogeneity.

Dispensing tests of the three discussed encapsulant candidates have been performed using a self made dispensing robot. It consists of the time pressure controlled dispenser *Ultra 1400* by *Nordson EFD* [38] which is installed onto an *xyz*-axis table by *Isel*. The glue is filled into a cartridge that is connected with the dispenser via a flexible tube. This connects the cartridge with the pressurized air which controls the flow of the glue. There are many different types of needles which can be plugged to the tip of the cartridge. They vary in terms of diameter, material, angle of slope and form. The cartridge is mounted onto the *Isel* table with a mounting designed and produced by the workshop of the *III. Physikalisches Institut RWTH*. Figure 4.2 shows the cartridge mounted onto the *xyz*-table. The *Isel* table is connected to a computer via serial interface. The dispenser is controlled using the *USB-6008* multifunction I/O device by *National Instruments* [39]. This device sends a 5 V signal to the nine-pin interface connector of the dispenser to start the pressurized air. A signal of 0 V stops the dispensing process. The pressure of the dispenser is set via a rotary knob and displayed by an analog display. Another rotary knob is available to control the vacuum which is active when the dispensing process is inactive. This prevents the glue from flowing out of the needle.

The control of the *xyz*-axis table and the dispenser is combined in a *Labview* program. It provides functions to move the cartridge with defined velocities. This function is used to align the needle above the substrate and to find the optimal needle height. Another function

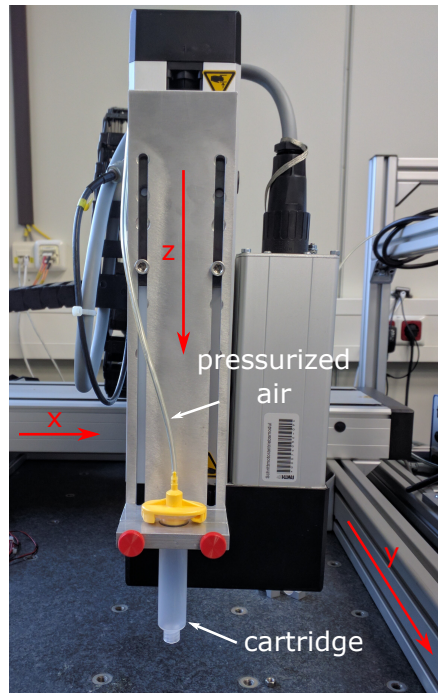


Figure 4.2: Photograph of the self made dispensing robot.

performs the dispensing process. The needle is moved down to the set up needle height and the pressurized air is activated. Then the needle is moved with a set up velocity while dispensing the glue on a straight line with a given length. At the end the system moves the needle up again and can optionally repeat this process after a user-defined time with a distance that also has to be defined. This optional feature allows to test the impact on the dispensing result of viscosity changes over time.

## 4.3 Encapsulation tests

### 4.3.1 The different degrees of freedom

First dispensing tests have been performed on thin glass plates using Polytec EP 610. The goal of these tests has been to get a first impression of the most critical degrees of freedom and to study their impact on the dispensing results. The performed tests are evaluated qualitatively and should be understood as preparation for more advanced tests. The results are summarized in the following.

There are three degrees of freedom which can be used to control the amount of glue that is dispensed: the inner diameter of the needle, the pressure setup of the dispenser and the velocity of the needle during the dispensing process. If a glue with high viscosity is used, of course a higher needle diameter has to be preferred. As the viscosity changes during the pot life this has to be taken into account and in the ideal case it is compensated by increasing

the pressure or decreasing the velocity. Additionally, the correct adjustment of the dispenser vacuum is very important. It is set up by slowly increasing the vacuum until the glue stops flowing through the needle. If the vacuum is too strong, air is sucked through the cartridge creating air bubbles within the glue. This significantly worsens the dispensing result because the glue loses its homogeneity. Since the amount of glue in the cartridge changes, the vacuum has to be readjusted regularly. Another very critical parameter is the height of the needle above the substrate. Obviously the substrate can be damaged if the needle height is too low. On the other hand if the needle is set up too high above the substrate, the glue is accumulated at the tip of the needle and a drop with increasing size is formed. The glue drop then finally slips off from the tip of the needle when the drop reaches a critical size or when it touches the substrate's surface. As a result, a line of glue dots is dispensed instead of a continuous glue line. Needles with a sloped tip do not seem to increase the feasible range of needle height. The optimal needle height lies approximately in the order of the inner diameter of the needle. During tests with the low viscosity Polytec EP 610, needles with inner diameters between about 250 and 500  $\mu\text{m}$  have been used. If a system is used which requires a manual setup of the needle height above the substrate, slopes in the surface of the substrate can be a huge problem.

### **4.3.2 Viscosity of the different glues**

The three glues have very different viscosities according to the values from the manufacturer data sheets. The glues are dispensed onto thin glass plates and the dispensing result is compared to get a feeling of how the different viscosity values affect the deliquescence. Polytec EP 610 has a long pot life of six hours. This allows to test the development of the dispensing behavior over time. Comparable tests have not been performed with Sylgard 186 and Sylgard 184 since the pot life is too short.

The Polytec encapsulant has been dispensed eighteen times with an interval of twenty minutes to test the viscosity over the entire pot life. Figure 4.3 shows a photograph of the dispensing result. The picture contrast has been increased and a contour scan has been performed for better recognition of the glue lines. At the beginning, the glue deliquesces randomly and the glue lines are rather broad. After about three hours (corresponding to glue line number 9) the change of the viscosity is clearly visible in the shape of the dispensed glue lines. They are much more straight and for about one and a half hours the shape of the lines is well reproducible. After about four and a half hours of pot life (line number 14) the line width further decreases and the glue is much more deformed.

The mixture of Sylgard 184 and the mixture of Sylgard 186 as well as preparations of the dispensing robot have to be done fast because their pot life is short. Sylgard 184 proves to be similar to Polytec EP 610 in the behavior during the dispensing process. A striking difference

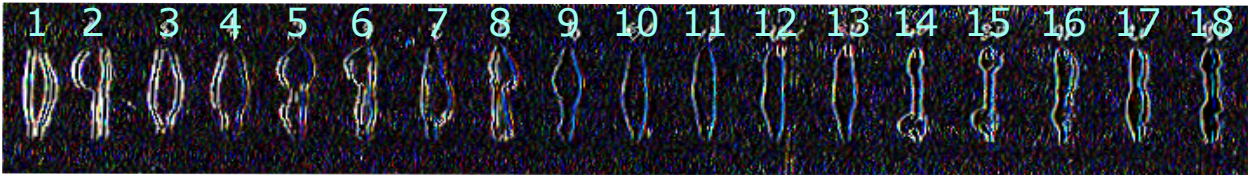


Figure 4.3: Dispensing tests of Polytec EP 610. The glue lines are dispensed with intervals of twenty minutes.

between the two glues is that Polytec EP 610 stops deliquescing shortly after the dispensing while Sylgard 184 deliquesces for a much longer time. This is a disadvantage of Sylgard 184 as it is much harder to control the final shape of the glue. Figure 4.4 (a) shows a photograph of Sylgard 184 glue lines dispensed from right to left. Another striking disadvantage is the low time of usage. So Sylgard 184 seems not to be a good solution as standalone encapsulant for a glob top encapsulation of the wire bonds. Sylgard 186 on the other hand has a very high viscosity compared to Polytec EP 610 and Sylgard 184. Figure 4.4 (b) shows a photograph of Sylgard 186 glue lines during the dispensing tests. The glue deliquesces much less which makes it much easier to control the shape of the glue. Furthermore needles with higher inner diameters are used which reduces the problem of finding the right needle height.



(a) Sylgard 184.



(b) Sylgard 186.

Figure 4.4: Photographs of dispensing tests of Sylgard 184 and Sylgard 186.

### 4.3.3 Tests on wire bonds

The actual encapsulation of bonded wires is tested on spare TOB1 modules (tracker outer barrel) of the Phase-0 CMS detector. Figure 4.5 shows a photograph of a module which has been used for encapsulation tests. TOB1 modules consist of two strip sensors which are connected with wire bonds [6, 14]. They have 768 strips with a pitch of  $122\ \mu\text{m}$ , so the distance between the wires is  $32\ \mu\text{m}$  higher compared to the wire distance on the 2S module. The wire length is about 4 mm which is comparable to the inner row of wires of the 2S module. The strips are read out by APV25-S1 chips which amplify and shape the signal. The TOB1 module has six APV chips which read out 128 strips each.

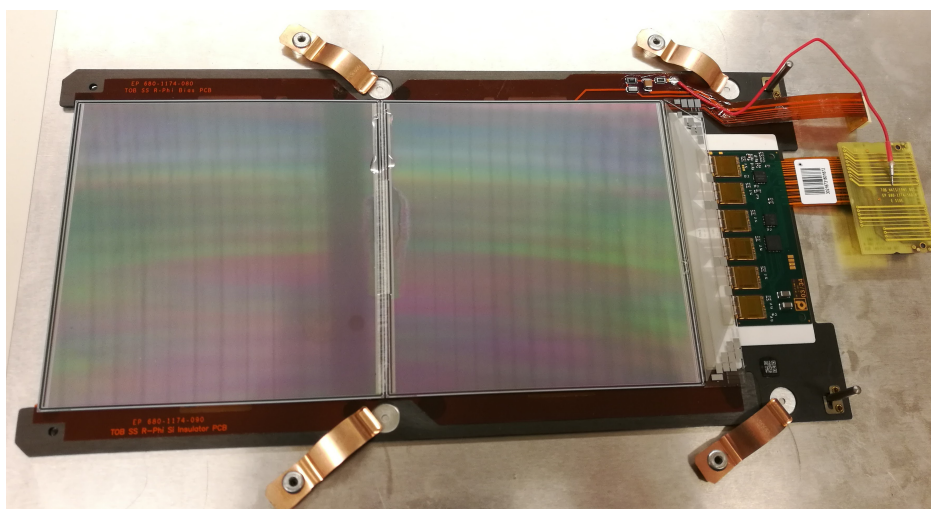


Figure 4.5: Photograph of a TOB1 module which has been used for encapsulation tests.

The result of the encapsulation test of Sylgard 186 on the wires of the TOB1 module is shown in Figure 4.6. To encapsulate the entire wires it was necessary to dispense the glue as five glue lines (perpendicular to the wire direction) at various positions of the wire. The glue seems to flow through the wires and does not contaminate large areas of the sensor surface. Therefore, this first test of Sylgard 186 on wires is evaluated as a success in terms of the feasibility. As the distance between the wires is slightly higher than for the 2S module, further tests have to be performed for a final evaluation. If there are problems with the viscosity being too high, Sylgard 186 can be mixed with Sylgard 184 to adjust the viscosity. Tests with a mixture of the two encapsulants remain to be performed.

Figure 4.7 shows the result of the encapsulation test of Polytec EP 610 on wires. The glue is dispensed as two glue lines at various positions of the wire. Because the viscosity is very low and the surface tension is high, the wires are coated with a thin layer of glue. It seems that the spacing below the wires is completely filled with the encapsulant but it is rather difficult to check this without damaging the wires. The low viscosity also results in more contamination of the sensor surface. After curing the glue becomes very stiff. This might be

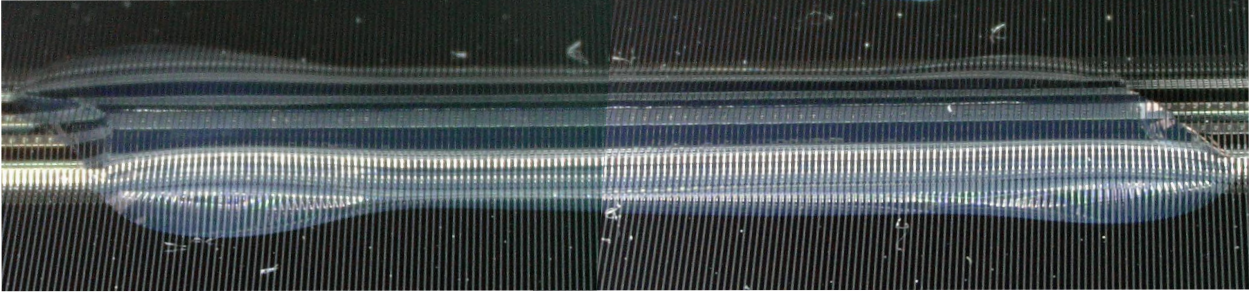


Figure 4.6: Photograph of an encapsulation test of Sylgard 186 on wires of a TOB1 module. The picture consists of two photographs that have been merged.

a problem if the glue expands or shrinks at high temperature changes. So tests need to be performed exposing the encapsulated wires to thermal cycles.

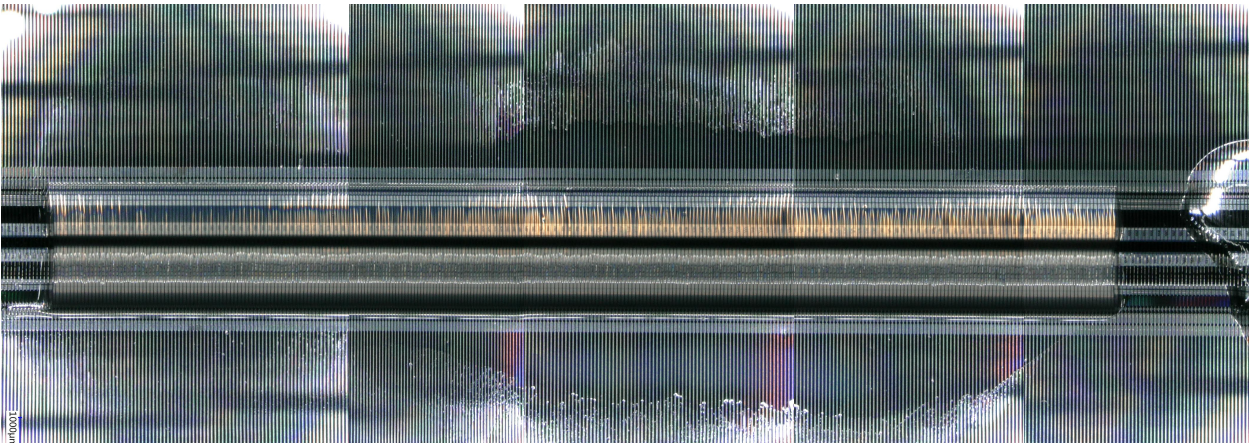


Figure 4.7: Photograph of an encapsulation test of Polytec EP 610 on wires of a TOB1 module. The picture consists of five photographs that have been merged.

The direct influence of the encapsulation is tested by performing noise measurements before and after the glue dispensing. The TOB1 module is read out using an ARC (APV read-out controller) test setup which has been used for quality checks of the Phase-0 strip-tracker modules [40]. For this ten thousand ( $N$ ) noise events are measured using a pulser as trigger. The different channels do not output the same level of ADC (Analog-to-Digital-Converter) counts when no signal is applied on the chip [41] but a signal called pedestal ( $PED$ ). The pedestal signal is determined for every channel  $i$  as mean value of the raw signal data ( $RAW$ ):

$$PED_i = \frac{\sum_{n=1}^N RAW_i^n}{N}. \quad (4.1)$$

Electronic noise pick-up at the preamplifier inputs causes an extra offset called common mode noise ( $CMN$ ) [41]. The common mode noise is calculated assuming that groups of

$N_{ch} = 32$  channels forming four groups ( $g$ ) are affected by the same noise. It is calculated event by event:

$$CMN_g^n = \frac{1}{N_{ch}} \sum_{i=g \cdot N_{ch}}^{(g+1) \cdot N_{ch} - 1} (RAW_i^n - PED_i). \quad (4.2)$$

The common mode subtracted noise  $NOI$  of the signal is determined by

$$NOI_i = \sqrt{\frac{\sum_{n=1}^N \left( RAW_i^n - PED_i - CMN_{g(i)}^n \right)^2}{N - 1}}. \quad (4.3)$$

The common mode subtracted noise of the TOB1 module is shown in Figure 4.8 before (red) and after the encapsulation with Sylgard 186 (blue) and Polytec EP 610 (green). Polytec EP 610 encapsulates the wires from strip number 240 up to 550. The wires from strip number 550 to about 760 are encapsulated with Sylgard 186. After the encapsulation with Sylgard 186, the common mode subtracted noise has not visibly changed. The distribution perfectly fits to the noise distribution without encapsulant. Polytec EP 610 has been dispensed about two months later. The noise measurement shows slight changes in the noise distribution but only in the region of the Sylgard 186 encapsulant. The result has been reproduced. This slight change is not of a relevant order of magnitude but it might indicate aging effects of the glue. This has to be checked in further tests.

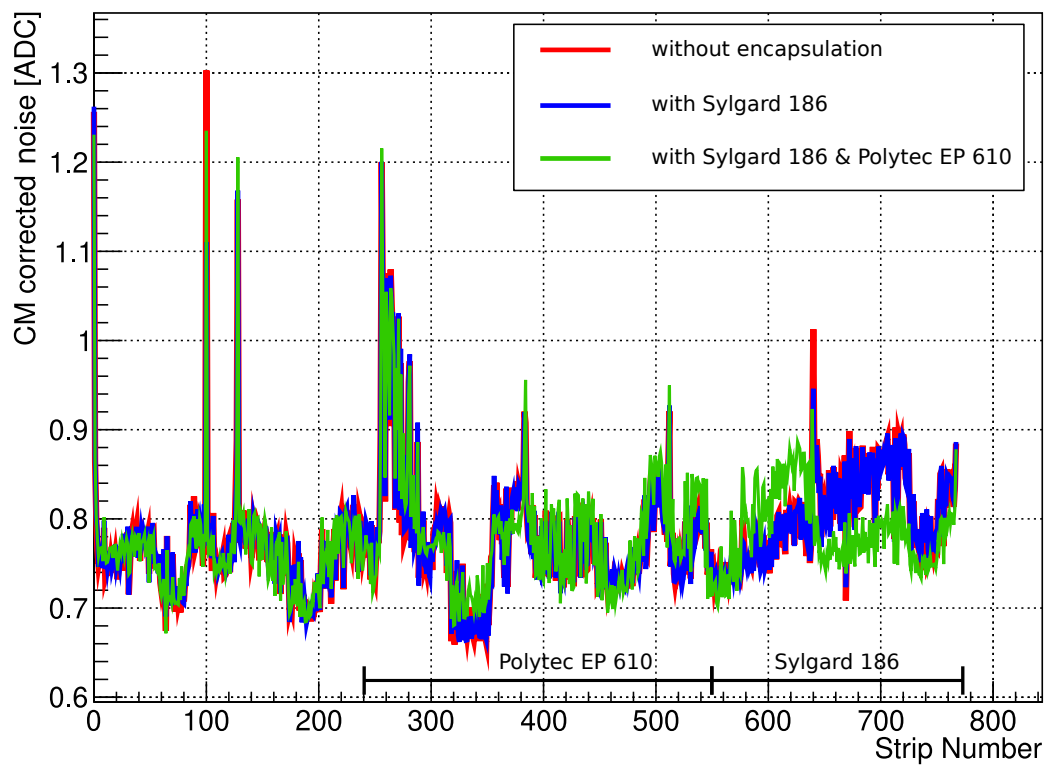


Figure 4.8: Comparison of the common mode corrected noise measurements of a TOB1 module without encapsulation (red), with only Sylgard 186 (blue) and with both Sylgard 186 and Polytec EP 610.

## 5 Summary and Outlook

In the framework of this master thesis the wire bonding process on 2S modules has been prepared for the series production. For this, the acquisition of the bond machine has been supported by defining requirements for the machine which should reduce the effort of manpower during the series production. This could be realized by a conveyor system which enables an automated processing of the tracker modules. The different bond parameters (US power, bond force, touchdown force and bond time) as well as BPC features have been studied and a procedure of parameter optimization has been presented. The US power and the bond force should be chosen so that lift-offs are avoided and pull test forces are maximized. Usually, the value of the touchdown force can be set to be the same as for the bond force. Furthermore, high parameter values of the bond time should be preferred. The BPC turned out to stabilize the quality of the bonds and to compensate for imperfections during the bond process. However, the machine-measured wire deformation seems to be wrong if the BPC is activated and the set up target deformation has been exceeded. The procedure of optimization has been applied to a dummy 2S module. In the preparation of the module wire bonding, the alignment of the aluminum rods which support the FE-hybrids has turned out to be a potentially critical source of failure. Not a single wire has failed during the actual wire bonding process although the dummy module has not been perfectly clean and free from scratches. Furthermore two different types of pull test wires have been presented and studied. The advanced method is in principal much better as the pull test wires have an identical geometry to the normal ones and hence it is more representative. But the used bond wedge is too coarse for this application. In addition, the accuracy of pull tests has been studied. The effective pull test result of course strongly depends on the formula used to calculate the correction factor but also the wire elongation and the position where the pull test hook is applied. So it is extremely important to explicitly describe the procedure of wire pull tests to allow comparability and settle on certain benchmark criteria. The current knowledge only allows to determine a coarse range of the effective pull test result.

Besides the wire bonding itself, also the encapsulation of the wires has been studied. A dispensing robot has been installed and the most critical features and parameters of the dispensing process have been discussed. The dispensing result has turned out to be especially sensitive to changes of the needle height above the substrate. The optimal needle height has been achieved at heights of the order of the inner needle diameter. So the correct

adjustment is an extremely challenging task especially if the substrate itself is not flat and may have a slope. Three different 2K glues have been tested as candidates for the wire bond encapsulation of 2S modules: Polytec EP 610, Sylgard 184 and Sylgard 186. Polytec EP 610 has the advantage of a comparably long pot life. However, it might be too stiff and the viscosity seems to be too low. The last point also holds for Sylgard 184 which additionally has a much shorter pot life. This disqualifies the glue as a standalone encapsulant for glob top encapsulation. Sylgard 186 on the other hand has a high viscosity which enables highly controllable dispensing without much contamination of neighboring material but tests have to show that the glue also flows through wires with distances of about 90  $\mu\text{m}$ .

Still further work is required to prepare the wire bonding of the series production of 2S modules. A further study could be performed to reveal the correct method to determine the effective pull test result. Simulations might help to define a realistic mathematical description of the pull process. Then, benchmark results and a common test method have to be defined. Therefore studies should be performed using a finer bond wedge to repeat tests of the advanced pull test method. To further improve the automated wire bonding in the series production, the BPC features might be used for failure identification and quality monitoring. Only first tries have been done which could be continued. Additionally, the machine does not provide a sensor system checking the length of the remaining wire of the wire spool. This feature could be added to improve the automated wire bonding procedure and to simplify the technicians' job during the series production. The encapsulation process has only been studied qualitatively to learn the methods and get a feeling of the dispensing process. Future tests have to prove the feasibility of encapsulating the wires with a certain glue. This includes thermal cycle tests as well as irradiation tests. Additionally the encapsulation process has to be optimized for the series production.

# List of Figures

2.1	Sketch of the CMS detector layout [13]. . . . .	5
2.2	Trigger concept of the Phase-2 Tracker [3]. The correlation of the closely aligned sensors allows to define a trigger criterion. The hit pairs are referred to as stubs (black rectangles). Stubs lying within the acceptance window (green) correspond to high- $p_T$ particles. Low- $p_T$ particles are rejected. . . . .	8
2.3	Sketch of the Phase-2 tracker [10]. One quarter of the tracker is displayed in the $r - z$ view. The Inner Tracker consists of pixel modules with two (green) and four (yellow) readout chips. The Outer Tracker is built up of PS modules (blue) and 2S modules (red). . . . .	9
2.4	Sketches of the 4.0 mm version of the 2S module [10]. . . . .	10
3.1	Procedure of wedge-wedge-bonding. The green line represents the aluminum wire. . . . .	13
3.2	Screenshot of the bonding machine software panel for the loop geometry. . . . .	14
3.3	Photographs of the bond wedge taken using the <i>Tool Check</i> mode of the bond machine. The red dotted line indicates the position of the wire inside the wedge. The cutout regions and important areas of the bond wedge are highlighted by the black dotted line. . . . .	14
3.4	Failure modes for destructive pull tests. . . . .	15
3.5	Sketch illustrating the calculation of the correction factors for pull tests. . . . .	16
3.6	This plot shows the relative difference between the correction factors for the first bond calculated by using the Equations 3.5 and 3.3 for $\alpha$ and $\beta$ in the range of $5^\circ$ to $65^\circ$ . . . . .	18
3.7	Sketch visualizing the most relevant measures for visual inspections. . . . .	20
3.8	The bonding machine. . . . .	21
3.9	Example of a deformation curve which is displayed during the wire bonding process and saved for offline analysis. . . . .	22
3.10	Photograph of the wire bonding jig for the 2S module. . . . .	23
3.11	Standard jig. . . . .	24

3.12 Photograph of the pull test machine *Dage Series 3000*. An extra light source is positioned on top of the pull test machine. The installed hook is a special hook which is only used for calibrations. . . . . 25

3.13 Photograph of the wire bond test material by *Cicorel*. The structure highlighted with red color indicates the regions used for test programs. . . . . 26

3.14 Sketch of the geometry of the test programs. The sketch is not to scale. The yellow area represents one of the  $4 \times 4 \text{ mm}^2$  squares. . . . . 27

3.15 Microscope picture of the test program wire geometry. The red bar illustrates the estimated region of the position of the pull hook. . . . . 28

3.16 Calculation of the correction factor. The red curves shows the correction factor  $K_1$  calculated by using the Delvotec formula. The same correction factor calculated using the simple formula is displayed as blue curve. The upper curve of those is calculated with an elongation factor of 1%, the lower curve with an elongation factor of 4%. The region highlighted by the green dotted lines represents the estimated region of the hook position. . . . . 29

3.17 Randomly generated  $K_1$  using the two different formulas with an elongation of 1 or 4%.  $d_1$  is generated within the region highlighted in Figure 3.16. . . . 30

3.18 Randomly generated  $K_1$  using the two different formulas with an elongation of 1 and 4%.  $d_1$  is generated within the last 20% of the estimated region for the hook position. . . . . 31

3.19 Mean values of the wire deformation plotted against the setup value of the US power. The blue triangles indicate the maximum and minimum values. The displayed error is the standard deviation of the deformation distribution of a single setup value. . . . . 33

3.20 Deformation slope development for variation of the US power. The different US power settings can be distinguished by differently colored markers as specified in the legend. . . . . 33

3.21 Uncorrected pull test results in dependence of the US power setup value. The blue triangles indicate the maximum and minimum values. The displayed error is the standard deviation of the pull test result distribution of a single setup value. . . . . 34

3.22 Uncorrected pull test results in dependence of the machine measured deformation. The variation of deformation is achieved by a variation of the US power. The failure mode is indicated by green (heel break) and red (lift-off) colored markers. . . . . 35

3.23	Mean values of the wire deformation plotted against the setup value of the BF. The blue triangles indicate the maximum and minimum values. The displayed error is the standard deviation of the deformation distribution of a single setup value. . . . .	35
3.24	Deformation slope development for variation of the BF. The different BF settings can be distinguished by differently colored markers as specified in the legend. . . . .	36
3.25	Uncorrected pull test results in dependence of the BF setup value. The blue triangles indicate the maximum and minimum values. The displayed error is the standard deviation of the pull test result distribution of a single setup value.	37
3.26	Uncorrected pull test results in dependence of the machine measured deformation. The variation of deformation is achieved by a variation of the BF. .	37
3.27	Mean values of the wire deformation plotted against the setup value of the TDF. The blue triangles indicate the maximum and minimum values. The displayed error is the standard deviation of the deformation distribution of a single setup value. . . . .	38
3.28	Deformation slope development for variation of the TDF. The different TDF settings can be distinguished by differently colored markers as specified in the legend. . . . .	39
3.29	Uncorrected pull test results in dependence of the TDF setup value. The blue triangles indicate the maximum and minimum values. The displayed error is the standard deviation of the pull test result distribution of a single setup value.	40
3.30	Uncorrected pull test results in dependence of the machine measured deformation. The variation of deformation is achieved by a variation of the TDF. The failure mode is indicated by green (heel break) and red (lift-off) colored markers. . . . .	40
3.31	Mean values of the wire deformation plotted against the setup value of BT. The blue triangles indicate the maximum and minimum values. The displayed error is the standard deviation of the deformation distribution of a single setup value. . . . .	41
3.32	Deformation slope development for variation of BT. The different BT settings can be distinguished by differently colored markers as specified in the legend.	41
3.33	Uncorrected pull test results in dependence of the BT setup value. The blue triangles indicate the maximum and minimum values. The displayed error is the standard deviation of the pull test result distribution of a single setup value.	42

3.34	Uncorrected pull test results in dependence of the machine measured deformation. The variation of deformation is achieved by a variation of the BT. The failure mode is indicated by green (heel break) and red (lift-off) colored markers. . . . .	43
3.35	Sketch presenting the different slope setup values. The red graph shows an artificial wire deformation curve. The black dotted lines present the slopes generated with the setup values. Note that the axes are plotted in units of bond time and target deformation. . . . .	44
3.36	Mean values of the wire deformation plotted against the setup value of the BPC slope. The blue triangles indicate the maximum and minimum values. The displayed error is the standard deviation of the deformation distribution of a single setup value. . . . .	45
3.37	Deformation slope development for variation of BT. The different slope settings can be distinguished by differently colored markers as specified in the legend. . . . .	46
3.38	Uncorrected pull test results in dependence of the BPC slope setup value. The blue triangles indicate the maximum and minimum values. The displayed error is the standard deviation of the pull test result distribution of a single setup value. . . . .	47
3.39	Uncorrected pull test results in dependence of the machine measured deformation. The variation of deformation is achieved by a variation of the BPC slope. The failure mode of all tested wires is heel break. . . . .	47
3.40	Visualization of the wire deformation to describe the mathematical model. . . . .	48
3.41	The mean horizontal deformation is plotted against the mean vertical deformation with the standard deviation as error. The deformation is changed by a variation in BF with <i>deactivated</i> BPC. . . . .	49
3.42	The mean horizontal deformation is plotted against the mean vertical deformation with the standard deviation as error. The deformation is changed by a variation in BF with <i>activated</i> BPC. . . . .	50
3.43	Comparison of the quality of bonds with activated (blue) and deactivated (red) BPC. The pull test results are uncorrected. The displayed error is the standard deviation. The triangles indicate maximum and minimum values. . . . .	51
3.44	Photographs of the 2S dummy module. . . . .	52
3.45	Photograph of the alignment of the hybrid support rod. . . . .	53
3.46	Calculated correction factors $K_1^D$ (red), $K_2^D$ (turquoise), $K_1^s$ (blue) and $K_2^s$ (pink) plotted against the position of the pull test hook. . . . .	54
3.47	Deformation slope development of the source bond in the variation of the US power. . . . .	57

3.48	The plots (a) and (b) show mean values of deformation and uncorrected pull test result in variation of the US power for the source bond. The error is the standard deviation of the results. The blue triangles indicate the minimum and maximum values. Figure (c) combines both plots including the failure mode. . . . .	58
3.49	The plots (a) and (b) show mean values of deformation and uncorrected pull test results of the source bond for the variation of the setup BF and TDF. The error is the standard deviation of the results. The blue triangles indicate the minimum and maximum values. . . . .	59
3.50	Deformation slope development of the destination bond for the variation of the US power. . . . .	60
3.51	The plots (a) and (b) show mean values of deformation and uncorrected pull test result in variation of the US power for the destination bond. The error is the standard deviation of the results. The blue triangles indicate the minimum and maximum values. Figure (c) combines both plots including the failure mode.	61
3.52	The plots (a) and (b) show mean values of deformation and uncorrected pull test result of the destination bond for the variation of the BF and TDF setup value for the source bond. The error is the standard deviation of the results. The blue triangles indicate the minimum and maximum values. . . . .	62
3.53	Sketches visualizing the bonding programs. . . . .	63
3.54	The calculated correction factor $K_2$ plotted against the hook position. The correction factor is calculated using the Delvotec formula for the inner (red) and outer row (turquoise) and using the simple formula for the inner (blue) and outer row (pink). The region contained between the black / green dotted lines presents the estimated hook position for the inner / outer row of wires.	65
3.55	Problems regarding the wire bonding of the inner row of wires. . . . .	66
3.56	Uncorrected pull test results of the inner row test wires. . . . .	67
3.57	Uncorrected pull test results of the outer row test wires. . . . .	68
4.1	Sketch of an encapsulated 2S module using the dam-and-fill method on the top side and the glob top method on the bottom side. . . . .	71
4.2	Photograph of the self made dispensing robot. . . . .	72
4.3	Dispensing tests of Polytec EP 610. The glue lines are dispensed with intervals of twenty minutes. . . . .	74
4.4	Photographs of dispensing tests of Sylgard 184 and Sylgard 186. . . . .	74
4.5	Photograph of a TOB1 module which has been used for encapsulation tests.	75
4.6	Photograph of an encapsulation test of Sylgard 186 on wires of a TOB1 module. The picture consists of two photographs that have been merged. . . . .	76

4.7 Photograph of an encapsulation test of Polytec EP 610 on wires of a TOB1 module. The picture consists of five photographs that have been merged. . . 76

4.8 Comparison of the common mode corrected noise measurements of a TOB1 module without encapsulation (red), with only Sylgard 186 (blue) and with both Sylgard 186 and Polytec EP 610. . . . . 78

# List of Tables

3.1	Benchmark recommendation for pull tests on wire bonds from <i>F&amp;K Delvotec Bondtechnik GmbH</i> [20]. The variable WTS represents the wire tensile strength which is specified by the wire manufacturer. . . . .	16
3.2	Benchmark recommendation for the visual inspection of wire bonds from <i>F&amp;K Delvotec Bondtechnik GmbH</i> [20]. The variable WD represents the wire diameter. . . . .	20
3.3	Properties of the used bonding wedge <i>UT45A-W-2525-1.00-C</i> [23]. . . . .	22
3.4	Results of digital measurements of the wire geometry realized in the test program. . . . .	27
3.5	Summary of means and RMS of the histograms of calculated correction factors (Figure 3.17). . . . .	28
3.6	Default parameters for first parameter studies. . . . .	32
3.7	Set of BPC parameters. . . . .	45
3.8	Summary of the status and usage of the bond regions of the dummy module. . . . .	52
3.9	Summary of means and RMS of the histograms of calculated correction factors for the optimization of the <b>source bond</b> on the top right side of the module. The parameter $\mu$ is the mean correction factor and $\sigma$ is the standard deviation. . . . .	55
3.10	Summary of means and RMS of the histograms of calculated correction factors for the optimization of the <b>destination bond</b> on the top right side of the module. $\mu$ is the mean correction factor and $\sigma$ is the standard deviation. . . . .	56
3.11	Summary of the optimized bond parameters for the module wire bonding. . . . .	61
3.12	Summary of means $\mu$ and RMS $\sigma$ of the histograms of calculated correction factors for the pull tests of the inner and outer row of wires. . . . .	64
4.1	Overview of the tested encapsulant candidates. . . . .	70



# Bibliography

- [1] CERN, Cern timelines: The Large Hadron Collider, URL: <https://timeline.web.cern.ch/timelines/The-Large-Hadron-Collider>, May 2017
- [2] Nobelprice.org, Nobel Media AB 2014, The Nobel Prize in Physics 2013, URL: [http://www.nobelprize.org/nobel\\_prizes/physics/laureates/2013/](http://www.nobelprize.org/nobel_prizes/physics/laureates/2013/), May 2017
- [3] CMS Collaboration, D Contardo, M Klute, J Mans, L Silvestris, J Butler (editors), Technical Proposal for the Phase-II Upgrade of the CMS Detector, CERN-LHCC-2015-010, LHCC-P-008, CMS-TDR-15-02, Geneva, June 2015
- [4] CERN, About CERN, URL: <https://home.cern/about>, April 2017
- [5] CERN, The Large Electron-Positron Collider, URL: <https://home.cern/about/accelerators/large-electron-positron-collider>, May 2017
- [6] O Pooth, Habilitation Treatise RWTH Aachen University, The CMS Silicon Strip Tracker, ISBN: 978-3-8348-1003-8, 2010
- [7] C Patrignani et al. (Particle Data Group), Review of Particle Physics, Chin. Phys. C40:100001, 2016
- [8] CERN, Education, Communications and Outreach Group, LHC: the guide, URL: <https://cds.cern.ch/record/2255762/files/CERN-Brochure-2017-002-Eng.pdf>, February 2017
- [9] CERN, CMS Luminosity - Public Results, URL: <https://twiki.cern.ch/twiki/bin/view/CMSPublic/LumiPublicResults>, May 2017
- [10] CMS Collaboration, K Klein (editor), The Phase-2 Upgrade of the CMS Tracker, CERN-LHCC-2017-009. CMS-TDR-014, Geneva, June 2017, submitted to the LHCC, to be published
- [11] CERN, The HL-LHC project, URL: <http://hilumilhc.web.cern.ch/about/hl-lhc-project>, May 2017
- [12] CMS Collaboration, About CMS, URL: <https://cms.cern/detector>, September 2017

- [13] CMS Collaboration, The Compact Muon Solenoid : technical proposal, CERN-LHCC-94-38, LHCC-P-1, 1994
- [14] CMS Collaboration, The CMS experiment at the CERN LHC, 2008 JINST 3 S08004, URL: <http://stacks.iop.org/1748-0221/3/i=08/a=S08004>, 2008
- [15] A Künsken, PhD Thesis RWTH Aachen University, Studies on the use of the CMS outer hadron calorimeter in the level-1 Muon trigger, 2017
- [16] C Ruoff, A Closer Look At Wire Bonding, Charged: Electric Vehicles Magazine, URL: <http://www.hesse-mechatronics.com/wp-content/uploads/hesse-wire-boding-artilce-chargedevs-spreads.pdf>, March/April 2016
- [17] Private communication with F&K Delvotec Bondtechnik GmbH, 2017
- [18] F Farassat, Bondprozesskontrolle, URL: [https://www.fkdelvotec.com/fileadmin/media\\_fuk/dokumente/Bondprozesskontrolle.pdf](https://www.fkdelvotec.com/fileadmin/media_fuk/dokumente/Bondprozesskontrolle.pdf), August 2017
- [19] J Sedlmair, F Schlicht, F Farassat, Welche Frequenz ist am besten zum Drahtbonden?, F&K Delvotec Bondtechnik GmbH, URL: [https://www.fkdelvotec.com/fileadmin/media\\_fuk/dokumente/160809D\\_TN\\_15\\_01\\_Frequenz.pdf](https://www.fkdelvotec.com/fileadmin/media_fuk/dokumente/160809D_TN_15_01_Frequenz.pdf), 2015
- [20] F&K Delvotec Bondtechnik GmbH, F&K Delvotec: Test Standard Wirebonding, February 2016, This is a summary of the test standard recommended by F&K Delvotec Bondtechnik GmbH. The information was provided in the context of the acquisition of a new bonding machine.
- [21] S Schmitz, J Kripfgans, M Schneider-Ramelow, W Müller, K Lang, Investigating wire bonding pull testing and its calculation basics, Proceedings of the 5th Electronics System-integration Technology Conference (ESTC), September 2014
- [22] F&K Delvotec Bondtechnik GmbH, Bonder 64000 G5: Benutzerhandbuch, Ottobrunn, Germany, 2012
- [23] Small Precision Tools, US/UT Series - Universal Bonding Tool, URL: [http://www.smallprecisiontools.com/File/products/bonding/wedges/details/US-UT\\_Series%20-%20Available%20Sizes%20and%20How%20to%20Order%20-%20English.pdf](http://www.smallprecisiontools.com/File/products/bonding/wedges/details/US-UT_Series%20-%20Available%20Sizes%20and%20How%20to%20Order%20-%20English.pdf), August 2017
- [24] Heraeus, Bonding Wires for Semiconductor Technology, URL: [https://www.heraeus.com/media/media/het/doc\\_het/products\\_and\\_solutions\\_het\\_documents/bonding\\_wires\\_documents/Brochure\\_Bonding\\_Wire.pdf](https://www.heraeus.com/media/media/het/doc_het/products_and_solutions_het_documents/bonding_wires_documents/Brochure_Bonding_Wire.pdf), August 2017
- [25] Dage Precision Industries, Dage Series 3000: An Operators Guide, Version 2

- [26] Nikon, SMZ445 / SMZ460: Zoom Stereomicroscopes, URL: [https://www.nikoninstruments.com/en\\_DE/Products/Stereomicroscopes-and-Microscopes/Stereomicroscopes/SMZ445](https://www.nikoninstruments.com/en_DE/Products/Stereomicroscopes-and-Microscopes/Stereomicroscopes/SMZ445), August 2017
- [27] Nikon, Stereoscopic Zoom Microscope SMZ645 / SMZ660 Instructions, August 2017
- [28] Keyence, VHX-900F, URL: <http://www.keyence.de/products/microscope/digital-microscope/vhx-900f/models/vhx-900f/index.jsp>, August 2017
- [29] IPC: Association Connecting Electronics Industries, Spezifikation für chemisch Nickel/Gold (ENIG) für Oberflächen von Leiterplatten, URL: <http://www.ipc.org/TOC/IPC-4552-German.pdf>, October 2002
- [30] Inkscape, URL: <https://inkscape.org/de/>, August 2017
- [31] OpenCV, URL: <http://opencv.org/>, September 2017
- [32] J Bonnaud, A Honma, CERN, Privat communication, 2017
- [33] Polytec PT: Polymere Technologien, Polytec EP 610: Ungefüllter Epoxidharzklebstoff, Technische Daten, URL: [http://www.polytec-pt.com/no\\_cache/de/produkte/epoxidklebstoffe/epoxidharzklebstoffe-und-vergussmassen/?cid=20328&did=24621&sechash=39f60ebe](http://www.polytec-pt.com/no_cache/de/produkte/epoxidklebstoffe/epoxidharzklebstoffe-und-vergussmassen/?cid=20328&did=24621&sechash=39f60ebe), January 2016
- [34] Dow Corning, Sylgard 184 Silicone Elastomer, URL: <http://www.dowcorning.de/DataFiles/090276fe80190b08.pdf>, April 2014
- [35] Dow Corning, Dow Corning 186 Silicone Elastomer, URL: <http://www.dowcorning.de/DataFiles/090276fe8018f8ef.pdf>
- [36] Scheugenpflug AG, Selektiver Schutz für Leiterplatten: Glob Top, Dam and Fill & Flip Chip Underfill, URL: <http://www.scheugenpflug.de/anwendungen/bauteile-komponenten/glob-top-bei-leiterplatten.html>, September 2017
- [37] Amann Girbach, smartmix X2, URL: <https://www.amanngirrbach.com/de/produkte/modellherstellung/smartmix-x2/>, September 2017
- [38] Nordson EFD, Ultra 1400 Series Dispenser: User's guide
- [39] National Instruments, USB-6008, URL: <http://www.ni.com/de-de/support/model.usb-6008.html>, September 2017
- [40] M Pöttgens, PhD Thesis RWTH Aachen University, Development and evaluation of test stations for the quality assurance of the silicon micro-strip detector modules for the CMS experiment, 2007

- [41] M Axer, PhD Thesis RWTH Aachen University, Development of a Test System for the Quality Assurance of Silicon Microstrip Detectors for the Inner Tracking System of the CMS Experiment, 2003